



**HAL**  
open science

# Multiple contrast-bolus injection strategy for the quantification of hepatic tumor perfusion by DCE-MRI: a rabbit study

Sofia Veneti

► **To cite this version:**

Sofia Veneti. Multiple contrast-bolus injection strategy for the quantification of hepatic tumor perfusion by DCE-MRI: a rabbit study. Medical Imaging. Université Paris Cité, 2019. English. NNT : 2019UNIP5065 . tel-03860687

**HAL Id: tel-03860687**

**<https://theses.hal.science/tel-03860687>**

Submitted on 18 Nov 2022

**HAL** is a multi-disciplinary open access archive for the deposit and dissemination of scientific research documents, whether they are published or not. The documents may come from teaching and research institutions in France or abroad, or from public or private research centers.

L'archive ouverte pluridisciplinaire **HAL**, est destinée au dépôt et à la diffusion de documents scientifiques de niveau recherche, publiés ou non, émanant des établissements d'enseignement et de recherche français ou étrangers, des laboratoires publics ou privés.



# Université de Paris

**Ecole doctorale : Médicament, Toxicologie, Chimie, Imageries (MTCI)**

*Laboratoire : Paris Centre de Recherche Cardiovasculaire (PARCC)-INSERM U970*

---

## **Multiple contrast-bolus injection strategy for the quantification of hepatic tumor perfusion by DCE-MRI: a rabbit study**

---

Par Sofia Veneti

Thèse de doctorat en Imageries

Dirigée par Charles-André Cuenod

Présentée et soutenue publiquement le 28 Novembre 2019

Devant un jury composé de :

Pr. Christophe Aube	PU-PH, Université d'Angers, Angers	Rapporteur
Pr. Nathalie Lassau	PU-PH, Université Paris XI, Paris	Rapporteur
Pr. Emmanuelle Canet-Soulas	Professeur des Universités, Université Lyon 1, Lyon	Examineur
Dr. Olivier Pellerin	PH-HDR, Université Paris V, Paris	Examineur
Dr. Philippe Garteiser	CR, Université Paris Diderot, Paris	Examineur
Pr. Charles-André Cuenod	PU-PH, Université Paris V, Paris	Directeur de thèse

# ABSTRACT

---

## Introduction

Hepatic tumors represent a major burden in medical practice, and imaging techniques play a pivotal role in their detection and diagnosis. Dynamic contrast-enhanced MRI (DCE-MRI) is increasingly proposed to evaluate cancer perfusion, along with DCE-CT and DCE-US. DCE-MRI, however, suffers from low temporal resolution, low signal to noise ratio (SNR), motion artifacts, and it is especially limited by the non-linearity of the relationship between signal and contrast-agent (CA) concentration. Moreover, in the liver, dual-input kinetic models are required, as the portal input function (PIF) has to be considered in addition to the arterial input function (AIF). Such dual-input kinetic models are especially demanding in terms of temporal resolution and tissue enhancement.

In this work, to overcome many of the limitations, we propose to use an original strategy based on a multi-bolus injection of diluted CA. The goal is to avoid the saturation effect of high concentration of CA, while compensating for the consequent loss of “enhancement to noise ratio” (E/N) by increasing the number of bolus injections. Besides, it has the advantage of being more robust to an unexpected event such as motion during a single bolus injection.

This strategy has been tested on simulation data and rabbits bearing liver tumors pre and post embolization.

## Materials and Methods

### *Simulation Study*

A computer simulation was developed using real arterial input function (AIF) and portal input function (PIF) obtained on rabbit with a 4.7T MRI scanner applying single- and multi bolus injection schemes. Liver enhancement curves were simulated with a dual-input model by varying the perfusion parameter values (Hepatic Perfusion Indexes -HPI, total hepatic blood flow -Ft, and distribution volume fractions -vd) and noise has been added. Then, a deconvolution was applied to estimate back the parameters. The estimated and the initial parameters were compared and evaluated by the Coefficient of Variation (CV) of their differences.

### *In vivo analysis*

VX2 tumors have been implanted in the liver of 10 rabbits. Transcatheter arterial embolization (TAE) was used to treat these tumors.

DCE-MRI pre and post embolization were obtained with four boluses of 1/25 diluted Gd-DOTA. The injection volume was 4ml per bolus and the injection rate was 3ml per sec.

The perfusion parameters of the liver and the tumors have been extracted by dual input single- and two-compartment models and compared with each other before and after embolization.

## **Results**

### *Simulation Data*

The respective improvement factors in the 4-bolus injection were 47.9% ( $P < 2 \cdot 10^{-5}$ ), 35.7% ( $P < 2 \cdot 10^{-5}$ ), and 65.9% ( $P < 2 \cdot 10^{-5}$ ).

### *In vivo analysis*

Pre-embolisation,  $F_t$  of liver and tumor border were higher than of tumor core. The  $v_d$  and area under the curve (AUC) of the liver were higher than in tumor core but lower than in tumor border. Post-embolisation,  $F_t$  and  $v_d$  of the liver remained constant, while both  $F_t$  and  $v_d$  of tumor border were decreased compared to pre-embolisation. HPI of post-embolization of the poorly vascularized tumor core was not measurable as its enhancement curves are close to the noise level.

## **Conclusion**

The multi-bolus injection strategy opens up new prospects in quantitative DCE-MRI. This study shows that multi-bolus injections with diluted bolus improve the robustness of DCE measurements by making the acquisition less sensitive to bias or unexpected movements while allowing an acquisition in the quasi-linearity zone of the relation between CA and signal. It has the drawback of not providing the classical images obtained at the arterial, portal, and late phases. However, this may be the trade-off to obtain a better quantitative measurement. Moreover, it may be envisioned to provide synthetic images with the standard phases.

# RESUME

---

## Introduction

Les tumeurs hépatiques représentent un problème fréquent. Les techniques d'imagerie jouent un rôle central dans leur détection et leur diagnostic. L'IRM dynamique avec injection de produit de contraste (DCE-IRM) est de plus en plus proposée pour évaluer la perfusion des cancers. Mais elle souffre d'une faible résolution temporelle, d'un faible rapport signal / bruit (SNR), d'artefacts de mouvements, et elle est particulièrement limitée par la non-linéarité de la relation signal-concentration d'agent de contraste (AC). De plus, dans le foie, des modèles cinétiques à double entrée sont nécessaires, car la fonction d'entrée portale (PIF) doit être prise en compte en plus de la fonction d'entrée artérielle (AIF). Ces modèles sont techniquement particulièrement exigeants.

Nous proposons d'utiliser une stratégie originale basée sur une injection multi-bolus d'AC dilué. L'objectif est d'éviter les effets de saturation des concentrations élevées, tout en compensant la chute du «rapport rehaussement/bruit» en augmentant le nombre de bolus. En outre, elle présente l'avantage d'être plus robuste face à un événement imprévu, tel qu'un mouvement lors de l'injection d'un bolus unique.

Cette stratégie a été testée sur des données de simulation et chez des lapins porteurs de tumeurs avant et après embolisation.

## Matériel et méthodes

### *Simulation*

Une simulation a été développée à l'aide d'une AIF et d'une PIF réelles obtenues chez un lapin à 4,7T en appliquant des schémas d'injection en bolus unique et multiples. Les courbes de rehaussement tissulaire hépatique ont été simulées avec un modèle à double entrée en faisant varier les valeurs des paramètres de perfusion (index de perfusion hépatique -HPI, débit sanguin hépatique total -Ft et fractions de volume de distribution -vd) ; puis du bruit a été ajouté. Ensuite, une déconvolution a été appliquée pour estimer les paramètres. Les paramètres estimés et initiaux ont été comparés et évalués par le coefficient de variation (CV) de leurs différences.

### *In vivo*

Des tumeurs VX2 ont été implantées dans le foie de 10 lapins. Une embolisation artérielle transcathéter (TAE) a été utilisée pour traiter ces tumeurs.

La DCE-MRI pré et post-embolisation a été obtenue avec quatre bolus de Gd-DOTA dilués au 1/25. Le volume d'injection était de 4 ml par bolus et le débit d'injection était de 3 ml par seconde. Les paramètres de perfusion du foie et des tumeurs ont été extraits par des modèles à deux entrées à un et deux compartiments et comparés les uns aux autres avant et après l'embolisation.

## **Résultats**

### *Simulation*

Pour HPI, Ft et vd, les facteurs d'amélioration de l'injection en 4 bolus par rapport à l'injection simple bolus étaient de 47,9% ( $P < 2 * 10^{-5}$ ), 35,7% ( $P < 2 * 10^{-5}$ ) et 65,9% ( $P < 2 * 10^{-5}$ ).

### *In vivo*

Avant embolisation, le Ft du foie et de la périphérie tumorale étaient plus élevés que ceux du centre de la tumeur. Le vd et l'aire sous la courbe (AUC) du foie étaient plus élevés que dans le centre tumoral, mais inférieures à ceux de la périphérie tumorale. Après l'embolisation, Ft et vd du foie restaient inchangés, tandis que Ft et vd du bord de la tumeur étaient diminués. On notait que l'HPI post-embolisation des centres des tumeurs, mal vascularisés, n'étaient pas mesurables car leurs rehaussements étaient proches du niveau de bruit.

## **Conclusion**

La stratégie multi-bolus ouvre de nouvelles perspectives en DCE-IRM quantitatif. Elle améliore la robustesse des mesures de DCE-IRM en rendant l'acquisition moins sensible aux mouvements inopinés, tout en permettant une acquisition dans la zone de quasi-linéarité de la relation signal concentration d'agent de contraste. Elle a néanmoins pour inconvénient de ne pas fournir les images aux phases artérielle, portale et tardive. Cela peut être le prix à payer pour obtenir une meilleure mesure quantitative. De plus, il est possible de reconstruire a posteriori des images synthétiques des phases standard.

# ACKNOWLEDGEMENTS

---

Foremost, I would like to express my sincerest gratitude to my supervisor, Prof. **Charles. A. Cuenod**, for his continuous support of my Ph.D study and research, and for his patience, guidance, motivation, and immense knowledge.

A big thank you goes to:

Pr. **Bertrand Tavitian** and **Olivier Clement** for accepting me in the laboratory and for all their pertinent remarks.

All of my colleagues and Masters students in the laboratory for our excellent collaboration and all the fun we have had together throughout the past four years. More specifically, I will remember: **Anais's** carelessness and joy. She will always be my "little sister". **Maylin's** hearty laugh and reasonableness. **Caterina's** Italian temperament and amazing Italian sweets. **Thula's** industriousness. **Amel's** sweetness. **Thoma's** dark humor. **Daniel's** home remedies and love of plants. **Gwenn's** singing in the office. **Afef's** maturity and peacefulness. **Umit's** peacefulness and kindness. **Habib's** revoluntary spirit. **Imad's** organizational skills.

Among them, I would especially like to thank **Dr. Daniel Balvay** for his priceless help on the programming and the image analysis, the reduction of the articles and my thesis reduction. Furthermore, I would like to thank Dr. **Gwennh el Autret** for the MRI knowledge that she shared with me and **Afef Bouchouicha** for her valuable statistic knowledge that she conveyed to me. I would also like to thank post-doc **Imad Benkhaled** for his help on the programming code of the 1<sup>st</sup> and 2<sup>nd</sup> article.

I would like to thank the post-doc **Anja Nitzsche** for her emotional support during the difficult moments throughout my thesis

And the Masters students: **Konstantina, Ikram, Pamela** for our beautiful friendship that built up even outside of the laboratory.

My sincere thanks go to **Dr. Florentina Pascale, Dr. Olivier Pellerin**, and Dr. **Tchao M atchi** for their priceless contribution to my 2<sup>nd</sup> part of my thesis on the tumor implantation, treatment, and histology analysis, respectively. Without their help, I could not successfully complete this part of my thesis.

I would like to thank all of the people at the Guerbet company for the training on the VX2 tumor implantation in the rabbit liver.

A special thanks goes to all the members of the animal house; **Martine, Julie, Adrien, Alexis, and Sophie** for our great collaboration and their patience when I had difficulty expressing my thoughts in French--I will never forget the care and love Martine gave me, as if she were my mother.

I would also like to thank all the people who have crossed my path in the PARCC and HEGP. Finally, and above all, I owe a big thank you to

My boyfriend, **Alexandros**, for his endless patience, his love, and his selfless support, keeping my confidence high in difficult moments throughout my Ph.D.

My parents; **Christos and Matoula**, and my sisters; **Katerina and Ilektra**, for their love, support, and encouragement throughout my research.

# TABLE of CONTENTS

---

Multiple contrast-bolus injection strategy for the quantification of hepatic tumor perfusion by DCE-MRI: a rabbit study .....	0
ABSTRACT.....	1
RESUME.....	3
ACKNOWLEDGEMENTS .....	5
TABLE of CONTENTS.....	7
LIST of FIGURES.....	9
LIST of TABLES .....	13
ABBREVIATIONS & SYMBOLS .....	14
<b>I. GENERAL INTRODUCTION .....</b>	<b>17</b>
<b>I.1 LIVER TUMOR – LIVER IMAGING – AND PERFUSION IMAGING .....</b>	<b>17</b>
<b>I.2 CONTEXT OF THE STUDY .....</b>	<b>18</b>
1.2.1 PARCC-INSERM-HEGP & MY LABORATORY .....	18
1.2.2 HECAM PROJECT (HEPATOCELLULAR CARCINOMA MULTI-TECHNOLOGICAL).....	19
1.2.3 COLLABORATIONS .....	19
1.2.4 TRAINING ON ANIMAL EXPERIMENTATION .....	20
<b>I.3 MAIN CONTRIBUTION OF THE THESIS .....</b>	<b>20</b>
<b>I.4 LIST OF PUBLICATIONS AND MEETINGS.....</b>	<b>20</b>
1.4.1 SCIENTIFIC PAPERS .....	20
1.4.2 CONFERENCE AND MEETING CONTRIBUTIONS.....	21
<b>II. CURRENT KNOWLEDGE ON THE LIVER AND MICROCIRCULATION IMAGING .....</b>	<b>22</b>
<b>II.1 LIVER ANATOMY AND PHYSIOLOGY .....</b>	<b>22</b>
11.1.1 MACROSCOPIC LIVER ANATOMY.....	22
11.1.2 HEPATIC VASCULATURE .....	24
11.1.3 MICROSCOPIC ANATOMY OF THE LIVER .....	26
11.1.4 LIVER PHYSIOLOGY .....	30
<b>II.2 HEPATOCELLULAR CARCINOMA .....</b>	<b>34</b>
11.2.1 LIVER TUMORS .....	34
11.2.2 HEPATOCELLULAR CARCINOMA (HCC).....	34
<b>II.3 PERFUSION IMAGING .....</b>	<b>44</b>
11.3.1 PERFUSION .....	44
11.3.2 PERFUSION MEASUREMENT METHODS IN MAGNETIC RESONANCE IMAGING (MRI) .....	48
11.3.3 DCE-MRI .....	51
11.3.4 QUANTITATIVE ANALYSIS.....	58
<b>II.4 LIVER PERFUSION AND LIVER PERFUSION IMAGING .....</b>	<b>64</b>
11.4.1 LIVER PERFUSION .....	64

II.4.2	SIGNAL ANALYSIS IN THE LIVER.....	65
<b>III.</b>	<b>OPTIMIZING THE BOLUS SCHEME FOR LIVER DCE-MRI: THE FOUR BOLUSES STRATEGY</b>	<b>75</b>
	<b>75</b>	
<b>III.1</b>	<b>OPTIMIZATION OF THE ACQUISITION PROTOCOL.....</b>	<b>75</b>
III.1.1	RABBIT HANDLING.....	75
III.1.2	MRI PROTOCOLS.....	78
<b>III.2</b>	<b>COMPUTER SIMULATION TESTING OF THE FOUR BOLUSES STRATEGY (PAPER I).....</b>	<b>85</b>
III.2.1	INTRODUCTION.....	85
III.2.2	MATERIAL & METHODS.....	86
III.2.3	RESULTS.....	88
III.2.4	DISCUSSION.....	90
III.2.5	CONCLUSION.....	91
<b>III.3</b>	<b>VX2 TUMOR HANDLING AND TREATMENT.....</b>	<b>92</b>
III.3.1	VX2 TUMOR HANDLING.....	92
III.3.2	VX2 TUMOR TREATMENT: TRANSCATHETER ARTERIAL EMBOLIZATION (TAE).....	99
<b>III.4</b>	<b>IN VIVO TESTING OF THE FOUR BOLUSES STRATEGY (Paper II; in preparation).....</b>	<b>101</b>
III.4.1	INTRODUCTION.....	101
III.4.2	MATERIAL AND METHODS.....	101
III.4.3	RESULTS.....	105
III.4.4	DISCUSSION.....	110
III.4.5	CONCLUSION.....	111
<b>IV.</b>	<b>GENERAL CONCLUSION &amp; PERSPECTIVES.....</b>	<b>112</b>
	<b>112</b>	
<b>IV.1</b>	<b>CONCLUSION.....</b>	<b>112</b>
<b>IV.2</b>	<b>PERSPECTIVES.....</b>	<b>113</b>
<b>V.</b>	<b>REFERENCES.....</b>	<b>115</b>
	<b>115</b>	
	<b>PAPER I: Multi-Bolus Injection to Improve the Robustness of Liver DCE-MRI: A Simulation</b>	
	<b>Study in Rabbits.....</b>	<b>121</b>

# LIST of FIGURES

---

<b>Figure 1</b> : Morphological anatomy of the liver. ....	22
<b>Figure 2</b> : Functional anatomy of the liver. (a) Anterior view, and (b) posterior view. ....	23
<b>Figure 3</b> : Couinaud's segmentation of the liver. ....	23
<b>Figure 4</b> : Liver arterial supply. ....	25
<b>Figure 5</b> : Vasculature inflow of portal vein. ....	25
<b>Figure 6</b> : Intrahepatic vascular anatomy, anterior view. ....	26
<b>Figure 7</b> : Microscopic anatomy of the liver.....	27
<b>Figure 8</b> : The three concepts of the microscopic liver anatomy. ....	28
<b>Figure 9</b> : (a) Depiction of sinusoidal space and space of Disse. (b) Histology image of Space of Disse. Reticular fibers are stained black with silver. Hepatocytes are weakly stained. ....	29
<b>Figure 10</b> : Histology image-Kupffer cells' depiction. Kupffer cells can be recognized by their oval nuclei closely associated with sinusoidal spaces. ....	29
<b>Figure 11</b> : Depiction of micelle ....	30
<b>Figure 12</b> : Bile salts congregate around fat and separate them into small droplets called micelles.....	31
<b>Figure 13</b> : Regional variation in the incidence rates of liver cancer. The incidence rates shown pertain to both sexes and all ages. Adapted from the World Health Organization.....	35
<b>Figure 14</b> : <b>Changes in diagnosis of HCC over time</b> .....	36
<b>Figure 15</b> : <b>Large HCC tumor</b> (black straight arrow). Dynamic T1-weighted GRE sequence (TR/TE/FA=154ms/6ms/70°). (a) Before injection, a hypo-intense signal lesion presented with a hypo-intense pseudo-capsule. (b) 15 seconds post-injection of gadolinium, the HCC shows a hyper-vascular appearance with a non-enhancing capsule. (c) 5 minutes post-injection of gadolinium a more hypo-intense enhancement of the tumorous lesion depicted with the beginning of enhancement of parts of the capsule.....	38
<b>Figure 16</b> : <b>Diagnostic algorithm for HCC in expert centers</b> .....	38
<b>Figure 17</b> : <b>Modified BCLC staging and treatment strategy</b> .....	40
<b>Figure 18</b> : Development of HCC and first-line treatment options for each stage.....	41
<b>Figure 19</b> : Prognosis of patients with HCC based on imaging findings .....	43
<b>Figure 20</b> : Blood microcirculation. It is the blood circulation in capillaries which in between arterioles and venules, it is the most basic structural and functional unit in the circulatory system by delivering oxygen and nutrients and removing carbon dioxide (CO <sub>2</sub> ). ....	45
<b>Figure 21</b> : Simple model of blood circulation with a single arterial input and single bolus venous output. Loss of blood is not allowed, so tissue blood flow (Ft) and tissue blood volume (vt) are assumed constant. ....	46
<b>Figure 22</b> : Different types of contrast-agents and their deposition in the tissue. ....	48
<b>Figure 23</b> : Dynamic contrast-enhanced (DCE)-MRI acquisition. (a) Intravenous injection of contrast-agent (CA) and repeated imaging to monitor the traversal of contrast-agent within the tissue. (b) Both vascular space and tissue enhancement curves represent the intensity of contrast agent before, during, and after the CA injection at specific time points. ....	52
<b>Figure 24</b> : Performance of gradient echo with various FA values. TR=3ms, T <sub>1</sub> =1sec .....	53
<b>Figure 25</b> : Tissue enhancement curves after bolus injection of contrast agent. (a) Tissue enhancement curve without interstitial leakage . (b) Tissue enhancement curve with interstitium leakage . (c) Overview of contrast agent enhancement. The tissue enhancement (solid blue line) represents the sum of the contrast-agent enhancement in the tissue vascular	

space (initial rapid upslope curve), plus the contrast-agent enhancement into the interstitial space (slower downslope curve). (d) Depiction of the perfusion parameters for the vascular space (red enhancement curve) and the interstitial space (green enhancement curve). The sum of the  $F_t$  and  $PS$  express the  $K^{trans}$  parameter. ....55

**Figure 26 :** Semi-quantitative parameters' depiction. ....57

**Figure 27: Algorithm of the fitted parameters' data extraction.** Measured arterial input function (AIF) is applied to a pharmacokinetic model with a value range of perfusion parameters in order to generate tissue enhancement curves (tissue signal modeling). Additionally, the same measured input function (AIF) is applied to a real tissue extracting the measured tissue enhancement curve. Those enhancement curves (generated and measured) are compared between them and by employing the fitting technique, the fitted data of the perfusion parameters are extracted and derived from the best fit between the curves. ....58

**Figure 28 :** (a) **Depiction of a 2CXM model depiction** . Gadolinium-based contrast-agent does not enter cells.  $v_p$ =volume of plasma,  $v_e$ = volume of interstitium,  $PS$ = permeability surface area product. ....60

**Figure 29 : Depiction of Tofts model.** It is a weakly vascularized model. The plasma compartment has a negligible volume ( $v_p \approx 0$ ) and the interstitium is well-mixed. ....61

**Figure 30 : (A) Normal liver.** The exchange of the low molecular contrast agent (Gd) between the vascular space and interstitial space is spontaneously done through fenestrae. **(B) Cirrhotic liver.** The exchange of the contrast agent molecules between vascular and interstitial space is limited because of the fenestrae loss, which causes an enlargement of interstitial space (space of Disse). ....64

**Figure 31 :** Schematic plot of the liver and spleen enhancement curves after a bolus injection of contrast agent. The diagram illustrates the biphasic enhancement of the liver consisted in arterial and portal phases.  $g_a$ = maximum slope of liver enhancement curve before peak splenic enhancement.  $g_p$ = maximum slope of liver enhancement curve after peak splenic enhancement. ....67

**Figure 32 :** (A) Dual-input single compartment model. Using this model, the kinetic parameters related to hepatic blood flow ( $F_t$ ) consisted of the hepatic artery ( $FA$ ) and the portal vein ( $F_{pv}$ ) into the liver, and the distribution volume ( $vd$ ) where the mixed hepatic blood flow distributes. (B) Dual-input two compartment conventional model. Using this model, the additional kinetic parameters that can be measured are the volume of the interstitial space ( $v_e$ ) and the permeability surface area product ( $PS$ ). ....68

**Figure 33 :** Relations between the residue function  $R(t)$ , the cumulative frequency function  $H(t)$ , and the probability density function  $h(t)$ . Both the initial value of  $R(0)$  and the final value of  $H(\infty)$  are normalized to one (1), and their combination corresponds to the area under the curve  $h(t)$ . ....73

**Figure 34 :** (a) Anesthesia maintenance in rabbits during the MRI experiment with Isoflurane through the v-gel endotracheal mask. (b) Endotracheal v-gel mask. ....76

**Figure 35 :** Vet examination bag used to handle the rabbits during the pre-medication anesthesia injection to keep the rabbit restrained in a gentle way. ....77

**Figure 36 :** Single-bolus protocol with 5ml of Gd-DOTA and a concentration dilution at 1/5. Signal saturation at the AIF curve. ....80

**Figure 37 :** Three different dual-bolus injection protocols. (a) 1st bolus: 3ml Gd-DOTA (1/10 dilution), 2nd bolus: 1ml Gd-DOTA (pure), and time interval between boluses: 1min. (b) 1st bolus: 5ml Gd-DOTA (1/10 dilution), 2nd bolus: 5ml Gd-DOTA (1/10 dilution), and time interval between boluses: 1min 30 sec. (c) 1st bolus: 5ml Gd-DOTA (1/15 dilution), 2nd bolus: 5ml Gd-

DOTA (1/15 dilution), and time interval between boluses: 2min. The (c) protocol is better than the other two because it has less saturation effects and efficient wash-out part of first bolus. 80

**Figure 38** : Two different bolus injection protocols. (a) 3-bolus injections' protocol; 5ml Gd-DOTA with a concentration dilution at 1/15. (b) 4-bolus injections' protocol; 4ml Gd-DOTA with a concentration dilution at 1/25..... 81

**Figure 39** : four-boluses injection protocols applied to the same rabbit (a) without the MR compatible injector (b) with the MR-compatible injector. When using the MR-compatible injector, the AIF transit pattern is sharp and identical in each bolus..... 82

**Figure 40** : Single-bolus injection and multi (four)-bolus injection schemes. The acquisition duration is 10min for both schemes. The bolus volume is 4ml of contrast agent (Gd-DOTA) with a 1:25 dilution and injection rate at 3ml/sec for both schemes..... 86

**Figure 41** : Vascular enhancement curves of Arterial Input Function (AIF) and Portal Input Function (PIF) for both injection schemes (c,d) acquired by the respective abdominal aorta ROI (a) and the portal vein ROI (b)..... 87

**Figure 42** : Simulation workflow..... 88

**Figure 43** : Variability of the perfusion measurement applying the multi-bolus injection scheme. HPI: Hepatic perfusion index, Ft: total tissue blood flow, vd: distribution volume, CV: coefficient of variation. p-values extracted by performing the F-test.  $p \leq 2 \cdot 10^{-3}$ : \*,  $p \leq 2 \cdot 10^{-4}$ : \*\*,  $p \leq 2 \cdot 10^{-5}$ : \*\*\* ..... 89

**Figure 44** : Variability of the perfusion measurement increasing the acquisition duration with the single-bolus injection scheme. HPI: Hepatic perfusion index, Ft: total tissue blood flow, vd: distribution volume, CV: coefficient of variation. .... 90

**Figure 45** : Cardiac monitoring armlet around the anterior paw of the rabbit (black straight arrow), v-gel mask connected with the isoflurane gas application (dashed arrow), and ear catheter (red straight arrow). .... 93

**Figure 46** : (a) rabbit abdomen shaving, (b) betadine application on the rabbit abdomen ..... 93

**Figure 47** : (a) Vertical oriented mini-laparotomy abdominal incision with a 15-blade and a blunt dissection. (b) Liver is kept moist with the help of a wet gauze. .... 94

**Figure 48** : (a) Solid VX2 tumor fragment. (b) Gentle push of the VX2 fragment into the liver parenchyma with the tip of a fine forceps. .... 94

**Figure 49** : (a) Fascial repair sutures. (b) Cutaneous ligation sutures ..... 95

**Figure 50** : (a,b) Aggressive and probably virus stem VX2 tumor ..... 96

**Figure 51** : (a) VX2 tumor nodule. (b) the respective slices of VX2 tumor ..... 97

**Figure 52** : (a) Gentle scraping for the removal of necrotic core. (b) Separation of viable tumor from adherent muscle tissue ..... 98

**Figure 53** : Bathing of tumor in the nutrient-rich solution (left). Small fragments of tumor, for immediate intrahepatic implantation, stored in the physiologic serum (right)..... 98

**Figure 54** : (a) Liquid nitrogen container. (b) cryotubes in different sizes ..... 99

**Figure 55** : Angiography of a liver bearing a VX2 tumor The vascularization of VX2 tumor is clear (black arrow)..... 100

**Figure 56** : DCE-MRI and TAE treatment timeline. .... 102

**Figure 57** : Multi (four)-bolus injection scheme ..... 103

**Figure 58** : ROIs and respective enhancement curves from the same rabbit pre-embolisation and post-embolisation. Pre-embolisation, the signal of the tumor is higher than the liver while post-embolisation, because of the embolisation, the signal of the tumor is lower than the liver. .... 104

**Figure 59** : Typical fitting (in black) of the tissue enhancement curves (in green) of the liver (left) and the tumor(right) with the single-compartment model, pre-embolisation (upper curves), and post-embolisation (bottom curves). The residual of the fitting process is displayed as blue crosses, and remains well centered around the zero level, attesting the quality of the adjustment..... 106

**Figure 60** : pre- and post-embolisation perfusion parameters of the tissues (liver, tumor) for the Hepatic Perfusion Index (HPI),  $K^{trans}$ , and distribution volume (vd) parameters. The measurements are expressed as median with 95% Confidence Interval (CI). ..... 107

**Figure 61** : Graph of the paired parameter values. a) normal liver and tumor pre-embolization, b) normal liver and tumor post-embolization, c) normal liver pre- and post-embolization, d) tumor pre- and post-embolization. .... 108

**Figure 62 : One-week post-embolization pathology (H&E staining).** (a) Magnification 2.7x. Three different regions of the post-embolisation sample: normal liver (A), fibrotic band between liver and embolized VX2 tumor (B), embolized VX2 tumor (C). (b) Magnification (11.1x.) of the left black rectangle within the embolized tumor. The embolized tumor contains fibrosis (straight arrows), necrotic cells (green outlines) and vital tumor cells (the small black dots are the nuclei of the vital VX2 cells). ..... 109

**Figure 63 : One-week post-embolization liver tissue affected by the transcatheter arterial embolisation (TAE) (H&E staining)** Magnification 3.7x. Embolisation product is found into the vessels of the liver (green outline). There are necrotic sites (red outlines) adhered to fibrosis sites (light blue areas). Black arrows indicate the remaining normal liver. .... 110

# LIST of TABLES

---

<b>Table 1:</b> Three Types of Perfusion MRI Techniques .....	50
<b>Table 2:</b> Perfusion parameters that can be extracted by using single-compartment or two-compartment model.....	71
<b>Table 3:</b> List of rabbit deaths before and during the MRI experiments.....	77
<b>Table 4:</b> The sequences of my MRI protocol for the liver study. ....	79
<b>Table 5:</b> Different bolus injection protocols performed within the entire interval of my thesis..	84
<b>Table 6:</b> Initial perfusion parameters' range .....	88
<b>Table 7 :</b> MRI sequences .....	103
<b>Table 8 :</b> Median values of perfusion parameters values of the liver and the tumor pre- and post-embolisation. MAD: Median Absolute Deviation. SD: Standard Deviation.....	107
<b>Table 9:</b> Mean paired differences of the parameters and their p-values (comparison in the different combinations displayed in Figure 61) (Wilcoxon matched pairs test). The asterisk (*) indicates the statistically significant results ( $p < 0.05$ ), and the cross (+) the quasi-significant results ( $p < 0.1$ ). ....	109

# ABBREVIATIONS & SYMBOLS

---

## A

$\alpha$ = HPI

AIF= arterial input function

ASL= Arterial Spin Labelling

AT= arrival time

AUC= Area Under the curve

## B

BCLC= Barcelona Clinic Liver Cancer

## C

CA= contrast-agent

$C_b$ = concentration of contrast agent in whole blood

$C_e$ = concentration of contrast agent in the interstitial space

$C_p$ = concentration of contrast agent in plasma

$C_t$ = concentration of contrast agent in tissue

$C_A$ = concentration of contrast agent in the hepatic artery

$C_P$ = concentration of contrast agent in the portal vein

CC= conventional compartment model

CT= computed tomography

CV= coefficient of variation

## D

DCE= dynamic contrast-enhanced

DEB= drug-eluting beads

DP= distributed model

DSC=dynamic susceptibility contrast

## E

E= extraction ratio

EES= extravascular-extracellular space

## F

FA= flip angle

$F_A$ = tissue arterial blood flow

$F_P$ = tissue portal blood flow

$F_t$ = tissue blood flow

FLASH=Fast-Low Angle-Shot

## G

Gd= gadolinium

GRE= gradient-echo

## H

HBV= hepatitis B-virus

HCV= hepatitis C-virus

HCC= hepatocellular carcinoma

Hct=hematocrit

HPI= Hepatic Perfusion Index  
H(t)= cumulative frequency function  
h(t)= impulse outflow response

## **K**

$k_{ep}$ = transfer rate of contrast agent from the EES into plasma  
 $K^{trans}$ = transfer rate of contrast agent from plasma into the EES

## **M**

MAD= median absolute deviation  
MRI= magnetic resonance imaging  
MTE= mean time to enhance  
MDCT= multi-detector CT  
MTT= mean transit time

## **N**

NAFLD= non-alcoholic fatty liver disease  
NASH= non-alcoholic steatohepatitis

## **P**

PET= Positron emission tomography  
PBP= percentage baseline at peak  
PIF= portal input function  
PPI= portal venous perfusion index  
PS= permeability-surface area product

## **R**

$R_t(t)$ = tissue transfer function  
 $R_1$ = longitudinal relaxation rate of the tissue in the presence of the contrast-agent  
 $R_{10}$ = longitudinal relaxation rate of the tissue in the absence of the contrast-agent  
 $r_1$ = coherent longitudinal relaxivity of the contrast-agent  
RARE= rapid acquisition with refocused echoes

## **S**

S or SI= signal intensity  
 $S_0$ = relaxed signal  
SPGR= 3D fast spoiled gradient echo  
SD=standard deviation

## **T**

TAE= transcatheter arterial embolisation  
TACE= transarterial chemoembolization  
c-TACE= conventional TACE  
TR= repetition time  
TE= echo time  
TTP= time to peak  
 $T_1$ = inherent longitudinal relaxation time  
 $T_{10}$ = longitudinal relaxation time before the administration of contrast-agent

## **V**

$v_b$ = tissue blood volume fraction  
 $v_d$ = tissue distribution volume (single compartment models)

$v_e$  = tissue extravascular-extracellular volume fraction

$v_p$  = tissue plasma volume fraction

$v_t$  = tissue blood volume

# I. GENERAL INTRODUCTION

---

This thesis is submitted in fulfillment of the requirement for obtaining a PhD degree at the PhD school of Medicine at the Paris Descartes V University of Paris. The project was supervised by Professor Charles-Andr  CUENOD.

During this thesis, a multi-bolus injection scheme was proposed for the liver DCE-MRI analysis. This scheme was tested by a computer simulation showing the improvement of the robustness of the perfusion parameters' measurement. In continue, the same scheme was tested in-vivo, especially in rabbits bearing with VX2 tumor evaluating its feasibility by distinguishing the perfusion difference of tissues (liver, tumor border, tumor core) before and after the treatment procedure of embolisation.

## I.1 LIVER TUMOR – LIVER IMAGING – AND PERFUSION IMAGING

Liver tumor can be primary such as Hepatocellular carcinoma (HCC) or secondary such as metastasis from the intestine. These are common diseases but have very poor diagnosis. Many treatments are available from surgery to transcatheter arterial (chemo) embolization [TA(C)E] or conformal radiotherapy, but these treatments are effective when the lesions are small. Consequently, early detection of these lesions is important for improving care and early treatment. Furthermore, during treatment, tumor response assessment is important to adapt the therapeutic strategy.

In recent years, the most powerful imaging for the detection of small lesions is the functional imaging perfusion such as DCE-MRI, DCE-CT, and DCE-US that benefit the administration of contrast-agent and provide advanced detection of lesions and especially quantitative measurement deconvoluting the vascular input functions extracting the perfusion parameters (tissue blood flow-  $F_t$ , tissue blood volume-  $v_t$ , permeability-surface area- PS, interstitial volume-  $v_e$ , and mean transit time- MTT) that allow the evaluation of treatment efficacy.

The perfusion imaging in the liver tumor pathology has been tested for many years but has not been adopted in clinical practice due to both technical and physiological problems. First, the liver placed in the abdominal cavity, so it is affected by the respiration motion. Second, the liver consisted of two supplies; the hepatic artery, and the portal vein that implies additional perfusion parameters compared to other tissues, such as hepatic perfusion index (HPI) that indicates the arterial contribution in the liver. Third, the liver has also a specific circulatory network formed by

highly permeable capillaries (sinusoids) leading to rapid leakage of contrast-agent into the interstitial space that is a fast phenomenon but of small amplitude, therefore difficult to detect and analyze. In case of hepatic tumors, these characteristics are differentiated. Consequently, rapid DCE sequences are demanded for reliable detection of the lesions through the efficient separation between the arterial input function (AIF) and portal input function (PIF).

## **I.2 CONTEXT OF THE STUDY**

### **I.2.1 PARCC-INSERM-HEGP & MY LABORATORY**

My thesis was conducted at the Paris Cardiovascular Research Center (PARCC) from January 2016 to November 2019. It is in the 15<sup>th</sup> department of Paris near the Garigliano bridge and is attached to the Georges Pompidou European Hospital (HEGP). Since 2009, it is a joint research unit (UMR 970) of INSERM (9000 statutory researchers), and Paris Descartes University (4000 statutory). With an international vocation in the field of basic research on cardiovascular diseases, it consists of approximately 4100 m<sup>2</sup> of laboratories and technical platforms, for a total of 180 researchers. PARCC is divided into 13 research teams, each one with a specialization. Namely,

Team 1: Endothelial physiopathology and vascular extracellular vesicles

Team 2: In vivo imaging research

Team 3: Genetics to understand the physiopathology of arterial diseases

Team 4: Integrative Epidemiology of Cardiovascular Diseases

Team 5: Immuno-metabolic mechanisms of cardiovascular diseases

Team 6: Regenerative Therapies for Cardiac and Vascular Diseases

Team 7: Cellular, molecular and physiological mechanisms of heart failure

Team 8: Kidney and vascular signaling from development to disease

Team 9: Vascular development and disease

Team 10: Immunotherapy and anti-angiogenic therapy in oncology

Team 11: Multidimensional Approach in Organ Transplantation

Team 12: Genetic and metabolism of rare cancers

Team 13: Genetic Mechanisms of Aldosterone-Related Disorders

All these research teams involve also administrative and technical teams.

I have personally had the opportunity to work in the team 2 called also Imaging Research Laboratory (LRI), specialized in clinical and pre-clinical biomedical imaging and led by Prof. Bertrand Tavitian. This team consists of engineers, Ph.D students, post-docs, doctors, research professors and medical or engineering students. I joined the LRI to participate in the HECAM project.

## I.2.2 HECAM PROJECT (HEPATOCELLULAR CARCINOMA MULTI-TECHNOLOGICAL)

This thesis was financed by BPI France under the HECAM project [Hepatocellular Carcinoma Multi-Technological].

HECAM is a Competitive Research and Development Project (PSPC). It is funded by the Future Investments Program. The goal of this project is the development of tools for screening, diagnosis, and treatment of HCC (Hepatocellular Carcinoma) that is the primary stage of the liver cancer.

However, screening, diagnosis, and management of a pathology such as HCC require multiple complementary technologies. Therefore, the HECAM consortium led by General Electric Healthcare (GE Healthcare) is made up of multiple partners:

1. **An intermediate company (ETI)**; Guerbet
2. **Seven small and medium companies (SMEs)**; BioPredictive, CarThera and IntegraGen (IdF), BioSIMS Technologies (Upper Normandy), Intrasure (Languedoc-Roussillon), EDAP TMS France and Fluoptics (Rhône-Alpes)
3. **Three academic partners:**
  - a. Gustave Roussy, the first center for the fight against cancer in Europe,
  - b. Assistance Publique-Hôpitaux de Paris, and
  - c. National Institute of Health and Medical Research.

The consortium also relies on the University Hospital of Montpellier.

## I.2.3 COLLABORATIONS

During my thesis, I have had several collaborations with, namely:

- ❖ **Guerbet company**, Pharmaceutical company in Aulnay-sous-Bois, France; I attended a training on the VX2 tumor implantation in the rabbit liver
- ❖ **Archimmed company**, Paris, France; We collaborated on the VX2 tumor treatment experiments
- ❖ **Pathoanatomy department of the Georges-Pompidou Hospital**, Paris, France; We collaborated on the analysis of the histology images of the VX2 tumor post-embolization, during the VX2 tumor experiments for the reduction of the 2nd paper.
- ❖ **Interventional department of the Georges-Pompidou Hospital**, Paris, France; We collaborated on the performance of the transcatheter arterial embolization technique for the VX2 treatment, during the VX2 tumor experiments for the reduction of the 2nd paper.

## I.2.4 TRAINING ON ANIMAL EXPERIMENTATION

During the second year of my thesis, I attended a training entitled: “Animal Experimentation – Designer” based on the conception of the procedures on rodents’ and lagomorphs’ experimental animals. This training took place at the Institute Pasteur, in Paris and was approved by the Ministry of Agriculture.

## I.3 MAIN CONTRIBUTION OF THE THESIS

What we proposed and investigated was a multi (four)-bolus injection scheme for the improved perfusion analysis of the liver and the hepatic tumors implanted in rabbits applying the DCE-MRI technique.

Moreover, during my thesis, I have had the pleasure of attending several research meeting. Namely,

- ❖ 26<sup>th</sup> Annual Meeting ISMRM, June 2018, Paris, France
- ❖ Journée Francophone de Radiologie (JFR 2018), Octobre 2018, Paris, France
- ❖ Journée Scientifiques de l’école doctorale MTCl, June 2017, Paris, France
- ❖ Journée Francophone de Radiologie (JFR 2017), Octobre 2017, Paris, France
- ❖ Journée Francophone de Radiologie (JFR 2016), Octobre 2016, Paris, France
- ❖

## I.4 LIST OF PUBLICATIONS AND MEETINGS

### I.4.1 SCIENTIFIC PAPERS

The thesis was built on a basis of the following research papers and conference and meeting contributions:

- I. Multi-bolus injection to improve the robustness of Liver DCE-MRI: *a simulation study in rabbits*  
Sofia Veneti., Daniel Balvay., Gwennh el Autret., Charles A. Cuenod,

Submitted in Magnetic Resonance in Medicine

- II. Application of the four-bolus injections strategy using dynamic contrast-enhanced magnetic resonance imaging (DCE-MRI) to detect the effect of transcatheter arterial embolization (TAE) in VX2 liver tumor in rabbits

*Sofia Veneti, Imad Benkhaled, Daniel Balvay, Olivier Pellerin, Florentina Pascale, Tchao Méatchi, Charles A. Cuenod*

Manuscript in preparation

## I.4.2 CONFERENCE AND MEETING CONTRIBUTIONS

- ❖ Does multi-bolus injection protocol improve the DCE-MRI technique in the liver?

*Sofia Veneti, Daniel Balvay, Gwennhäel Autret, Charles A. Cuenod*

**Digital Poster presentation.** 27<sup>th</sup> Annual Meeting ISMRM, May 2019, Montreal, Canada

- ❖ Does multi-bolus injection protocol improve the DCE-MRI technique in the liver?

*Sofia Veneti, Daniel Balvay, Gwennhäel Autret, Charles A. Cuenod*

**Poster presentation.** 3e Congrès National d'Imagerie du Vivant (CNIV), February 2019, Paris, France

- ❖ Does multi-bolus injection protocol improve the DCE-MRI technique in the liver?

*Sofia Veneti, Daniel Balvay, Gwennhäel Autret, Charles A. Cuenod*

**Oral presentation.** Journées scientifiques de l'école doctorale MTCI, June 2018, Paris, France

- ❖ Does multi-bolus injection protocol improve the DCE-MRI technique in the liver?

*Sofia Veneti, Daniel Balvay, Gwennhäel Autret, Charles A. Cuenod*

**Oral presentation.** Annual meeting of the Paris Cardiovascular Research Center (PARCC), May 2018, Normandy, France

## II.CURRENT KNOWLEDGE ON THE LIVER AND MICROCIRCULATION IMAGING

---

### II.1 LIVER ANATOMY AND PHYSIOLOGY

#### II.1.1 MACROSCOPIC LIVER ANATOMY

The liver is the largest organ of body; approximately 2% to 3% of average body weight. Located in the right upper quadrant of the abdominal cavity underneath the right hemi-diaphragm and is protected by the rib cage.

The anatomy of the liver can be described using two different aspects: the morphological anatomy (Figure 1) and the functional anatomy (Figure 2). The traditional morphological anatomy is based on the external appearance of the liver and does not show the internal features of vessels and biliary ducts branching.

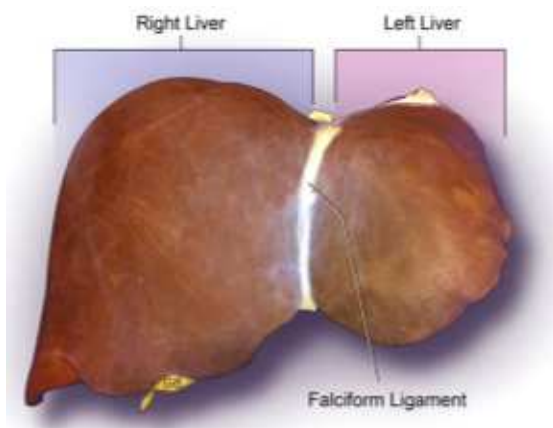


**Figure 1** : Morphological anatomy of the liver. <sup>1</sup>

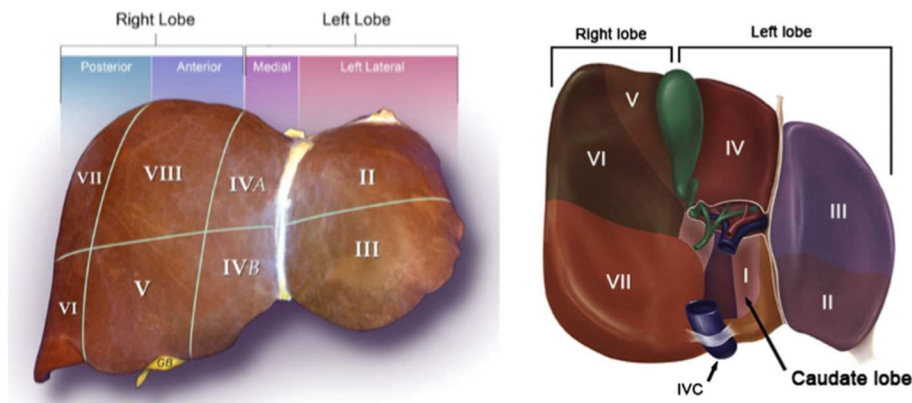


**Figure 2 :** Functional anatomy of the liver. (a) Anterior view, and (b) posterior view.

The French surgeon and anatomist Claude Couinaud was the first (1957) who divided the liver into eight functionally independent segments. Each segment has its own vascular inflow, outflow, and biliary drainage. In the center of each segment, there is a branch of the portal vein, the hepatic artery and bile duct (portal triad). In the periphery of each segment there is vascular outflow through the hepatic veins (Figure 3).

**Right hepatic vein** divides the right lobe into the anterior and posterior segments.

**Middle hepatic vein** divides the right lobe into right and left lobes.

**The Falciform ligament** divides the left lobe into median (segment IV) and lateral (segment II, III).

**The portal vein** divides the liver upper and lower segments.

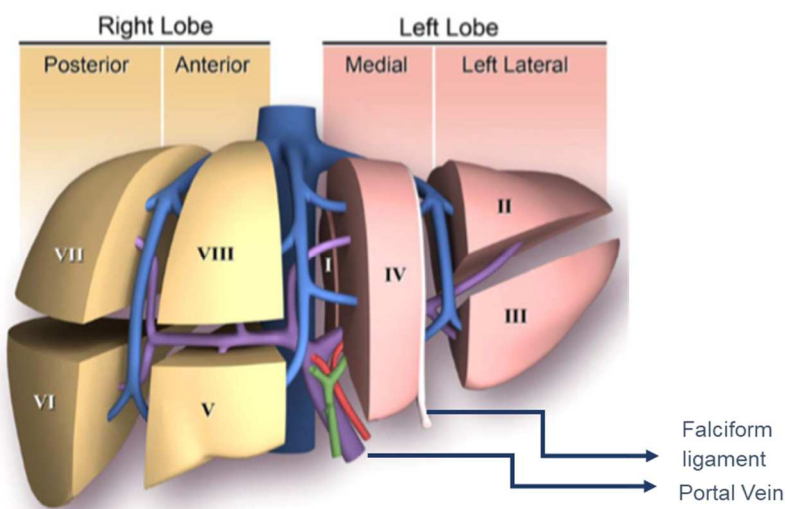


**Figure 3 :** Couinaud's segmentation of the liver. <sup>1</sup>

Looking at the liver in front, the segments VI and VII are not visible because they are located posteriorly. The right border of the liver is formed by segment V and VIII. Although, the segment IV is part of the left half of the liver, it is situated mainly to the right. It is also divided into segment IVa and IVb according to Bismuth <sup>2</sup>. The numbering of the segments is in a clockwise manner.

## **II.1.2 HEPATIC VASCULATURE**

The liver is a very vascular organ and at rest receives up to 25% of total cardiac output, more than any other organ. It has also a special circulatory system. It is vascularized by a double blood supply: the hepatic artery and the portal vein. The hepatic artery is oxygenated blood and contributes 25% to 30% of the blood supply. The remaining 70% to 75% is distributed by the portal vein which derives the spleen, stomach and intestine. The arterial and portal blood mix within the hepatic sinusoids before draining into the systematic circulation via the hepatic veins.

### ***Arterial Vasculature***

The arterial vasculature of the liver is variable. In Figure 4, it is depicted the most common arterial pattern. The common hepatic artery originates from the celiac axis along with the left gastric and splenic arteries. The common hepatic artery continues laterally and branches into the proper hepatic artery and the gastroduodenal artery. The proper hepatic artery is divided into left and right hepatic arteries to feed the respective hepatic lobes.

### ***Venous Vasculature***

The portal vein provides the greatest part of the blood supply to the liver. As presented in Figure 5, the portal vein forms from the intersection of the superior mesenteric vein and splenic vein behind the area of the pancreas. The portal vein is valveless and is a low-pressure system with pressure commonly 3 to 5 mm Hg. The main portal vein traverses cranially towards the liver and is divided into the left and right portal veins near the liver hilum. The left portal vein has two portions. The right portal vein often appears closer to or within the hepatic parenchyma of the right liver itself. It quickly splits up anterior and posterior branches to segments V and VIII and segments VI and VII, respectively (Figures 2; and Figure 6).

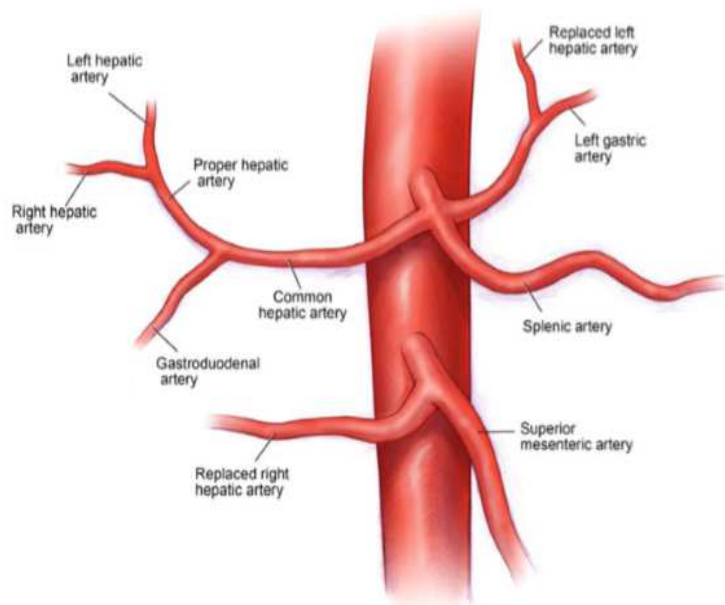


**Figure 4:** Liver arterial supply. <sup>1</sup>

The venous drainage of the liver (Figure 5) is through the intrahepatic veins that basically derive from three hepatic veins that drain into the Inferior Vena Cava (IVC). The left and middle hepatic veins may drain directly into the IVC. The right hepatic vein is typically larger, with a short extrahepatic track and drains directly into the IVC.

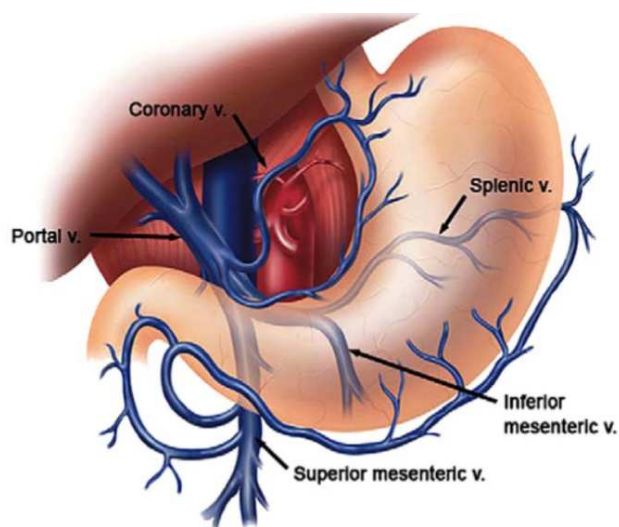


**Figure 5 :** Vasculature inflow of portal vein. <sup>3</sup>

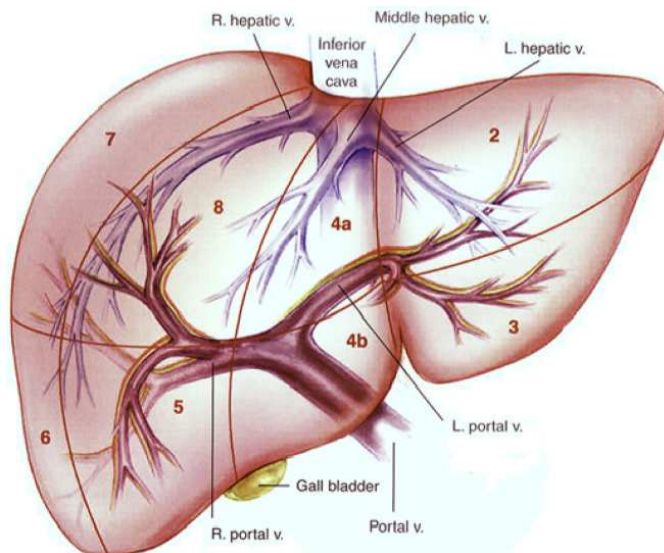


**Figure 6** : Intrahepatic vascular anatomy, anterior view. <sup>3</sup>

### **II.1.3 MICROSCOPIC ANATOMY OF THE LIVER**

The liver is a complex three-dimensional structure that consists of epithelial and mesenchymal elements structured in repetitive microscopic units. Such a structural and functional organization allows assessment of diffuse disease processes in small representative histology specimens.

#### ***Classic Lobule, Portal Lobule and Liver Acinus***

The liver is organized into lobules. Each lobule has a hexagonal appearance and is centered on a branch of the hepatic vein (the central vein). Portal triad consists of the portal vein, the hepatic artery, and the bile duct (Figure 7). In the lobules, blood flows from the periphery to the center of the lobule into the central vein.

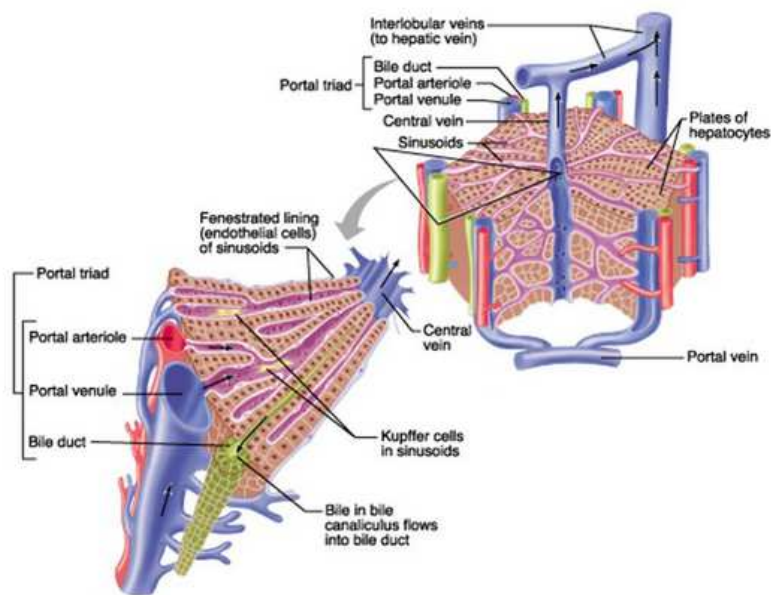


**Figure 7** : Microscopic anatomy of the liver.<sup>4</sup>

There are three different ways to classify the liver micro-anatomy; classic lobule, portal lobule, and hepatic acinus.

The **classic lobule** (Figure 8a) is an anatomic model as long as having the central vein in the middle and around it is the portal triads. In the classic lobule, the hepatic artery diffuses blood across cells into central vein. The portal vein supply, that comes from the intestine, stomach, and spleen, goes across the liver through the central vein, as well. Finally, the bile drains in the opposite direction from the central vein to the bile duct. *The central vein goes up from the liver to the inferior vena cava (IVC) and then to the body.*

The **portal lobule** model (Figure 8b) focus on the bile excretion. The portal lobule is made up of a triangle connecting three adjacent central veins of three classic lobules side by side where in the middle of that triangle takes place the portal triad. Consequently, in the portal lobule, the bile drains from the periphery (central vein) to the center of the triangle (portal triad-bile duct).

The **hepatic acinus** (Figure 8c) is typically diamond-shaped where the central veins are at one end of the diamond and at the other end of the diamond is the portal triad. The hepatic acinus demonstrates the blood flow that comes from the hepatic artery and the portal vein. This blood flow accurately describes zones. More specifically, Zone I (periportal zone) takes place between two portal triads and delivers the richest in oxygen blood supply in cells. Zone II (intermediate zone) is lesser oxygenated blood supply. Zone III (pericentral zone) is right next to the central vein. It is the furthest way from the oxygen-rich blood supply.

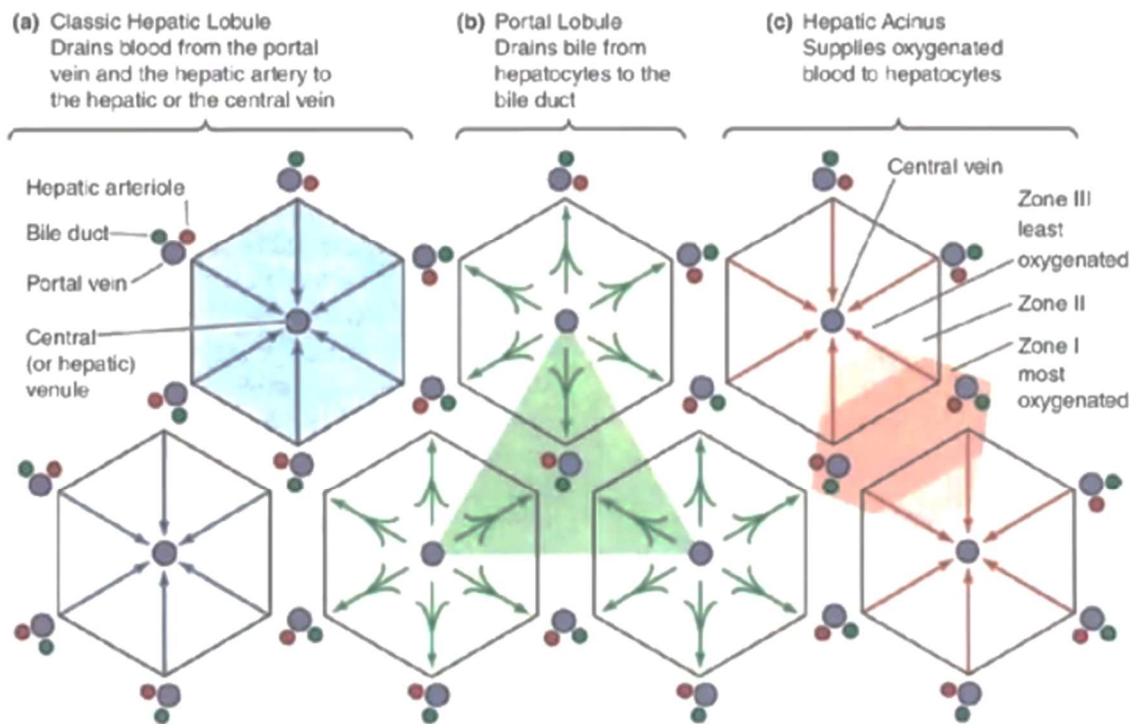


Figure 8 : The three concepts of the microscopic liver anatomy. <sup>3</sup>

### ***Hepatic cords, Hepatic sinusoids and Space of Disse***

Within each lobule, epithelial hepatocytes are arranged into hepatic cords separated by adjacent sinusoids. The cords of hepatocytes represent the parenchyma of the liver.

In cross section, hepatic cords appear linear (hence the name « cords »). However, they are not strings of cells; they look like branching and interconnecting sheets which extend parallel to the long axis of the lobule and radiate out from its center.

The sinusoids are vascular spaces lined by a fenestrated endothelium (i.e. an endothelium that is full of holes- from *fenestra*, window) (Figure 9). This endothelium has no underlying basement membrane. Therefore, the fenestrations allow blood plasma to leak freely into the Space of Disse. Fenestrae are dynamic structures. They contract and dilate in response to alternations of sinusoidal blood flow and perfusion pressure. They also act as a selective barrier to control the extensive exchange of material between the blood and the liver cells and vice versa. Furthermore, they contribute to the homeostatic control of the hepatic microcirculation. Finally, the fenestrae remove from the blood any macromolecular waste product.

The space between the endothelium and the cords is named **space of Disse (or interstitial space)**. Its location allows the hepatocytes to keep together, since contains a network of reticular fibers such as collagen.

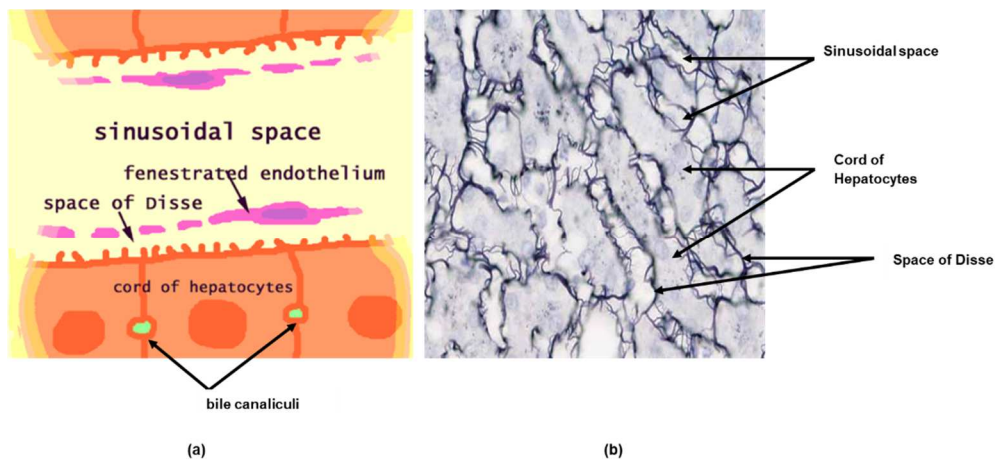


**Figure 9:** (a) Depiction of sinusoidal space and space of Disse. (b) Histology image of Space of Disse. Reticular fibers are stained black with silver. Hepatocytes are weakly stained. <sup>5</sup>

Finally, stellate **Kupffer cells** or liver macrophages located in the liver, lining the wall of the sinusoids. The role of these cells is to catch and destroy bacteria which entered the intestine (Figure 7; Figure 10).

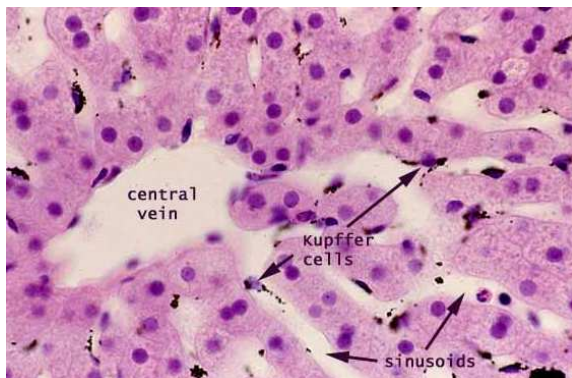


**Figure 10 :** Histology image-Kupffer cells' depiction. Kupffer cells can be recognized by their oval nuclei closely associated with sinusoidal spaces. <sup>5</sup>

## II.1.4 LIVER PHYSIOLOGY

The liver plays a major role in metabolism. It is the backbone of protein metabolism, carbohydrate and lipid metabolism. Furthermore, the human liver is responsible for up to 500 separate functions, usually in combination with other systems and organs. Some of them are the glycogen storage, the plasma protein synthesis and the drug detoxification. The functions of the liver are carried out by the liver cells or hepatocytes. Finally, the liver produces the bile, which is important for digestion.

### ***Bile and Bile Acids***

Bile is a bitter-tasting, dark-green to yellowish brown fluid produced by the liver that helps the process of digestion of lipids in the small intestine. Bile is stored in the gallbladder and while eating, it is discharged into the duodenum through the bile duct. The main components of bile are lipids, cholesterol, bile salts and lecithin. These are basically all secreted together in micelles (Figure 11). Cholesterol is placed at the core of a micelle and is the starting molecule in the synthesis of bile acids.

Initially, the micelles are composed entirely of bile acids. These are called primary micelles. These cannot absorb much cholesterol but are able to take up phospholipid. As the micelle takes up more phospholipid it will become a mixed micelle. Generally, the micelles will grow as they absorb more phospholipid. Micelle formation determines the volume of bile secreted.

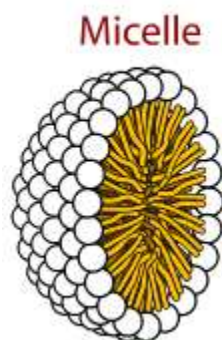


**Figure 11:** Depiction of micelle <sup>6</sup>

Furthermore, bile acts as a detergent helping to emulsify the fats in the food through the process of conjugation. **Conjugation** is basically a process that occurs inside hepatocytes and by which molecules have another molecule (usually glycine or taurine) adhered to them, which then makes them water soluble. In other words, the basic point of conjugation is to give the molecule a negative charge which will make it hydrophilic. It usually occurs in two steps: in the first step,

the molecule is polarized. Then, in the second step, it is fully conjugated and given an overall negative charge. The main thing that liver conjugates is bile salt.

**Bile salts** are the conjugated form of bile acid, and thus, bile acids are what we circulate in our blood, and bile salts are what we secrete in bile. The **bile salts** are charged with a hydrophobic end and a hydrophilic end (Figure 12). When they are exposed to water mixed with fat, such as in the small intestine, the bile salts gather around a fat droplet with their hydrophilic side pointing towards water. This process increases the surface area of the fat and allows greater access by the pancreatic enzymes that break down fats (fat digestion). Bile salts also act as bactericides, destroying many of the microbes that may be present in the food.

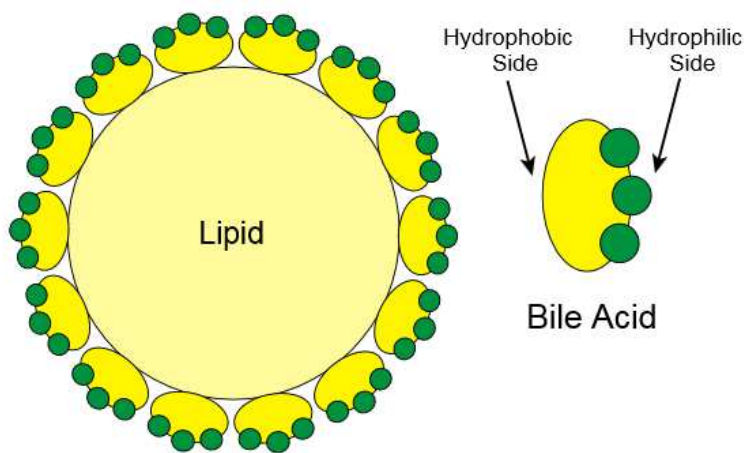


**Figure 12** : Bile salts congregate around fat and separate them into small droplets called micelles.<sup>7</sup>

Except for its digestive function, bile serves also as the route of excretion for bilirubin, a waste byproduct of red blood cells that is recycled by the liver. Unconjugated bilirubin cannot be excreted at all. Once bilirubin has been conjugated in hepatocytes, some may escape into blood and be excreted in the urine-giving urine its color.

## ***Protein Metabolism***

In contrast to muscle cells, which synthesize protein for their own use, hepatocytes synthesize proteins for the whole organism. Many of the circulating proteins are synthesized by hepatocytes. The liver carries out four main functions in protein metabolism: formation of plasma proteins, transamination and deamination of amino acids and urea synthesis (for ammonia excretion).<sup>8</sup>

### *Plasma protein formation*

The liver manufactures a wide spectrum of proteins. Over 80% of the proteins synthesized by the liver are exported into the systemic circulation. These proteins play important role to the

maintenance of hemostasis, oncotic pressure, transportation of hormones, lipid transport and acute phase responses. Total hepatic plasma protein synthesis varies between 30 and 60 gr a day.

### *Transamination and Deamination of amino acids*

The amino acids undergo common reactions like transamination followed by deamination for the liberation of ammonia<sup>9</sup>.

### *Urea formation*

Interconversion and degradation of amino acids results in ammonia production. Ammonia removal occurs mainly via urea synthesis and subsequent excretion by the kidneys. Ammonia (ammonium ion) is very toxic and if not rapidly and efficiently removed from the circulation will result in central system disease.

## ***Carbohydrate metabolism***

The liver plays a crucial role in maintaining blood glucose levels. Following consumption of food, extra glucose can be stored within the liver as glycogen (large polymer). This process called **glycogenesis**. Then, when blood concentrations of glucose begin to decrease the liver activates other pathways which lead to depolymerization of glycogen (**glycogenolysis**) and export of glucose back into the blood for transport to all other tissues. It is important to notice that glycogenolysis is not a direct change of synthesis.

Finally, the liver can convert amino acids, lactate, pyruvate and glycerol into glucose via **gluconeogenesis**. Gluconeogenesis is stimulated by cortisol and glucagon, and constrained by insulin<sup>10</sup>.

## ***Lipid metabolism***

Within each liver lobule, there is zonation of the metabolic functions. The periportal zone is where oxidative energy metabolism, amino acid catabolism, cholesterol metabolism, and fatty acid-oxidation take place. Specially, fatty acids are synthesized within the cytoplasm of hepatocytes from Acetyl-CoA. On the other hand, the perivenous zone is where de novo lipid synthesis, ketogenesis and xenobiotic metabolism take place.

**Lyposynthesis** occurs by esterification of free fatty acids via acetyl-CoA and glycerol and is driven by glycerophosphate acyltransferase (GPAT), which is activated by nutritional status and insulin and prevented by glucagon.

**De novo lipogenesis of free fatty acids** from acetyl-CoA is regulated by insulin via activation of sterol regulatory element-binding protein-1c (SREBP-1c), which controls the transcription of lipogenic enzymes such as fatty acid synthesis.

### ***Storage Functions of the Liver***

Glucogen is stored in the liver via the glucogenesis process (carbohydrate metabolism). Lipid-soluble vitamins A, D, E, K are also stored in the liver as vitamin B12. Finally, iron and copper minerals are stored in the liver and the liver plays the role of regulator on these elements. Namely,

**Iron:** the liver regulates iron hemostasis and is the main body store for iron. Iron is taken up by enterocytes in a highly regulated way. Intestinal iron absorption is regulated by hepcidine, which is mainly produced by hepatocytes and to a lesser amount by adipocytes and macrophages. Hepcidine concentrations increase under inflammatory conditions or iron overload and decrease in case of anemia or hypoxic conditions.

**Copper:** copper is essential for life as it plays a key role as a co-factor for various enzymes. "As copper is cytotoxic, it is accompanied by specific protector proteins, which carry and transfer copper to its intracellular destination".<sup>6</sup>

### ***The liver as a detoxifier***

The liver is the central organ for detoxification of exo- and endogenous products. While water-soluble substances can be excreted by the kidneys, lipophilic substances must be transformed in the hepatocytes before excretion.

Filtering the blood is an essential detoxifying function of the liver, as the blood is stuffed with bacteria, endotoxins, and other toxic substances from the intestines. A healthy liver clears almost 100% of bacteria and toxins from blood before the blood enters general circulation.

The second essential detoxifying role of the liver involves a two-step enzymatic process for the neutralization of unwanted chemical compounds, such as drugs, pesticides and enterotoxins from the intestines. Phase I enzymes directly neutralize some of these chemicals, but some others are converted to intermediate forms and then processed by Phase II enzymes. These intermediate forms are often much more chemically active and thus, more toxic than the original substances.<sup>11</sup>

The third essential detoxifying role of the liver is synthesis and secretion of bile. Bile effectively eliminates toxic substances from the body and emulsifies fats and fat-soluble vitamins in the intestine, improving their absorption. When excretion of bile is prevented (cholestasis), toxins remain in the liver longer, subjecting the liver to damage.

## II.2 HEPATOCELLULAR CARCINOMA

### II.2.1 LIVER TUMORS

Malignant liver tumors can be divided into two categories: primary and secondary lesions. Hepatocellular carcinoma is the most common primary malignant tumor derived from hepatocytes. Its geographic distribution is heterogenous with highest incidence in developing countries due to its risk factors. Other malignant primary liver lesions include cholangiocarcinoma, epithelioid hemangioendothelioma, angiosarcoma, etc. Moreover, liver is the most common site of metastasis of digestive cancers, especially colorectal cancer. Generally, around 70% of patients with colorectal cancer will develop metastasis in the liver <sup>12</sup>.

### II.2.2 HEPATOCELLULAR CARCINOMA (HCC)

Hepatocellular carcinoma (HCC) is primary liver cancer and the fifth most common cancer, and the second in terms of mortality <sup>13</sup>. HCC rarely occurs before the age of 40 years and reaches a peak at approximately 70 years of age. More than 700 000 cases of this cancer were diagnosed worldwide in 2008. HCC is the most frequent cause of death in patients with cirrhosis.<sup>14</sup>

#### ***Hepatocarcinogenesis and risk factors***

Any cause of chronic liver inflammation leads to fibrosis and cirrhosis, characterized by annular fibrosis surrounding regenerative nodules. Accumulation of mutations in hepatocytes DNA and modifications in nodules blood supply (decrease of portal blood supply and increase of arterial blood supply) are responsible for the transformation of regenerative nodules into dysplastic nodules (low and high grade) and finally HCC. Vascularization of HCC is characterized by predominant arterial blood supply.

Then, in most cases, HCC develops within an established background of chronic liver disease (70-90% of all patients). Chronic HBV infection, accounting for more than 50% of all cases, is the most common risk factor across the world.

In south-east Asia and sub-saharian Africa, where 80% of HCC arise (Figure 13), the dominant risk factor is chronic infection with hepatitis B virus (HBV), together with exposure to aflatoxin B1.

By contrast, in North America, Europe and Japan, diabetes and non-alcoholic fatty liver disease (NAFLD) and its inflammatory condition called “non-alcoholic steatohepatitis” (NASH) are emerging risk factors. Other classic but declining risk factors include alcohol and chronic infection with hepatitis C virus (HCV).

HCC can be developed in patients with chronic HBV infection but without cirrhosis, because of host DNA mutations induced by HBV genoma integration. NASH may also be a risk factor of HCC independent of background cirrhosis.

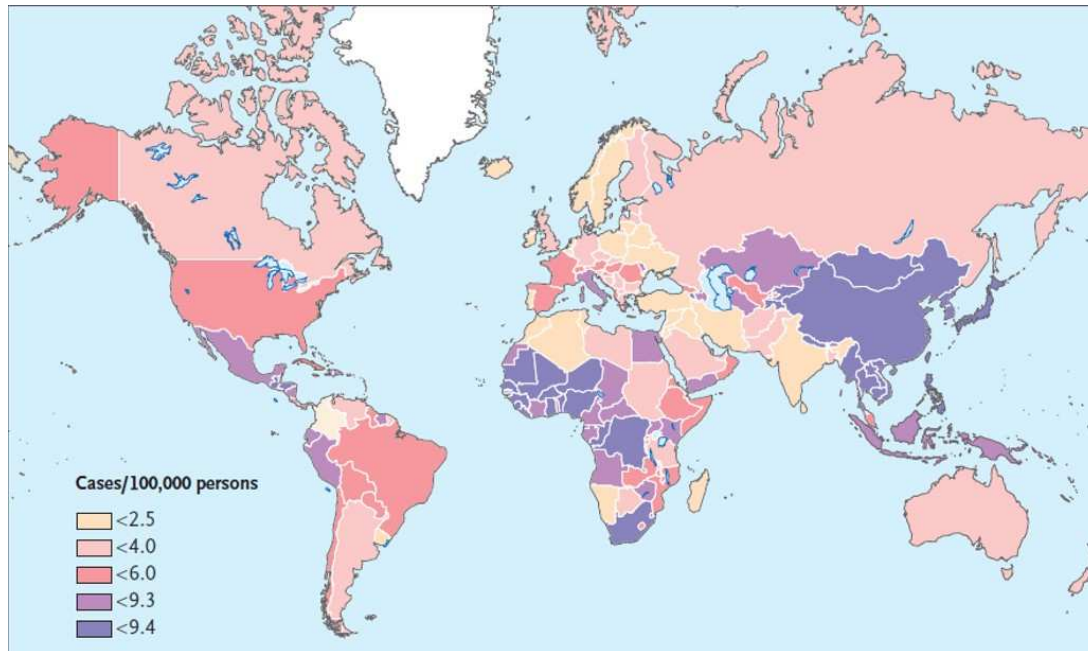


**Figure 13** : Regional variation in the incidence rates of liver cancer. The incidence rates shown pertain to both sexes and all ages. Adapted from the World Health Organization.<sup>13</sup>

## **Prevention**

HCC related to HBV can be however prevented by vaccination. If infection is chronic, viral replication can be abolished by antiviral agents, which would prevent progression of liver disease and, possibly, HCC in the long term<sup>14</sup>.

The incidence of HCC in individuals with HCV cirrhosis is 3-5% per year. Prevention of HCV infection relies on avoidance of viral transmission through contaminated blood. Interruption of evolution from acute infection into chronic hepatitis and, mainly, cirrhosis by using antiviral agents should prevent development of HCC. However, if cirrhosis is established, risk of HCC persists despite antiviral treatment.

## **Screening**

Screening of HCC aims to reduce disease-related mortality. Early detection and treatment of hepatocellular carcinoma is the sole option to achieve long-term disease-free survival. The decision to begin surveillance depends on the degree of risk of HCC for the individual and the extent to which he or she would be treated if diagnosed with liver cancer. Patients with HCC

identified by screening present with smaller tumors and are more likely to undergo a curative procedure<sup>15-17</sup>. Due to its risk factors, all patients with cirrhosis or chronic HBV infection are eligible for HCC screening. A recent meta-analysis concluded that despite poor-quality evidence, HCC screening increased the life expectancy of patients with cirrhosis<sup>18</sup>. However, a systematic review concluded that there was insufficient evidence to recommend surveillance<sup>19</sup>. Because clinicians who care for patients with liver disease all too often see unscreened patients presenting with advanced HCC, an a priori argument can be made that patients at risk should undergo surveillance, at least until there is evidence that surveillance is inefficient<sup>20</sup>. The preferred imaging method for surveillance is ultrasonography; it is well tolerated and widely available, and it has sensitivity of 60-80% and specificity beyond 90% for early detection.<sup>18</sup> Computed tomography (CT) and magnetic resonance imaging (MRI) are not recommended for screening because of radiation risks, high cost, and lower availability<sup>20</sup>. The best screening interval is 6 months<sup>21-24</sup>. A 3-month interval increases detection of small nodules but has no effect on survival<sup>25</sup>, and twice-yearly screening (every 6 and 12 months) has better results than annual<sup>26,27</sup>.

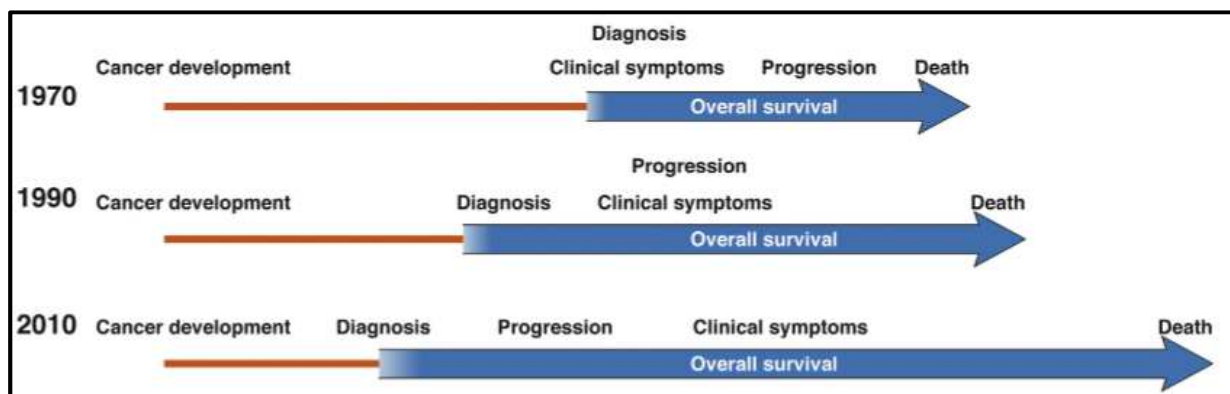


**Figure 14 : Changes in diagnosis of HCC over time.**<sup>20</sup>

*“Years ago, techniques such as ultrasonography, computed tomography, and magnetic resonance imaging were not available. Therefore, HCC was almost always diagnosed when the cancer produced symptoms. Progression registration, either symptomatic or at mere palpation or imaging, would closely precede death. Years later, it became feasible to diagnose HCC at earlier stages, before symptoms developed. Registration of progression was no longer so close to death. Patients are now diagnosed with early-stage disease due to surveillance programs. “*

## **Diagnosis**

Contrary to many other malignancies, HCC non-invasive diagnosis is possible, using imaging criteria validated by the European Association for Study of the Liver (EASL)<sup>28</sup> and the American Association for the Study of Liver Diseases (AASLD)<sup>29</sup>. These guidelines are summarized in Figure 16.

Once a nodule has been detected by ultrasonography in patients with cirrhosis or chronic HBV infection, further imaging strategy depends on its size. Nodules 1cm or smaller are almost

impossible to diagnose confidently by available techniques (biopsy could miss the target and specific radiologic findings are often missing at this stage): ultrasonographic monitoring at 3-4 months is the recommended option in this situation.

When the nodule exceeds 1cm, non-invasive diagnosis of HCC can be established by CT or MRI (contrast-enhanced ultrasonography has not yet been validated by European and American guidelines). Indeed, HCC CT or MR imaging pattern is in most cases specific enough to avoid biopsy. In patients with established liver cirrhosis or chronic HBV infection, any supracentimetric nodule presenting with intense enhancement during arterial phase followed by contrast wash-out during portal or delayed phases is HCC. If the first modality of imaging (CT or MRI) is not conclusive, the second must be achieved. Despite their high specificity (near 100%), these typical imaging features have lower sensitivity (around 71%) for nodules < 2cm. Biopsy is required in cases showing atypical radiologic presentations or in the absence of chronic liver disease, to achieve final diagnosis.

### ***Imaging management of liver nodules and LI-RADS***

As seen previously, the most specific radiologic features of HCC are provided by dynamic contrast-enhanced imaging, showing wash-in or hypervascularity (intensity or density superior to adjacent liver in arterial phase) and wash-out (intensity or density inferior to adjacent liver in portal or delayed phase). But other imaging findings, less specific, may help achieving radiologic diagnosis, such as pseudocapsule (annular enhancement around the nodule in delayed phase), presence of fat or iron component within the lesion, endovascular or biliary invasion, restriction of diffusion, blood products within the mass, and nodule-in-nodule appearance.

Most of these features have been recently considered in the new Liver Reporting and Data System validated in 2018 by the American College of Radiology (ACR)<sup>30</sup>. It facilitates and standardizes terminology and radiologic evaluation of liver nodules among patients with cirrhosis or chronic HBV infection or history of HCC. This score varies between 1 to 5. LI-RADS 1 or 2 nodules correspond to benign lesions whereas LI-RADS 3 or more nodules show significant risk of malignancy, corresponding to a high predictive value of HCC. It considers the size (and the growth) of the nodule, its arterial phase non-peripheral hyperenhancement, its non-peripheral wash-out and an enhancing capsule. Another category defined by LI-RADS is LI-RADS M, for nodules showing high probability of malignancy but not necessarily HCC.

Moreover, LI-RADS provides guidelines for nodules management according to their score: biopsy may be required for LI-RADS 4 and M nodules and HCC is confirmed for LI-RADS 5 nodules.

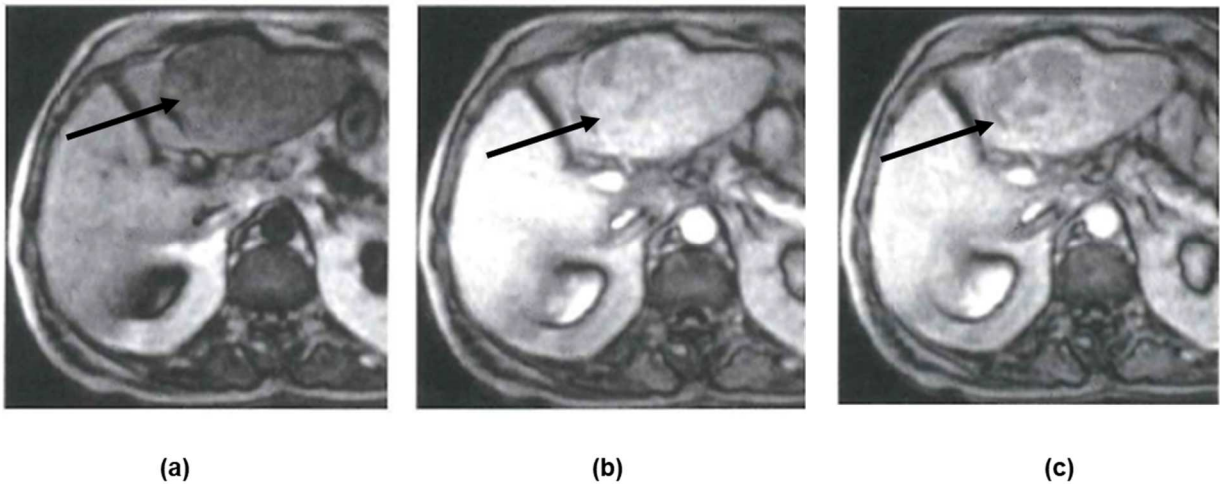


**Figure 15 :Large HCC tumor** (black straight arrow). Dynamic T1-weighted GRE sequence (TR/TE/FA=154ms/6ms/70°). (a) Before injection, a hypo-intense signal lesion presented with a hypo-intense pseudo-capsule. (b) 15 seconds post-injection of gadolinium, the HCC shows a hyper-vascular appearance with a non-enhancing capsule. (c) 5 minutes post-injection of gadolinium a more hypo-intense enhancement of the tumorous lesion depicted with the beginning of enhancement of parts of the capsule.

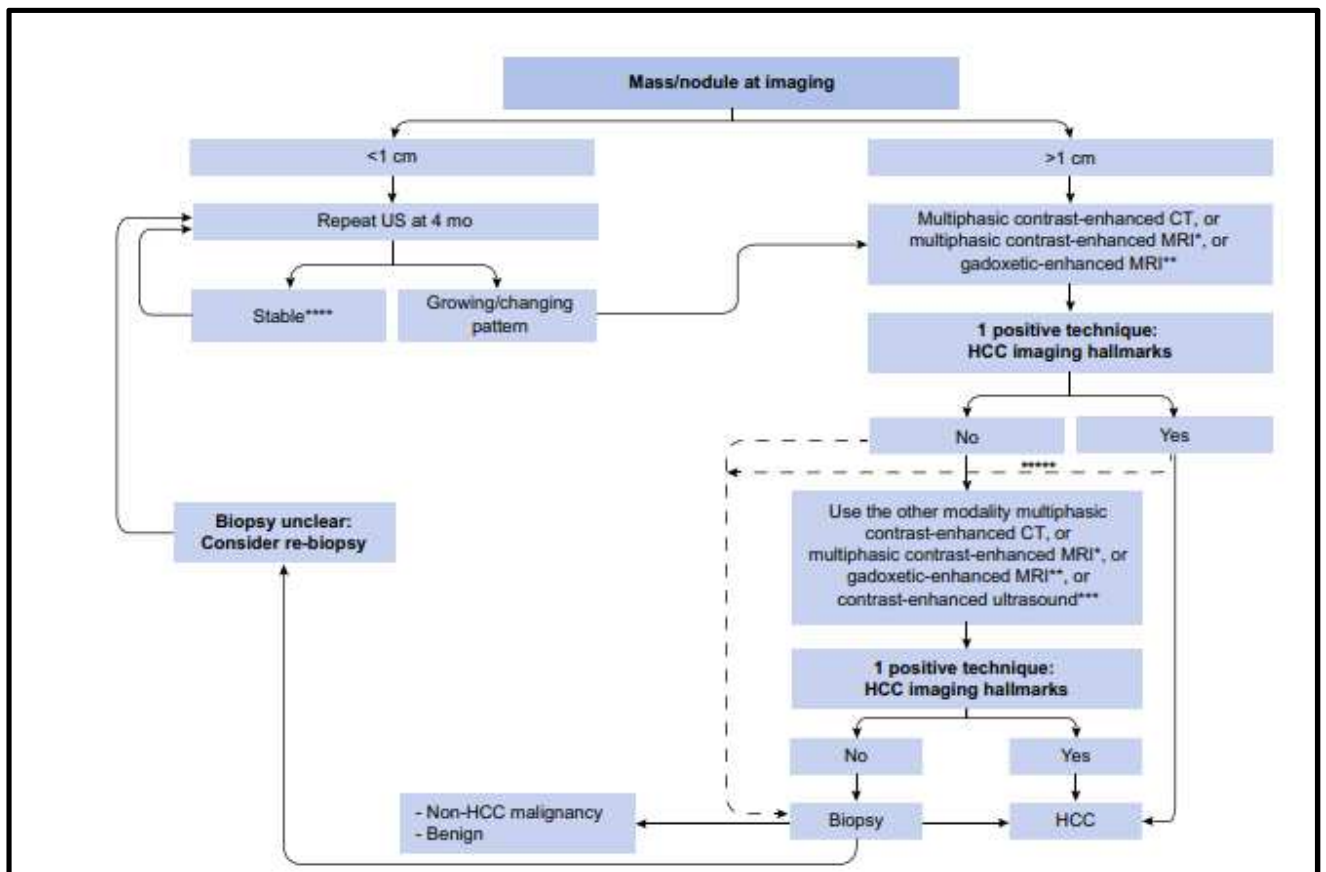


**Figure 16 : Diagnostic algorithm for HCC in expert centers**<sup>28</sup>

*\*Using extracellular MR contrast agents or gadobenate dimeglumine. \*\*Using the following diagnostic criteria: arterial phase hyperenhancement (APHE) and washout on the portal venous phase. \*\*\*Using the following diagnostic criteria: arterial phase hyperenhancement (APHE) and mild washout after 60 s.*

\*\*\*\*Lesion<1 cm stable for 12 months (three controls after four months) can be shifted back to regular six months surveillance. \*\*\*\*Optional for centre-based programmes.  
CT=computed tomography, MRI= magnetic resonance imaging.

## **Staging and prognosis assessment**

Assessment of prognosis is a crucial step in management of patients with HCC. Years ago, most affected patients were diagnosed at an advanced symptomatic stage, when treatment was not feasible and short-term prognosis was dismal<sup>14</sup>. Diagnosis has now advanced, and effective early treatment of patients is associated with median survival beyond 5 years<sup>14</sup>. Any attempt to assess prognosis should account for tumor stage, degree of liver function impairment, and presence of cancer-related symptoms<sup>31</sup> otherwise the clinical usefulness is limited.

The classification that stratifies patients with HCC according to outcome and simultaneously links it with treatment indication is the Barcelona Clinic Liver Cancer (BCLC) strategy (Figure 17)<sup>32</sup>. The BCLC staging system is a useful assessment tool that incorporates data on the patient's performance status, number and size of nodules, cancer symptoms, and liver function as determined by the Child-Pugh classification system.

End-stage patients are identified easily by any clinical method. They have a very poor prognosis and no intervention will be of benefit. Patients with end-stage liver disease (Child-Pugh C or advanced Child-Pugh B) should be considered for transplantation, but recognition of HCC could become a contraindication because of excessive tumor burden. Between these two extreme situations, the clinical profile is very heterogeneous. The BCLC classification<sup>33</sup> divides this heterogeneous group into two categories: the intermediate stage (BCLC B), defined by absence of any adverse predictor, and the advanced stage (BCLC C), which includes patients with symptoms, vascular invasion, extrahepatic spread, or a combination.

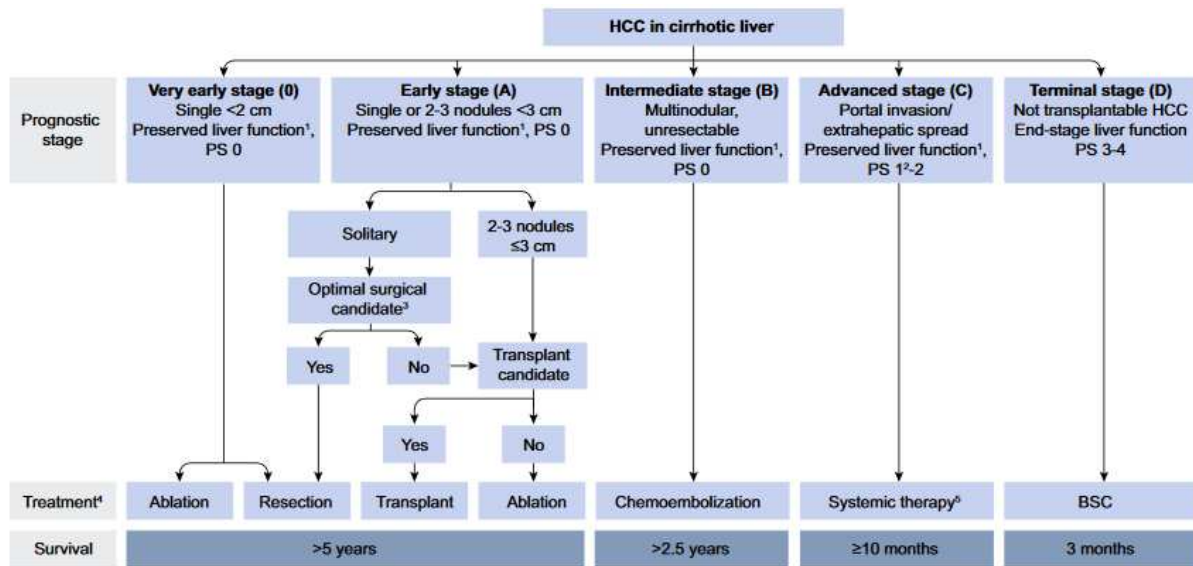


**Figure 17 : Modified BCLC staging and treatment strategy<sup>28</sup>**

<sup>1</sup> “Preserved liver function” refers to Child-Pugh A without any ascites, considered conditions to obtain optimal outcomes. This prerequisite applies to all treatment options apart from transplantation, that is instead addressed primarily to patients with decompensated or end-stage liver function. <sup>2</sup> PS 1 refers to tumor induced (as per physician opinion) modification of performance capacity. <sup>3</sup> **Optimal surgical candidacy** is based on a multiparametric evaluation including compensated Child-Pugh class A liver function with MELD score<10 to be matched with grade of portal hypertension, acceptable amount of remaining parenchyma and possibility to adopt a laparoscopic/minimally invasive approach. The combination of the previous factors should lead to an expected perioperative mortality <3% and morbidity<20% including a postsurgical severe liver failure incidence<5%. <sup>4</sup> The **stage migration strategy** is a therapeutic choice by which a treatment theoretically recommended for a different stage is selected as best 1st line treatment option. Usually it is applied with a left to right direction in the scheme (i.e. offering the effective treatment option recommended for the subsequent more advanced tumour stage rather than that forecasted for that specific stage). This occurs when patients are not suitable for their first line therapy. However, in highly selected patients, with parameters close to the thresholds defining the previous stage, a right to left migration strategy (i.e. a therapy recommended for earlier stages) could be anyhow the best opportunity, pending multidisciplinary decision. <sup>5</sup> As of 2017 sorafenib has been shown to be effective in first line, while regorafenib is effective in second line in case of radiological progression under sorafenib. Lenvatinib has been shown to be non-inferior to sorafenib in first line, but no effective second line option after lenvatinib has been explored. Cabozantinib has been demonstrated to be superior to placebo in 2nd or 3rd line with an improvement of OS from eight months (placebo) to 10.2 months (ASCO GI 2018). Nivolumab has been approved in second line by FDA but not EMA based on uncontrolled phase II data.

ASCO: American Society of Clinical Oncology; BCLC:Barcelona Clinic Liver Cancer; EMA: European Medicines Agency; FDA: Food and Drug Administration; MELD: model for end-stage liver disease; PS: performance status; OS: overall survival

## Treatment

The choice of the best treatment is complex, depending on patient-related factors (performance status, liver function, portal hypertension), disease-related factors (number, size and

intrahepatic distribution of lesions, vascular invasion and extra-hepatic spread). The BCLC staging system is a useful tool for treatment allocation (Figure 18).

The only curative treatment for HCC is liver transplantation, allowing tumor removal and preventing liver relapse by “treatment” of cirrhosis, but the lack of donors makes this option less available.

In this context, many percutaneous ablation techniques have been validated for first-line therapy, such as radiofrequency ablation (RFA) and percutaneous ethanol injection (PEI).

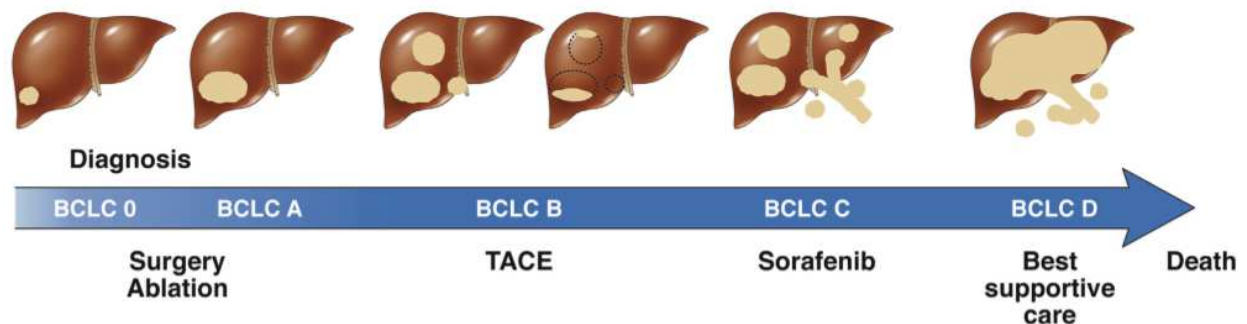


**Figure 18** : Development of HCC and first-line treatment options for each stage.<sup>20</sup>

### *BCLC Stage 0*

At this stage, surgery is no longer the only first-line treatment. Resection, transplantation, and ablation provide excellent results for single lesions  $\leq 2\text{cm}$  (T1 stage) in patients with preserved liver function<sup>34–37</sup>. Rates of 5-year survival range from 60% to 80%<sup>38,39</sup>.

### *BCLC Stage A*

Resection and transplantation produce the best outcomes for well-selected candidates with HCC stage A. Treatment should be chosen based on predicted immediate-term and long-term survival.

Transplantation should be considered for patients with clinically significant portal hypertension; 70% of patients survive for 5 years with adherence to the Milan criteria<sup>40</sup> (single HCC  $\leq 5\text{cm}$  or  $\leq 3$  nodules each  $\leq 3\text{cm}$  and no macrovascular invasion on imaging). Patients who are not suitable for surgery because of comorbidities should be considered for treatment with ablation. The major limitation for successful transplantation is organ shortage. Resection, ablation, chemoembolization, and radio-embolization are commonly used to avoid unacceptable progression (bridge therapy).

Radiofrequency (RFA) is now the first-line ablation technique, and microwave ablation is potentially a competitor. Ethanol injection provides less local control but still has a role in achieving a complete response when there is minimal residual viable tissue. All techniques

achieve the same effectiveness and survival in solitary HCC  $\leq 2$ cm, with portal hypertension as the main determinant of outcome.

### *BCLC Stage B*

Patients with BCLC stage B should be considered for transarterial chemoembolization (TACE). Conventional TACE (c-TACE) involves intra-arterial infusion of chemotherapy (usually doxorubicin or cisplatin), frequently mixed with Lipiodol (ethiodized oil) to increase exposure of the tumor to the drug, followed by embolization of the feeding vessel(s) with agents such as gelatin sponge <sup>41</sup>. This causes cytotoxicity and ischemia. Randomized controlled trials have shown that TACE increases survival time <sup>42–44</sup>.

The best candidate for TACE are asymptomatic patients with a solitary or limited multifocal HCC without vascular invasion or extrahepatic spread and with well-preserved liver function (Child-Pugh class A) <sup>45–47</sup>.

Favorable outcomes achieved beyond c-TACE, even TACE with drug-eluting beads (DEB-TACE), which slowly release chemotherapy after embolization <sup>48</sup> to increase tumor exposure to chemotherapy and reduce systemic drug exposure. Survival after DEB-TACE is not different from that after c-TACE but the treatment is more reproducible and better tolerated.

It is important to remember that the efficacy of TACE depends on complete obstruction of the tumor vasculature <sup>41</sup>. One important decision is when to stop TACE. TACE should not be repeated when 1) substantial necrosis is not achieved after 2 initial rounds of TACE, 2) follow-up treatment fails to induce significant necrosis at sites at risk, 3) when major progression (substantial liver involvement, vascular invasion, or extrahepatic spread) occurs after an initial response, and when re-treatment is unsafe because of deterioration of liver function.

### *BCLC Stage C*

Conventional chemotherapy, administered intravenously or intra-arterially, is ineffective for patients with HCC <sup>45–47</sup>. Sorafenib is an inhibitor of many kinases that reduces tumor cell proliferation and angiogenesis and increases tumor apoptosis <sup>49</sup>. It also induces major changes in stroma cells. Sorafenib is the standard systematic therapy for HCC. It is the first treatment option for patients with HCC of BCLC stage C <sup>45–47</sup> and for patients with BCLC stages A or B who are not candidates for curative or loco-regional treatments due to treatment stage migration and/or untreatable progression because of burden <sup>35,50,51</sup>.

The most frequent adverse events from sorafenib are hand/food/skin reaction, asthenia, diarrhea, and arterial hypertension (higher in Asian patients, but adverse events correlate with a better outcome <sup>52</sup>. Careful management and appropriate dose adjustment are therefore needed.

Time to progression may be vague because progression at imaging may not represent treatment failure. Differences in time to progression have not always translated in improved survival. This may reflect the existence of a heterogeneous progression pattern (Figure 19) and/ or potential drug toxicity that compensate the activity of the drug <sup>20</sup>.

Another new emerging therapeutic option for patients with HCC of BCLC stage C is radio-embolization by Yttrium-90, consisted in intra-arterial embolization by resin beads filled with the radioactive isotope yttrium-90.

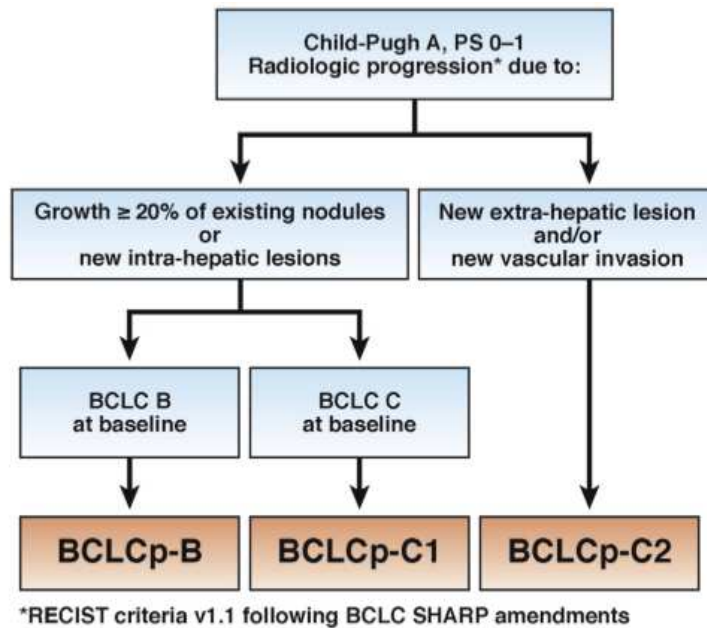


**Figure 19** : Prognosis of patients with HCC based on imaging findings <sup>50</sup>.

### *BCLC Stage D*

Patients with HCC of BCLC stage D have no treatment options, either because of their extensive tumor or advanced liver disease. Their prognosis is poor, and they should receive the best supportive care <sup>53</sup>.

## II.3 PERFUSION IMAGING

### II.3.1 PERFUSION

#### ***What is perfusion?***

Perfusion refers to the blood flow (ml/min) through the capillary circulation of a certain volume of an organ or tissue.(ml of blood/min/ 100ml of tissue) <sup>54</sup>.

Perfusion imaging provides the ability to detect regional and global alterations in organ blood flow. Specially, dynamic contrast- enhanced (DCE) magnetic resonance (MR) imaging assess blood flow at the tissue level as tissue microcirculation. This measurement is beyond the resolution of clinical MR imaging for direct visualization since capillaries are very small to be detected with MRI.

#### ***Microcirculation Characteristics***

The microcirculation is the circulation of the blood in the smallest blood vessels, the microvessels of the microvasculature system within organ tissues. The microvessels include terminal arterioles, metarterioles, capillaries and venules. Arterioles carry oxygenated blood to the capillaries, and blood flows out of the capillaries into the venules into the veins (Figure 20). The circulation in the microvasculature is very slow, in contrast with the blood circulation in the large vessels (arteries and veins) that is at high speed. That slow blood circulation permits exchanges of oxygen, other nutrients, catabolites, and wastes between the blood and tissues. Microcirculation is the most basic structural and functional unit in the circulatory system.

The main functions of the microcirculation are the supply of oxygen and nutrients, the removal of carbon dioxide (CO<sub>2</sub>), the regulation of blood flow and tissue perfusion, the inflammation responses including edema, and finally the regulation of the human body temperature.

Under normal circumstances, microcirculation of micro-vascular and blood flow is adapted to metabolism of body tissues and organs, then physiological function of various organs in human body is able to normally operate.

The microcirculatory network consists of vessels with a diameter of less than 200µm. Capillaries are about 5-8 µm in diameter, whereas red blood cells have a mean diameter of 7µm. Red blood cells circulate in single file through the capillaries and be sometimes deformed in order to pass through smaller capillaries. An adult has about 100.000m<sup>2</sup> total surface of capillary wall over which exchanges take place. <sup>55</sup>

The microvessels' wall consists of a single layer of flattened cells or endothelial cells, forming the endothelium. This wall may be surrounded by a few contractile smooth muscle cells called pericytes. Exchange of elements contained in the blood and the extravascular (interstitial) space of tissues are governed by the endothelium. The smooth muscle cells can contract, reducing the diameter of the arterioles and capillaries in order to regulate the blood flow in this microcirculatory network.<sup>55</sup>

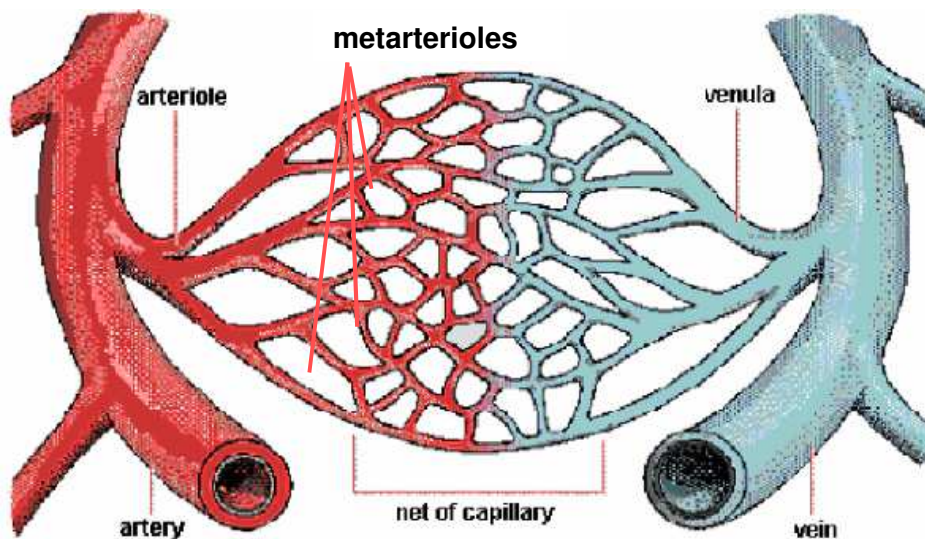


**Figure 20** : Blood microcirculation. It is the blood circulation in capillaries which in between arterioles and venules, it is the most basic structural and functional unit in the circulatory system by delivering oxygen and nutrients and removing carbon dioxide (CO<sub>2</sub>).

## ***Perfusion Parameters***

Each tissue has a specific microvascular network and its own microcirculatory system. Many pathological processes (ischemia, inflammation, cancer, diabetes, etc.) can alter the architecture and system of this network. It is therefore useful to characterize the microcirculatory network by determining its physiological parameters in order to allow diagnosis and therapeutic monitoring.<sup>55</sup>

Microcirculatory parameters are generally normalized as bulk blood flow rate divided by a given volume of tissue (ml/min/tissue volume) so that different tissues can be compared. In cross-sectional imaging (MRI, CT, PET, etc.) a voxel represents one volume element of tissue, so the parameters of the microcirculation (Figure 21) are expressed per unit of volume (per 100ml of tissue).

The simplest model of regional circulation contains a single arterial input, a tissue capillary bed, and a single venous output (Figure 21). This model has a long history originally used by Fick in the 19<sup>th</sup> Century to study cardiac output. Later modifications for indicator dilution blood flow

measurements were made by Kety and Schmidt in the 1940s and extended by Meier and Zierler in the 1950s.

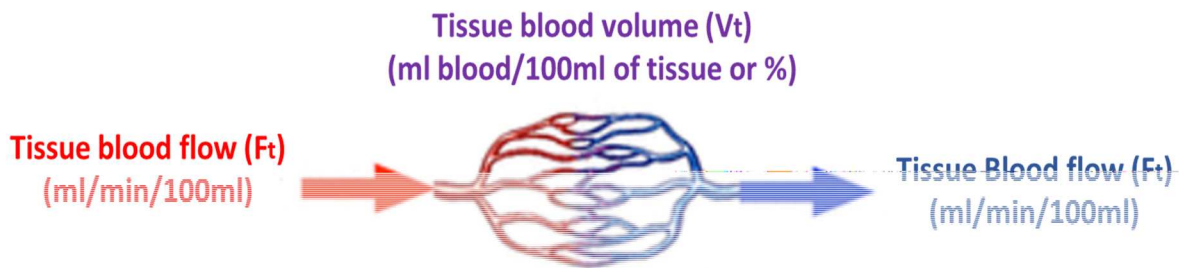


**Figure 21** : Simple model of blood circulation with a single arterial input and single bolus venous output. Loss of blood is not allowed, so tissue blood flow ( $F_t$ ) and tissue blood volume ( $v_t$ ) are assumed constant.

### *Tissue Blood flow ( $F_t$ )*

The tissue blood flow ( $F_t$ ) corresponds to the blood flow that enters (and exits) a volume of tissue (expressed in ml blood / min / 100ml tissue).

### *Tissue Blood volume ( $v_t$ ) or blood volume fraction ( $v_b$ )*

The tissue blood volume ( $v_t$ ) or blood volume fraction ( $v_b$ ) corresponds to the volume of capillary blood contained in a certain volume of tissue (expressed in ml of blood / 100ml of tissue or in %).

### *Mean Transit Time (MTT)*

Some paths through the tissue may be relatively straight while others may be highly sinusoidal with each capillary has a specific length. This means that each red blood cell takes a different amount of time to pass through the capillary bed.

Hence, the mean transit time (MTT) reflects the average time the blood to pass through the capillary network (time between the arterial inflow and venous outflow). It is expressed in sec (or min).

Tissue blood flow ( $F_t$ ), tissue blood volume ( $v_t$ ), and mean transit time (MTT) are related by the central volume theorem, so that if two are known, the third can be computed. The connecting relationship is given by the equation:

$$F_t = \frac{v_t}{MTT} \quad [1]$$

Blood flow represents a volume of blood per unit time (ml/min/100ml).

### *Extravascular and extracellular volume fraction ( $v_e$ )*

The tissue extravascular and extracellular volume fraction  $v_e$  (or tissue interstitial volume) is the volume which is contained in a volume of tissue where the extracellular contrast agents may accumulate if they cross the endothelium. It is expressed in mL of extravascular-extracellular volume / 100 mL of tissue or %.

### *Permeability-surface area product (PS)*

The permeability-surface area product (PS) is a combination of the permeability (P), which measures the transport rate of the contrast agent molecules per unit of capillary surface area, and the total surface area (S) of the capillaries. Capillary permeability is assumed to be symmetric: transport from the interstitial space to plasma is characterized by the same permeability (P). More precisely, PS is the number of contrast agent molecules travel from plasma to interstitial space per unit of time, tissue volume, and tissue plasma concentration<sup>56</sup>. It is expressed in mL/min/100mL tissue. PS depends not only on the characteristics of the capillary wall, but also on the contrast agent used.

### *Transfer constant ( $K^{trans}$ )*

Transfer constant ( $K^{trans}$ ) is defined as the rate at which the contrast agent molecules are delivered to the interstitial space per tissue volume and arterial plasma concentration. It is an important physiological parameter as it has been widely used in imaging studies to characterize tumor biology and treatment response. It is expressed in 1/min.

## II.3.2 PERFUSION MEASUREMENT METHODS IN MAGNETIC RESONANCE IMAGING (MRI)

Measurement of perfusion requires the use of contrast-agent that distribute in tissues proportionate with blood flow and can be detected. Some remain in the intravascular space, but others have a wider distribution (Figure 22).

1. **Intravascular contrast-agent** remain confined to blood vessels. MR examples include the ultra-small superparamagnetic iron oxide (USPIO) particles.
2. **Extracellular contrast-agent** do not enter cells but can pass through vessel walls to distribute in the extracellular spaces of tissues. Most gadolinium-based contrast agent are in this category. Gadolinium contrast agent has a relative small molecular size (500-1000 Da) which allows the passage through the vascular endothelium via passive diffusion into the extracellular space of most tissues. Exceptions are the brain and spinal cord, where specialized tight endothelial junctions create a blood-brain barrier (BBB) that excludes this process.
3. **Diffusible contrast-agent** distribute throughout all tissue compartments including the interior of cells.<sup>54</sup> These small molecules are usually used in nuclear medicine.

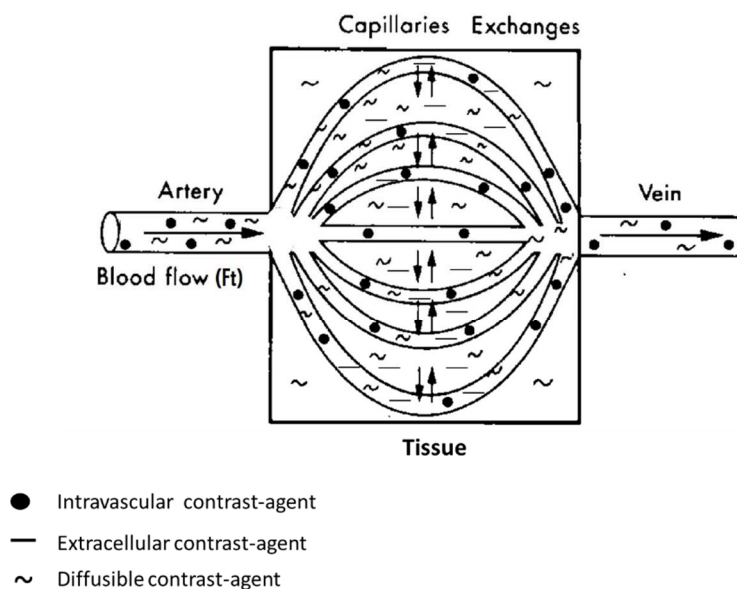


**Figure 22** : Different types of contrast-agents and their deposition in the tissue.<sup>57</sup>

Magnetic resonance techniques are powerful in visualizing tissue perfusion in the brain and other parts of body.

Three methods are commonly used to measure perfusion using MRI: Dynamic Susceptibility Contrast (DSC), Dynamic Contrast Enhanced (DCE), and Arterial Spin Labeling (ASL).

### ***Dynamic Susceptibility Contrast (DSC)***

DSC is mainly used in brain imaging for the clinical evaluation of perfusion in cerebral ischemia and brain tumors. DSC perfusion imaging begins with a bolus of gadolinium (Gd) -based contrast agent injected intravenously followed by a series of rapid acquisitions. Due to its paramagnetic properties, gadolinium (Gd) creates a local magnetic field distortion around vessels, with T2 (T2\*) dephasing and loss of signal as the bolus passes. By measuring signal intensity as a function of time through the region-of-interest analysis and fitting to a mathematical model, various perfusion parameters (e.g. cerebral blood volume (CBV), cerebral blood flow (CBF), mean transit time (MTT)) can be extracted. Because DSC technique utilizes very rapid imaging to capture the first pass of the contrast agent, it is sometimes known as bolus tracking MRI. The total image acquisition time is therefore very short (~2min).

### ***Dynamic Contrast Enhanced (DCE)***

DCE-MRI is a technique which is based on the acquisition of rapid (high temporal resolution) and serial T1-weighted images before, during, and after the intravenous administration of extracellular low-molecular-weighted MR contrast media, such as a gadolinium-based contrast agent, to measure the signal changes as a function of time. The acquisition time is approximately 5-10 minutes. DCE-MRI depicts the wash-in, peak, and wash-out contrast kinetics of the tissue, thereby providing information about the nature of tissue at the microvascular level.

DCE-MRI is sometimes referred to as “permeability” MRI as the extracellular contrast agent diffuses from the blood into the extravascular extracellular space (EES) of tissue at a rate determined by tissue perfusion ( $F_t$ ) and permeability of the capillaries their surface area (PS). The major goal of DCE-MRI is the analysis of the signal intensity of the contrast-agent over time. The image data of the DCE-MRI measurement can be analyzed visually or semi-quantitatively. Effective quantification may be obtained by applying a compartmental model allowing several physiological parameters to be derived.

### ***Arterial Spin Labeling (ASL)***

Unlike DSC and DCE perfusion MRI, ASL does not require the administration of gadolinium contrast. Instead, the patient's own water molecules serve as an endogenous diffusible tracer. This is accomplished by “magnetically labeling” water molecules in proximal blood vessels with

radiofrequency pulses. As these molecules flow into the organ of interest they reduce tissue signal intensity in proportion to perfusion. In the typical ASL pulse sequence, images are acquired both with and without labeling pulses, and then subtracted. By applying a mathematical model, various perfusion parameters (principally tissue blood flow,  $F_t$ ) can be obtained. The signal difference between the ASL signal and the static tissue signal is approximately <1% which makes the signal-to-noise ratio (SNR) relatively low. So, multiple signal averages must be acquired resulting in 3-5 min minimum acquisition time to obtain useful data. Because, SNR is limited, ASL performs significantly better at 3T than 1.5T.

**Table 1: Three Types of Perfusion MRI Techniques<sup>58</sup>**

	<b>DSC</b>	<b>DCE</b>	<b>ASL</b>
<b>Full term</b>	Dynamic susceptibility contrast	Dynamic contrast enhanced	Arterial spin labeling
<b>Bolus handling</b>	Bolus tracking	Bolus passage	Bolus tagging
<b>Acquisition point</b>	First pass of contrast agent	Accumulation of contrast agent	Accumulation of tagged blood
<b>Contrast media</b>	Intravenous bolus injection of Gd-based contrast agent	Intravenous bolus injection of Gd-based contrast agent	Without contrast agent
<b>Tracer</b>	Non-diffusible blood pool tracer	Flow or permeability-limited diffusible tracer	Diffusible tracer
<b>Relaxation mechanism</b>	$T_2/T_2^*$ relaxation	$T_1$ relaxation	Magnetic labeled blood $T_1$ relaxation
<b>Effect</b>	Increased susceptibility effect	$T_1$ shortening effect	Blood magnetization effect
<b>Signal behaviors</b>	Decreased signal	Increased signal	Subtracted signal

## II.3.3 DCE-MRI

### **Physical Principles**

The contrast agent (Gd) increases the  $R_1$  relaxation rate (decreases the  $T_1$ ) in a tissue by the relationship

$$R_1 = R_{10} + r_1 \cdot C \quad [2]$$

where,  $R_1 = \frac{1}{T_1}$  : longitudinal relaxation rate of the tissue in the presence of the contrast agent,

$R_{10} = \frac{1}{T_{10}}$  : inherent longitudinal relaxation rate of the tissue in the absence of the contrast agent,

$r_1$ : longitudinal relaxivity of the contrast agent, and

$C$ : concentration of the contrast agent in either blood or EES.

The relaxivity is dependent upon the field strength, the chemical nature of the contrast agent and the tissue.

The signal intensity ( $S$ ) from a spoiled gradient echo sequence (i.e. FLASH) is:

$$S = k[H] \cdot S_0 \cdot \left[ (1 - e^{-\frac{TR}{T_1}}) \cdot \frac{\sin(FA)}{1 - \cos(FA)} \cdot e^{-\frac{TR}{T_1}} \right] \quad [3]$$

where,  $k$ : a scaling constant,

$[H]$ : the spin density,

$FA$ : the flip angle, and

$S_0 (= e^{-\frac{TE}{T_2^*}})$  : relaxed signal ( $TR \gg T_1$ ,  $FA=90^\circ$ ).  $S_0$  can be found from the measured pre-

Gd signal (before injection of Gd).

Combining the equations [1] and [2] and provided that the three parameters  $r_1$ ,  $T_{10}$ , and  $FA$  are known then there is a clear relationship between signal and Gd concentration. Furthermore, as long as the Gd concentration decreases the  $T_1$ , there is an augmentation of the signal intensity.

### **Image Acquisition**

DCE may be performed on any organ, but it is commonly used for the heart, the breast, the liver, the prostate, and the kidney imaging. T1-weighted imaging sequence with 2D or 3D dynamic acquisition techniques are usually used, such as the 3D fast spoiled gradient echo (SPGR) or 2D gradient echo fast-low angle shot (FLASH).

The following figure (Figure 23) shows the process of DCE-MRI acquisition as well as the intensity evolution of contrast-agent (CA) in tissue before, during, and after its intravenous

administration. Especially, before the injection of contrast-agent, the intensity in both vascular space and tissue is zero. During CA administration, the intensity reaches at maximum in the vascular space while the peak intensity in tissue is appeared a few minutes later without reaching the intensity level of vascular space. After the CA administration, as long as the CA intensity reached at maximum (peak) in each enhancement curve, it is degraded. The intensity degradation of contrast-agent is a fast phenomenon in the vascular space, while being a slow phenomenon in tissue, so that their intensities to get approach in the quasi-same level a few minutes later the contrast-agent injection.

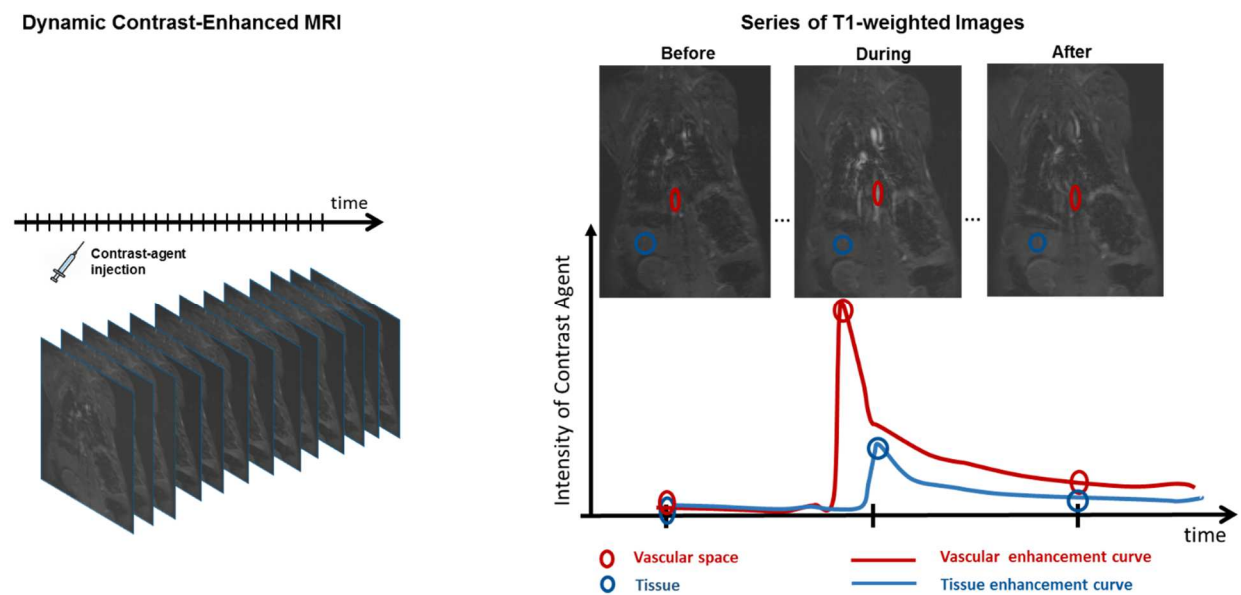


**Figure 23 :** Dynamic contrast-enhanced (DCE)-MRI acquisition. (a) Intravenous injection of contrast-agent (CA) and repeated imaging to monitor the traversal of contrast-agent within the tissue. (b) Both vascular space and tissue enhancement curves represent the intensity of contrast agent before, during, and after the CA injection at specific time points.

The DCE-MRI sequence parameters are compromised between coverage (number of slices, slice thickness), temporal resolution, and spatial resolution (field-of-view (FOV)). The optimal sequence is depended on the organ being measured. Normally, frame times of 2-20 sec can be achieved but for the measurement of the aorta curve in order to provide an arterial input function (AIF) for the modelling, a temporal resolution less than 3sec is desirable. In the liver, the parameter of temporal resolution is a drawback due to its dual supply from the hepatic artery and the portal vein, originating the respective arterial input function (AIF) and the portal input function (PIF) enhancement curves. In order to distinguish the differences of those enhancement curves within the injection peak to get the important information of the amount of contrast-agent (CA) concentration in the vascular space of tissue, it is acquired a very high temporal resolution acquisition ( $\leq 1$ sec). The current MRI does not still provide such a high temporal resolution acquisition due to the  $T_1$  limitation. Furthermore, the DCE sequence should ideally be long

enough (5-10 min) to sample the enhancement plateau. If not, then the interstitial volume ( $v_e$ ) cannot be reliably measured since is based on the plateau part of the curve. Flip angle (FA) accuracy is a crucial sequence parameter as it affects the calculation of the contrast-agent concentration from the enhancement curve (Equation 3), the estimation of the AIF, and the measurement of  $T_{10}$ . Specifically, the accuracy of the  $T_{10}$  value affects the measured values. Furthermore, a small FA gives more signal at low concentration, but has limited dynamic range (FA= 5°), increasing the FA gives increased sensitivity to Gd (FA>10°) (Figure 24), further increases give a wider dynamic range that is needed if measuring the AIF as well as the tissue enhancement.

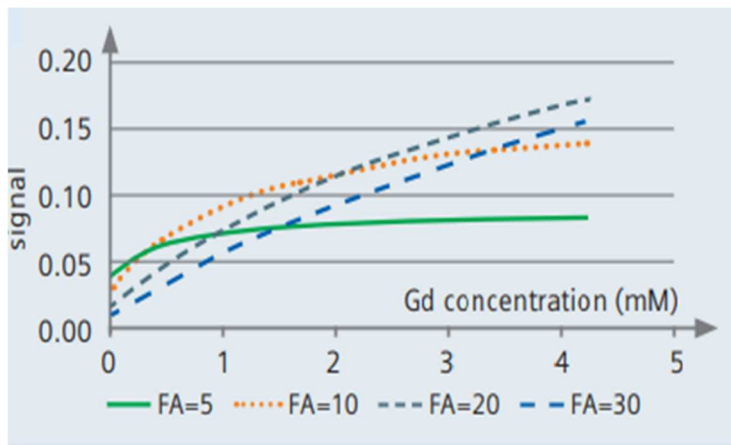


**Figure 24** : Performance of gradient echo with various FA values. TR=3ms,  $T_1=1\text{sec}$  <sup>59</sup>

For the quantitative DCE-MRI, a pre-contrast mapping of  $T_1$  is often performed. In the 3D strategy this is usually achieved by varying the FA, which runs immediately before the DCE-MRI sequence in order to obtain the  $T_{10}$  value of the tissue.

## ***Image Analysis***

After the image acquisition and extraction, the next step is the image analysis. Images may be analyzed and expressed in different methods. The most important methods are described below.

### ***Global regions of interest (ROI) analysis***

Here, large ROIs are used for the image analysis. This method is simple and has the advantage of grouping many voxels together, which provides a high signal to noise ratio (SNR) and makes the analysis of enhancement curves more robust. The main drawback, however, is that it cancels all the specific data by averaging voxels which may drive to an enhancement curve without any real physiological basis, as it is a mixture of different behaviors.

### *Voxel-by-voxel analysis (parametric mapping)*

On the contrary, voxel-by-voxel analysis is based on each individual voxel of tissue, which shows up any local heterogeneity. The disadvantage of this analysis is the fact that it is a time-consuming technique and demands great computing resources. Furthermore, if the SNR is not enough at the level of an individual voxel because of its small size, the quality of model fitting is compromised. This method is currently used in the study of the tumor heterogeneity.

### *Homogeneous voxel clusters' analysis*

This analysis is an intermediate strategy between the global ROI analysis and voxel-by-voxel analysis. In this analysis, the voxels are gathered in groups, called clusters, with either similar structural and signal characteristics before the contrast-agent injection or a similar enhancement curve after the injection. This method provides high SNR and consistent behavior, which could provide reliable information with physiological basis<sup>55</sup>

## ***Perfusion Signal Enhancement Curve***

### ***Signal Interpretation***

The behavior of the contrast-agent in tissues after the injection is determined by two different phenomena: perfusion in the microcirculatory network and leakage in the interstitial space. These two phenomena have different time courses and kinetics, but they overlap which causes a source of confusion.

### *Pure tissue perfusion*

Pure tissue perfusion corresponds on the perfusion of the molecules of the contrast agent in the microcirculatory system without interstitial leakage. During this phenomenon all molecules of the contrast agent enter into the capillary network in different time from the arterial system, and then, circulate into the capillaries. This function is very fast and can be reliably recorded if the image acquisition speed itself is very rapid (less than 3 sec per image). Then, the molecules of the contrast agent either eliminate directly via the kidney (renal filtration) or recirculate and then leakage into the kidney. The enhancement curve (Figure 25a) of this phenomenon informs us about the tissue blood perfusion ( $F_t$ ) which corresponds to the rapid rise of the curve. The peak of the curve corresponds to maximum concentration of the contrast agent when the capillaries are filled with blood (before the renal filtration) and informs us about the blood volume fraction ( $vd$ ). The recirculation is depicted on the enhancement curve as second peak (Figure 25a), which is much lower than the first peak. Furthermore, the signal decay of the enhancement curve is consisted of two parts, the first part corresponds to the direct renal filtration and the

second part to the recirculation and then to the renal filtration. Therefore, the second part of the decay signal is slower than the first one.

### *Leakage of the contrast agent into the interstitial space*

If the capillary wall is permeable to the contrast agent, it takes place the leakage of the contrast agent from the vascular space to the interstitium (interstitial space). Especially, if the concentration is higher in the plasma than the interstitium, then more contrast-agent molecules penetrate the interstitial space of tissue across the endothelial wall than contrast-agent molecules from the interstitium into plasma. The result is an accumulation of the contrast agent in the interstitial space of tissue. The accumulation rate is proportional to the difference in concentration of contrast agent across the capillary wall, the permeability ( $P$ ) of the wall to the contrast agent and the total surface area ( $S$ ) of capillary walls contained in the tissue. The rapid initial increase of the vascular enhancement curve is combined with a slower slope induced by the interstitial accumulation of contrast agent (Figure 25b).

In continue, when the concentration of contrast-agent in the plasma becomes lower than that in the interstitium, then the contrast agent is eliminated from the interstitium. The signal decrease of the tissue enhancement curve is combined with the decline part of pure enhancement curve. This part of curve gives us information about the tissue interstitial volume fraction ( $v_e$ ) (Fig.25b).

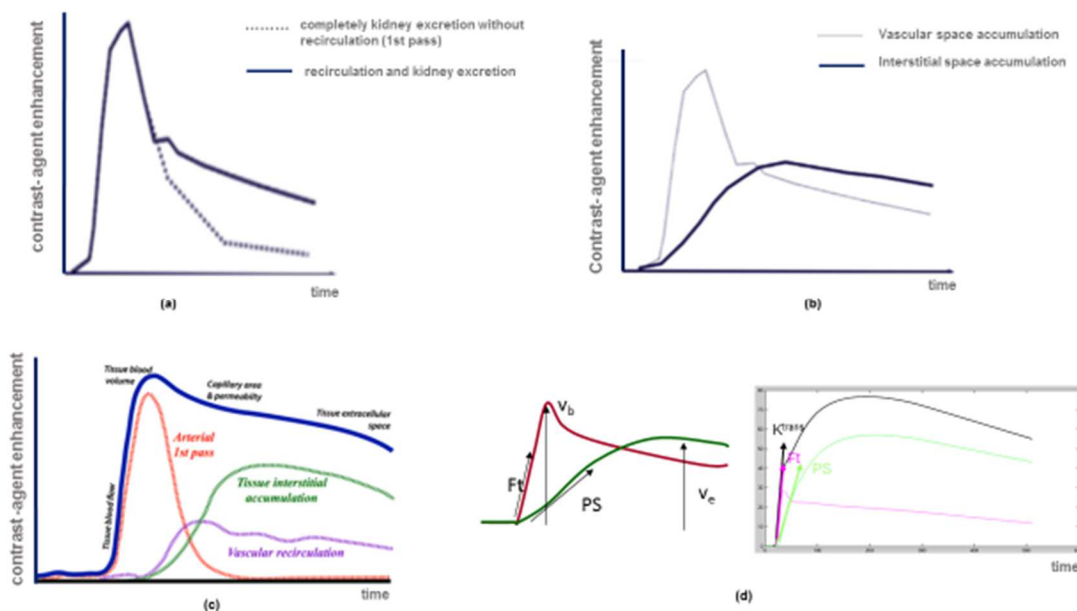


**Figure 25:** Tissue enhancement curves after bolus injection of contrast agent. (a) Tissue enhancement curve without interstitial leakage <sup>55</sup>. (b) Tissue enhancement curve with interstitium leakage <sup>55</sup>. (c) Overview of contrast agent enhancement. The tissue enhancement (solid blue line) represents the sum of the contrast-agent enhancement in the tissue vascular space (initial rapid upslope curve), plus the contrast-agent enhancement into the interstitial space (slower downslope curve). (d) Depiction of the perfusion parameters for the vascular space (red enhancement curve) and the interstitial space (green enhancement curve). The sum of the  $Ft$  and  $PS$  express the  $K^{trans}$  parameter.

## ***Signal Analysis***

The analysis of tissue enhancement curves can be performed on regions of interest (ROIs) on groups of pixels or voxel-by-voxel. DCE-data can be evaluated by one of three following methods:

### *Qualitative or visual analysis*

This method is the most widely used by clinical radiologists. It is very simple and rapid and focuses mainly on the wash-in rate, peak intensity after the wash-in phase, and the wash-out rate for multiple regions of interest can be visually assessed (Figure 26). It is effective for the characterization of certain tumors in combination with morphological criteria. However, it does not give numerical results, so it is impossible to compare different patients or measure the effectiveness of treatment in the same patient.

### *Semi-quantitative analysis*

Using this method, several semi-quantitative perfusion parameters can be obtained by analysis of DCE signal intensity curves for each voxel during passage of the contrast bolus. These parameters are easy to calculate and hence are widely used. However, they lack precision and consistency, as being highly dependent on the efficiency/ compactness of the contrast agent. The absolute values of these parameters have little meaning by themselves. But they can be useful if we use their relative values normalizing them by comparing them with those of a reference tissue such as muscle or a portion of the same tissue which is no-pathological. This normalization is performed by calculating ratios in order to obtain relative parameters. The most common of these relative parameters are the following and depicted in Figure 26:

**Arrival time (AT,  $t_0$ ):** it is the interval between the intravenous contrast agent injection and its first detection in tissue or in large artery. This interval corresponds to the baseline of the enhancement curve, as the MR signal vary randomly due to noise and motion, so several time points must be averaged before the contrast arrival in order to set a baseline.

**Time to peak (TTP):** It is the time from bolus administration to peak signal intensity.

**Area Under Curve (AUC):** It is the total area (“integral”) under the signal intensity curve during first pass of contrast agent. AUC represents the total amount of contrast agent passing through the regional vascular system and is roughly proportional to blood volume (vp). This parameter is also more robust to noise.

**Mean Time to Enhance (MTE):** It represents the average time for the entire bolus of injected contrast to pass through a region of tissue. Absolute values of MTE are highly dependent on the shape (compactness) of the arriving contrast-agent bolus and to a lesser degree on tissue

perfusion. At this point, it is important to make clear that MTE is not the same as Mean Transit Time (MTT) which corresponds to the total time for a single contrast-agent molecule (not the entire bolus) to pass through tissue.

**Percentage Maximum Enhancement or Percentage Baseline at Peak (PBP):** It is defined as the ratio of signal intensity at maximum (peak) divided by its initial values (baseline).

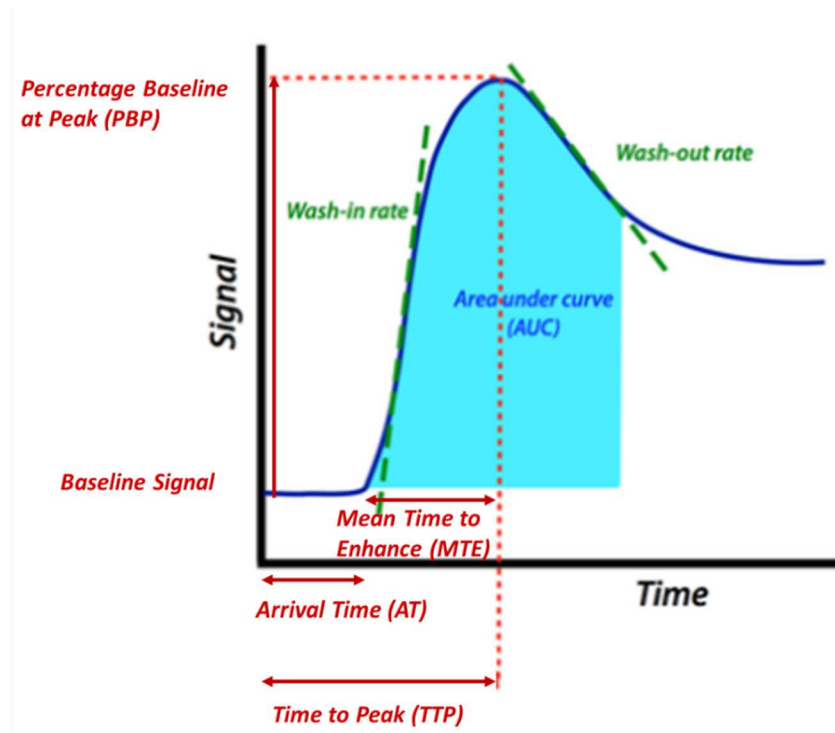


**Figure 26** : Semi-quantitative parameters' depiction.

### *Quantitative analysis*

Full quantitative analysis of the DCE data requires three steps:

1. Conversion of signal intensity to contrast-agent (gadolinium) concentration,
2. Selection of an appropriate mathematical hemodynamic model by employing the input function over time, AIF(t) for the extraction of tissue signal, C(t).
3. estimation of model parameters from the fitted data (Figure 27)

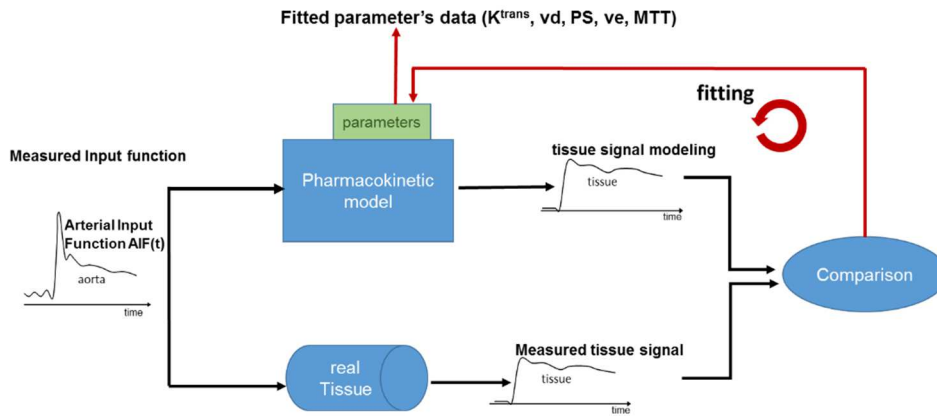


**Figure 27: Algorithm of the fitted parameters' data extraction.** Measured arterial input function (AIF) is applied to a pharmacokinetic model with a value range of perfusion parameters in order to generate tissue enhancement curves (tissue signal modeling). Additionally, the same measured input function (AIF) is applied to a real tissue extracting the measured tissue enhancement curve. Those enhancement curves (generated and measured) are compared between them and by employing the fitting technique, the fitted data of the perfusion parameters are extracted and derived from the best fit between the curves.

## II.3.4 QUANTITATIVE ANALYSIS

### ***Conversion Signal Intensity to Contrast-agent Concentrations***

The first step for full quantification of a DCE study so that being extracted more accurate and meaningful physiological information from this data is to convert signal intensity into actual contrast-agent (CA) concentrations.

The process is that the change in T1 -relaxation rate,  $dR_1(=1/dT_1)$  is linearly related to CA concentration (C). Note, however, that this assumption is true only for low -concentration solutions based to gadolinium-contrast. The relation CA concentration-signal intensity (SI) is not linear in high concentrations. Thus, by measuring the change in relaxation rates within a voxel during passage of a contrast bolus, the estimation of gadolinium concentration at time and the location can be determined.

However, in order to be obtained absolute CA concentrations, the tissue T1 without contrast-agent should be calculated. Without this calibration only relative CA concentrations can be determined from the MR signal.

Finally, because the usual contrast agents used in MRI such as gadolinium distribute in plasma rather than whole blood, their plasma should be considered through the hematocrit. The ratio of plasma to whole blood is given by the relationship:

$$C_p = \frac{C_b}{1 - Hct_b} \quad [4]$$

where,  $C_p$  : gadolinium concentration in plasma,

$C_b$  : gadolinium concentration in whole blood, and

$Hct_b$  : hematocrit in whole blood. A standard value of  $Hct_b$  is 0.45. Note that hematocrit can change even in the same patient over time, especially in cancer patients. If the Hct fluctuations do not be taken into consideration, the quality of the DCE measurement may be affected.

## ***Pharmacokinetic Models***

Once the DCE signal has been converted into gadolinium concentrations, the next step is to determine a tissue model to which the data will be fitted. There are two basic and widely used models. The first model was proposed by Paul Tofts and colleagues.<sup>56</sup> and supposes that the plasma component is small ( $v_p \approx 0$ ) so its contribution is negligible to the total tissue MR signal. The second model named two-compartment exchange model (2CXM)<sup>56</sup>. In this model, the plasma space included and both plasma space and interstitial space are considered as single compartments. This model is more complex however, it is more suitable for representing highly vascular lesions such as malignant tumors.

### *Two-compartment exchange model (2CXM)*

2CXM model consists of three components: tissue parenchyma cells (intracellular space), blood vessels (plasma), and the extracellular extravascular space (EES or interstitium) (Figure 28). Gadolinium (Gd)-based contrast-agent (low molecular weight) after the injection remains in plasma and gradually leaks, across the vascular endothelium, into the EES

1. The concentration of contrast agent **in the plasma space:**

$$v_p \frac{dC_p}{dt}(t) = F_p \cdot C_a(t) - F_p \cdot C_p(t) + PS \cdot C_e(t) - PS \cdot C_p(t)$$
$$\frac{dC_p}{dt}(t) = F_p \cdot C_a(t) - F_p \cdot \frac{C_p}{v_p}(t) + PS \cdot C_e(t) - PS \cdot \frac{C_p}{v_p}(t) \quad [5]$$

where,  $C_p$  : concentration of contrast agent in plasma

$F_p$ : plasma flow entering and exiting from plasma

$C_a$ : concentration of contrast agent in plasma from arterial blood

$C_e$ : concentration of contrast agent in the interstitium

$v_p$ : the plasma volume

$v_e$ : the interstitium volume

PS: permeability surface area product

2. The concentration of contrast agent **in the interstitial space**:

$$v_e \frac{dC_e(t)}{dt} = PS \cdot C_p(t) - PS \cdot C_e(t)$$

$$\frac{dC_e(t)}{dt} = PS \cdot C_p(t) - PS \cdot \frac{C_e(t)}{v_e} \quad [6]$$

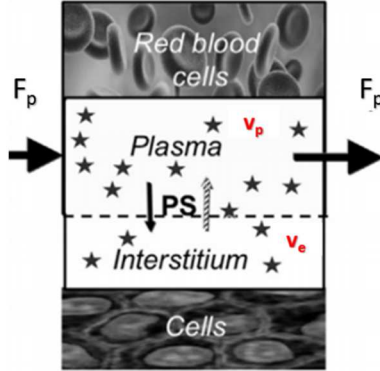


**Figure 28 :** (a) **Depiction of a 2CXM model depiction** <sup>55</sup>. Gadolinium-based contrast-agent does not enter cells.  $v_p$ =volume of plasma,  $v_e$ = volume of interstitium,  $PS$ = permeability surface area product.

*Original Tofts model*

The original Tofts and Kermode (1991) model is expressed by the following equation<sup>56</sup>:

$$v_e \frac{dC_e}{dt} = K^{trans} (C_p - C_e)$$

$$\frac{dC_t}{dt} = K^{trans} C_p - \frac{K^{trans}}{v_e} C_e$$

$$= K^{trans} C_p - k_{ep} \cdot C_e \quad [7]$$

where,  $K^{trans}$ : transfer rate of contrast agent from plasma into the EES space measured in units of  $\text{min}^{-1}$ .

$k_{ep}$ : reverse transfer rate of contrast (from the EES into plasma).

This model shows that the influx  $K^{trans} C_p(t)$  into the EES is characterized by the same rate constant  $K^{trans}$  as the outflux  $K^{trans} C_e(t)$

The original Tofts-Kermode (TK) model also assumed that intravascular contribution to total tissue gadolinium concentration was negligible. In other words, the fractional volume parameter  $v_p$  is very small and ignored in the analysis. The simple TK model (Figure 29) thus has only a single-compartment with two free parameters ( $K^{trans}$ ,  $v_e$ ) and is expressed with the integrated equation:

$$C(t) = K^{trans} \int_0^t C_p(\tau) e^{-(K^{trans}/v_e)(t-\tau)} d\tau \quad [8]$$

Using nonlinear least squares estimation on a voxel-by-voxel basis,  $K^{trans}$  and  $v_e$  can then be computed.

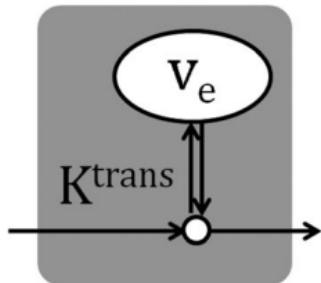


**Figure 29 : Depiction of Tofts model.** It is a weakly vascularized model. The plasma compartment has a negligible volume ( $v_p \approx 0$ ) and the interstitium is well-mixed.<sup>56</sup>

### ***Physiologic interpretations of $K^{trans}$***

When the plasma space is modelled as a single compartment,  $K^{trans}$  is defined by the formula

$$K^{trans} = \frac{F_p PS}{F_p + PS} \text{ and has different physiologic interpretations that depend on the balance}$$

between capillary permeability surface area product (PS) and plasma blood flow ( $F_p$ ) in the tissue of interest.

More specifically, there are two limiting cases:

#### ***Case 1: Permeability-Limited Model (High Flow, $F_p \gg PS$ ): extended Tofts model***

In this case, flow is high, and the blood plasma can be considered as a single pool, with equal arterial and venous concentrations. Large amount of contrast-agent is delivered to tissue, but its transport out of vascular space is slow enough. The amount of contrast-agent transferred into interstitial space is then determined by the size and the permeability of the capillary bed (permeability surface area product, PS) and the difference between the blood plasma concentration ( $C_p$ ) and the EES concentration ( $C_e$ )<sup>60</sup>. So, in this case,  $K^{trans} = PS$  if the contribution of contrast-agent in the intravascular space is ignored. The Eq. [7] is converted to:

$$\frac{dC_t}{dt} = PS \cdot \rho \cdot \left( C_p - \frac{C_e}{v_e} \right) \quad [9]$$

where,  $\rho$  is the density of tissue and expressed in gr/ml.

#### ***Case 2: Flow-Limited Model (High Permeability, $F_p \ll PS$ )***

In this case; plasma blood flow ( $F_p$ ) is much smaller than the PS product. All of the contrast-agent leaks into the EES before reaching the venous side of the capillary bed. So, after the injection of the contrast agent, the arterial concentration is low and most of the contrast agent is

being removed from the blood as it passes through the tissue. For this limited case, the  $K^{\text{trans}}=F_p$  and the one-compartment model is used. The intravascular space on the MR signal is ignored. The Eq. [7] is converted to

$$\frac{dC_t}{dt} = F_p \cdot \rho \cdot (C_p - \frac{C_e}{v_e}) \quad [10]$$

### **Mixed Flow-and PS-Limited Model (Extraction Rate, E)**

In this case, tracer uptake may be limited by both plasma blood flow ( $F_p$ ) and permeability (PS). The extraction ratio (E) indicates the fractional reduction in capillary blood concentration as it passes through tissue<sup>60</sup>:

$$E = \frac{(C_{pa} - C_{pv})}{C_{pa}} \quad [11]$$

where,  $C_{pa}$  and  $C_{pv}$  are the plasma blood concentration in arteries and in veins, respectively. As the tissue concentration gradually increases after injection, contrast-agent backflow increases, and the extraction ratio decreases. In fact,  $E(t)$  becomes negative when there is a net contrast-agent flow back into blood. The equation, in this case, is expressed as:

$$\frac{dC_t}{dt} = E \cdot F_p \cdot \rho \cdot (C_p - \frac{C_e}{v_e}) \quad [12]$$

Based on the Eq. [12], in the flow-limited case ( $PS \gg Ft$ ), the extraction ratio is complete ( $E=1$ ) and the equation reduces to Eq. [10]. In the PS limited case ( $PS \ll Ft$ ),  $E = \frac{PS}{F_p}$ , and the equation reduces to Eq.[9].

### **Arterial Input Function (AIF)**

The role of AIF is crucial in perfusion imaging. In the ideal DCE study, gadolinium is delivered to tissue in a short, compact arterial bolus. In practice, however, the initial intravenous bolus becomes delayed and dispersed by passage through the heart and the lungs. The shape of the tissue concentration curve measured in a DCE experiment is highly dependent on the shape of the arriving AIF. The quantitative analysis of the microcirculation requires the knowledge of the kinetics of the contrast agent in the afferent artery to the tissue of interest (AIF) in order to fit the correct kinetic model. Consequently, without knowledge of the AIF, valuable information about tissue kinetics may be lost. There are different methods to obtain an AIF. The most common methods are described below.

### *AIF measurement in a large artery*

Provided that the arterial blood from the heart is distributed homogeneously throughout the arterial tree, a large artery (such as the aorta or the carotid artery) can be used to obtain a proxy of the AIF for the tissue of interest. This type of AIF called *global AIF* because it is applied to all voxels within a slice. In this case, however, there is a delay between the time of passage of the bolus in the artery where the measurement of AIF is made and its arrival in the afferent arteriole of the tissue. This bolus delay is called Bolus Arrival Time (BAT) and must be considered in models using high temporal resolution. Nevertheless, this bolus delay and dispersion of contrast agent can produce significant errors in blood flow quantification.

### *AIF measurement in a small artery*

This method is potentially better for the AIF measurement compared to that in a large artery as avoiding the errors because of the bolus delay. In this method, AIF measurement arises from small arteries (*local AIFs*) located to each tissue voxel imaged. This method is used in the brain and required correction techniques for partial volume effects.

### *Population AIF*

This method is used if no vessel is available. Then, a mean AIF corresponding to an average value from a population can be used. This method is also used in the Toft's model. Although in this case, it is impossible to compare the individual results of two patients, it is however possible comparisons between two areas of tissue in the same patient, as modelling is carried out with the same AIF (normalization).<sup>55</sup>

An intermediate approach is to use a population AIF and to correct it using individual values measured in a small artery<sup>61</sup>

### *AIF in the liver*

Liver due to its dual blood supply (hepatic artery, portal vein) must consider besides AIF and PIF. PIF is the dynamic measurement on the portal vein. So, a weighted sum of both inputs (AIF, PIF) should be used to model the hepatic microcirculation and determine the respective role of these two supplies, through the Hepatic Perfusion Index (HPI).

It is easy to measure the AIF in the descending aorta or abdominal aorta, but the difficulty lies in the PIF measurement, as the portal vein is placed in the abdominal cavity which is affected by respiration movement. Consequently, it causes motion artifacts at PIF enhancement curve. Therefore, motion correction is mandatory for reliable PIF measurement.

## II.4 LIVER PERFUSION AND LIVER PERFUSION IMAGING

### II.4.1 LIVER PERFUSION

#### *Normal and cirrhotic liver perfusion*

As it was referred in the Chapter II-1, the liver is a highly vascular consisting of series of porous vascular channels (sinusoids with fenestrae) that are mainly supplied by the portal vein (75%) and supplemented by the hepatic artery (25%). The two input supplies are mixed up in the sinusoids at different time intervals to supply the liver cords. The small Space of Disse (interstitial space) separates the sinusoids from tight cords called hepatocytes. (Figure 30A). However, due to the large size of the fenestrae of the sinusoids, there is free exchange of low-molecular weight contrast agent such as gadolinium between the vascular space (sinusoids) and the interstitial space (Space of Disse) <sup>62</sup>.

In cirrhosis, a progressive disruption of normal anatomy and physiology leads to both regional and global perfusion changes. Deposition of collagen in the space of Disse causes an enlargement of Space of Disse, and alteration of sinusoidal architecture through the loss of fenestrae (capillarization) result in a significant barrier to low molecular weight contrast agent (Gd) to enter into the interstitial space (Figure 30B). As a result, portal venous flow decreases and the mean transit time (MTT) increases. This increase is caused by restriction of contrast-agent molecules' movement within the extravascular space because of collagen deposition. In cirrhosis, this alteration of portal venous blood flow is counteracted by an increase in hepatic arterial flow, a process known as the hepatic arterial buffer response.

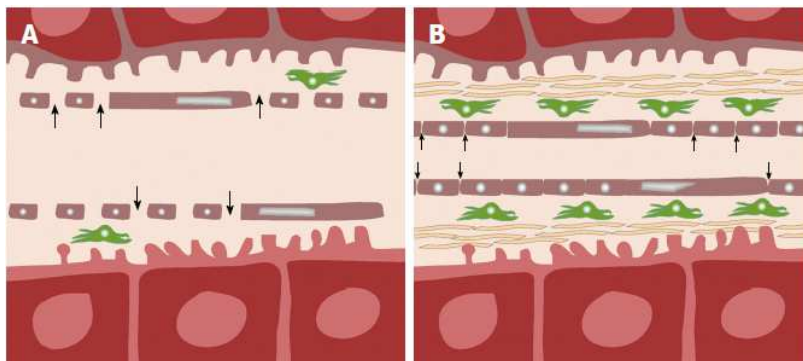


**Figure 30 :** (A) **Normal liver.** The exchange of the low molecular contrast agent (Gd) between the vascular space and interstitial space is spontaneously done through fenestrae. (B) **Cirrhotic liver.** The exchange of the contrast agent molecules between vascular and interstitial space is limited because of the fenestrae loss, which causes an enlargement of interstitial space (space of Disse). <sup>62</sup>

## ***Malignant liver perfusion***

In patients with cirrhosis, a spectrum of nodules, including benign regenerative nodules, dysplastic nodules, and Hepatocellular Carcinoma (HCC), can form<sup>63</sup>. The differences in their respective blood supplies can help in their detection and characterization. As the tumor continues to grow, there is recruitment of new vessels directly supplied by the hepatic artery (neoarteriogenesis). This is a prominent feature of HCC (primary malignancy) but can also be seen in the peri-tumoral area of liver metastases (secondary malignancy). Such an arterialization of the vascular supply is typical of malignant liver tumors.

## **II.4.2 SIGNAL ANALYSIS IN THE LIVER**

Dynamic MRI data in the liver can be processed using either a model-free or a model-based approach.

### ***Model-free approach***

Model-free approach uses semi-quantitative parameters for the analysis of the liver parenchyma and liver tumor perfusion observing the change of the rate of the signal tissue in the arterial and portal venous phases of the contrast enhancement curves.

Disease characterization occurs from the signal of the perfused liver or hepatic tumor which is enhanced with the arrival of contrast agent. Hence, most model-free approaches use parameters derived from the initial slope of the tissue signal intensity -time or contrast concentration -time curve.

One semi-quantitative description of liver and hepatic tumor vascularity is the hepatic perfusion index (HPI) which describes the relative contribution of arterial versus portal vein flow to the total liver perfusion.

### ***Hepatic Perfusion Index (HPI)***

HPI was first proposed by Miles *et al* in 1993<sup>64</sup>. HPI is expressed by the ratio of the arterial blood flow ( $F_A$ ) over the total hepatic blood flow ( $F_t$ ). The total hepatic blood flow consisted of the arterial blood flow ( $F_A$ ) and portal blood flow ( $F_P$ ).

$$HPI = \frac{F_A}{F_A + F_P} \quad \text{or} \quad HPI = \frac{F_A}{F_t} \quad [13]$$

Miles *et al* described liver perfusion imaging using CT by generating enhancement curves from regions of interest (ROIs) drawn over the liver, the aorta, and the spleen after a bolus injection of contrast agent. Liver enhancement was resolved into arterial and portal venous components

using the time to peak in the splenic enhancement curve to distinguish between the arterial and portal venous phases of the liver (Figure 31).

Liver arterial perfusion ( $F_A$ ) was estimated by the maximum slope in the liver enhancement curve before the maximum splenic enhancement divided by the peak aortic enhancement. Liver portal venous perfusion ( $F_P$ ) was correspondingly estimated by the maximum slope in the liver enhancement curve after the maximum splenic enhancement divided by the peak aortic enhancement.

This technique is simple to implement and can be applied to any segment of the liver, as there is no need to include the portal vein within the tissue imaged. However, the method underestimates portal hepatic flow for two reasons: first, the downwards slope of the last part of the arterial phase in the liver enhancement curve is superimposed on the upwards slope of the arriving portal curve, and second, the maximal slope of the portal venous phase of liver enhancement curve is divided by the peak aortic enhancement instead of the peak portal enhancement. To avoid these limitations, Blomley *et al* modified this approach.

#### *Portal venous Perfusion Index (PPI)*

Blomley *et al*<sup>65</sup> in 1995 introduced the PPI. PPI is referred to the ratio of portal venous to total liver perfusion (i.e.  $PPI=1-HPI$ ). Contributions from the hepatic artery were removed from the liver concentration-time curve by subtracting a scaled splenic concentration-time curve to give a more “accurate” portal phase in the liver enhancement curve. Using the arterially subtracted liver contrast concentration-time curve, the portal venous perfusion was estimated by dividing the maximum slope of the arterially subtracted liver enhancement curve by the peak portal enhancement.

This “corrected approach”, however, has two main limitations. First, it assumes that hepatic arterial and splenic enhancement curves are similar. Second, the technique requires a set of slices containing both the portal vein and a part of the spleen to be able to draw ROIs and extract the enhancement curves.

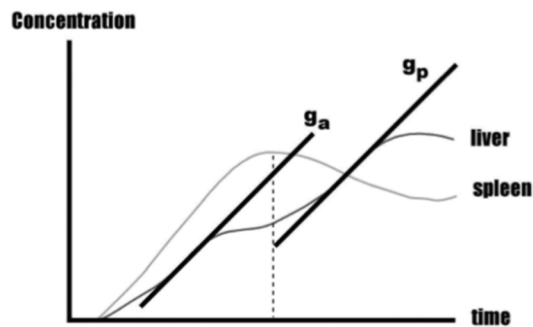


**Figure 31** : Schematic plot of the liver and spleen enhancement curves after a bolus injection of contrast agent. The diagram illustrates the biphasic enhancement of the liver consisted in arterial and portal phases.  $g_a$ = maximum slope of liver enhancement curve before peak splenic enhancement.  $g_p$ = maximum slope of liver enhancement curve after peak splenic enhancement.

### ***Model-based approach***

Model-based approach applies tracer kinetic modeling which enables quantitative vascular information to be extracted from MRI enhancement curves, when the passage of contrast agent through the liver parenchyma or tumor is observed over time.

What is measured by the MRI scanner is the average concentration of the tracer at any one time (reflected by the measured signal intensity) within the image voxel, as the vessels and the interstitial space are beyond the resolution of the MRI scanner to directly image.

Tracer kinetic modeling uses mathematical curve fitting to describe the tissue contrast concentration-time curves. If the contrast concentration-time curve of the vascular supply is known (arterial input function, AIF), subsequent mathematical techniques by convolution or deconvolution allow quantitative vascular parameters to be derived which correspond to best fitting of the tumor or tissue contrast concentration-time curves.

Several kinetic models are currently used for the assessment of liver perfusion and vary according to the physiological assumptions made. Basic categories of these kinetic models are described below.

#### ***Single-input vs dual-input***

Single-input models consider that the vascular input arises from the hepatic artery only, whereas dual-input models assume that the vascular input is derived from both the hepatic artery and the portal vein.

#### ***Single-compartment vs dual-compartment***

Single compartment models consider that the contrast agent is only confined to one compartment (i.e. vascular space), on the other hand, dual-compartment models assume that there is dynamic distribution of contrast-agent between two compartments (i.e. the vascular space and the interstitial space). Single-compartment models are computationally simpler and

could be applied as an approximation for the normal liver because the exchange of tracer between the vascular space and the interstitium spontaneously takes place because of the large fenestrae of the sinusoids. Dual-compartment models are computationally more demanding but may give a better reflection of the microcirculation of the diseased liver (tumor or cirrhosis). The illustration of these two models is depicted in Figure 32.

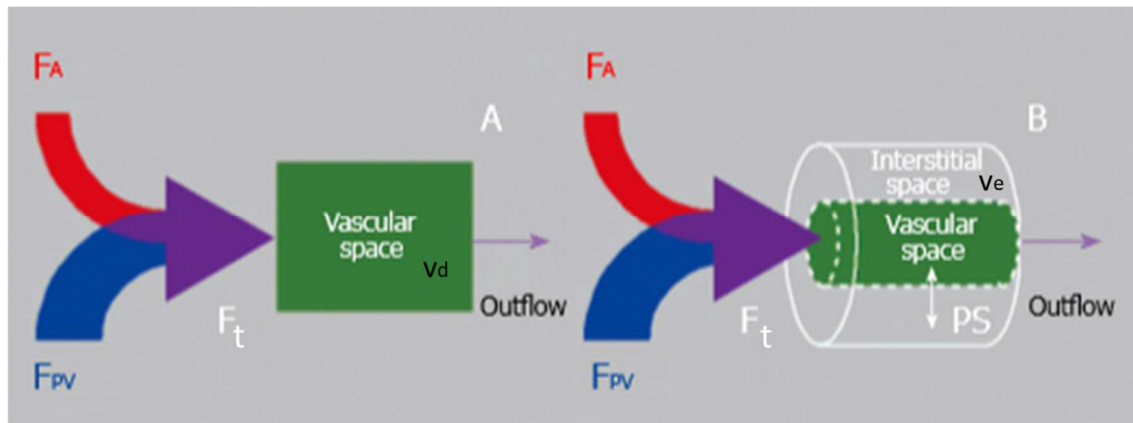


**Figure 32 :** (A) Dual-input single compartment model. Using this model, the kinetic parameters related to hepatic blood flow ( $F_t$ ) consisted of the hepatic artery ( $F_A$ ) and the portal vein ( $F_{pv}$ ) into the liver, and the distribution volume ( $v_d$ ) where the mixed hepatic blood flow distributes. (B) Dual-input two compartment conventional model. Using this model, the additional kinetic parameters that can be measured are the volume of the interstitial space ( $v_e$ ) and the permeability surface area product ( $PS$ ).

### ***Conventional compartment (CC) model vs distributed (DP) model***

Conventional compartment (CC) model is considered a model whose hypothesis is that there is instantaneous mixing or equilibrium of the contrast-agent along the entire course of a vessel. One example of a CC model is the Tofts model. The other approach is the distributed (DP) model where the concentration of the contrast-agent within the vascular space happens gradually, so the movement of CA within vascular space is not instantaneous and the measurement of CA is in the course of time. CC models are simpler to be implemented and computationally easier to be solved but make more assumptions about the microcirculation. On the other hand, DP models are more complex, so fewer assumptions about the microcirculations but are computationally more intensive and require higher temporal resolution data to derive meaningful results.

### ***Mathematical equation of compartmental models***

#### ***Dual-Input Single Compartment model***

Dual-input single-compartment model is used for the normal liver description. It can be expressed as the following equation that based on the Van Beer and Materne<sup>66</sup> model and the Tofts model:

$$\frac{dC_{Ls}}{dt}(t) = \left(\frac{F_A}{v_d}\right) \cdot C_A(t) + \left(\frac{F_P}{v_d}\right) \cdot C_P(t) - \left(\frac{F_t}{v_d}\right) \cdot C_{Ls}(t) \quad [14]$$

where,  $\frac{F_A}{v_d}$  : hepatic arterial perfusion

$\frac{F_P}{v_d}$  : portal venous perfusion

$\frac{F_t}{v_d}$  : outflow perfusion of the liver

$F_t$  : total blood flow that gets out of the liver and consisted of the hepatic artery and portal vein blood flow. For a single compartment, it is considered that the same blood amount goes into liver, the same amount goes out of it. This condition happens for the normal liver where the fenestrae of the sinusoids are large so the blood exchange between the vascular space and interstitial space happens instantaneously and is not filtered into the interstitial space of the microcirculation.

$F_A$ : hepatic arterial blood flow

$F_P$ : hepatic portal vein blood flow

$v_d$ : distributed volume of contrast agent in the liver. This volume is used instead of the hepatic blood volume, because the small-molecule contrast agent used in MRI leaks freely and instantaneously across the sinusoid capillary wall, leading to a distribution volume between the interstitial space and vascular space.

$C_A$ : concentration of contrast agent in hepatic artery

$C_P$ : concentration of contrast agent in portal vein

$C_{Ls}$ : concentration of contrast agent in the liver sinusoids

By fitting measured  $C_L(t)$ , the parameters  $v_d$ ,  $F_A$ ,  $F_P$  can be estimated and can be used to calculate hepatic arterial and portal venous perfusion, and mean transit time (MTT) of contrast agent through the liver.

This compartmental approach assumes that there is an instantaneous mixing of blood in the capillary compartment.

### *Dual-input Two-Compartment Model*

Dual-Input Two-Compartment model for the hepatic tumor description is expressed by the following equations and based on the 2CXM model:

**Vascular space:**  $v_s \frac{dC_s}{dt}(t) = F_A \cdot C_A(t) + F_P \cdot C_P(t) - F_t \cdot C_s(t) + PS \cdot C_e(t) - PS \cdot C_s(t)$

$$v_s \frac{dC_s}{dt}(t) = F_t \cdot [\alpha \cdot C_A(t) + (1 - \alpha) \cdot C_P(t)] - F_t \cdot C_s(t) + PS \cdot C_e(t) - PS \cdot C_s(t) \quad [15a]$$

**Interstitial space:**  $v_e \frac{dC_e}{dt}(t) = PS \cdot C_s(t) - PS \cdot C_e(t)$  [15b]

where,  $C_A$  : concentration of contrast agent in hepatic artery

$C_P$ : concentration of contrast agent in portal vein

$C_s$ : concentration of contrast agent in sinusoids

$C_e$ : concentration of contrast agent in the interstitium

$F_A$ : hepatic arterial blood flow

$F_P$ : hepatic portal vein blood flow

$F_t$ : total hepatic blood flow ( $F_t = F_A + F_P$ )

$\alpha$  : arterial fraction into the liver and  $\alpha = \frac{F_A}{F_t}$

$PS$ : permeability-surface area product

$v_p$ : fractional sinusoids volume

$v_e$  : fractional interstitial volume

**Table 2:** Perfusion parameters that can be extracted by using single-compartment or two-compartment model.

Parameters	Abbreviation	Definition	Unit	Model	Remarks
Mean Transit Time	MTT	Mean time taken by blood to flow through the microcirculation of tissue	seconds or minutes	Single-compartment	$v_d/F_T$
Liver distribution volume	$v_d$	Percentage of tissue volume in which the contrast agent distributes itself	% or ml/100ml of tissue	Single-compartment	
Tissue hepatic perfusion	$F_T$	The blood flow from the hepatic artery and the portal vein in a given volume of tissue. $F_T = F_A + F_P$	ml/min/100ml of tissue	Single- and Two-compartment	Flow-limited $K^{trans}$ case
Tissue arterial perfusion	$F_A$	Blood flow from the hepatic artery in a given volume of tissue	ml/min/100ml of tissue	Single- and Two-compartment	$\alpha F_T$
Tissue portal vein perfusion	$F_P$	Blood flow from the portal vein in a given volume of tissue	ml/min/100ml of tissue	Single- and Two-compartment	$(1-\alpha)F_T$
Hepatic Perfusion Index	HPI or $\alpha$	Percentage of the hepatic arterial perfusion in the tissue. $HPI = F_A / (F_A + F_P)$	%	Single- and Two-compartment	
Bolus Arrival Time	BAT or $t_0$	The time interval of the blood to move from the ROI in the vascular space to the ROI in the tissue space	seconds or minutes	Single- and Two-compartment	
Vascular transit time	$t_1$	The mean time the blood to traverse the vascular space	seconds or minutes	Two-compartment	
Permeability Surface Area Product	PS	The hepatic blood flow through the capillary wall in a given volume of tissue	ml/min/100ml of tissue	Two-compartment	Permeability-limited $K^{trans}$ case
Fractional vascular volume	$v_p$	The volume fraction in the vascular space	%	Two-compartment	$F_T t_1$
Fractional extravascular extracellular volume	$v_e$	The volume fraction in the interstitial space	%	Two-compartment	
Extraction ratio	E	The organ's relative efficiency in eliminating the contrast agent from the systematic circulation over a single pass through the organ	dimensionless	Two-compartment	$1 - \exp(-PS/F_T)$

## Theory of the convolution & deconvolution methods

### Convolution

When the contrast agent enters the tissue, the “normalized” tissue signal (measured tissue response  $C_t(t)$ ) results from a linear and stationary process over time derived from the arterial input function signal, AIF(t). AIF corresponds to the contrast agent (CA) concentration input that comes from the artery and results into tissue. However, the AIF(t) will not appear all at once at the venous exit, rather as a delayed and spread version of the input which is defined by  $h(t)$  and called **impulse outflow response**. Hence, the concentration-time curve at the venous outflow,  $C_0(t)$ , is the convolution of AIF(t) by  $h(t)$

$$C_0(t) = AIF(t) * h(t)$$

[16]

where \* denotes the convolution process.

If all contrast agent leaves the system, the area under h(t) should be unity (i.e. 100%). The integral of h(t) is:

$$H(t) = \int h(t) dt \quad [17]$$

where H(t) is the fraction of an impulsive input which has already left the tissue by time t. It is called **cumulative frequency function**.

### *Residue function*

However, since we cannot measure the concentration-time at the venous outflow of the tissue (such as the dual supply of the liver) and can only measure the concentration-time curve of contrast agent into the tissue, the venous outflow concentration is derived by the tissue concentration-time curve. This measurement can be accomplished by using the concept of residue function. The **residue function** is the complementary function of H(t) (Figure 33):

$$R(t) = 1 - H(t) \quad [18]$$

R(t) represents the fraction of the impulsive input of the contrast agent that remains within the tissue, its distribution volume,  $v_d$ , at time t.

The concentration-time curve of the remaining contrast agent in the distribution volume within the tissue,  $C_d(t)$  is expressed by the convolution of AIF(t) by R(t):

$$C_d(t) = AIF(t) * R(t) \quad [19]$$

However, the  $v_d$  of the contrast agent is within a larger volume of tissue,  $v_t$ . Therefore, the concentration of contrast agent within the tissue is:

$$C_t(t) = C_{dt}(t) \cdot V_{dt} \quad [20]$$

where,  $v_{dt} = \frac{v_d}{v_t}$  is the fractional dilution volume of the contrast agent expressed as a percentage

of the total volume of tissue  $v_t$ . If we want to measure the concentration of contrast agent in a voxel of tissue,  $C_t(t)$ , we convolute the input function, AIF(t) by **the tissue transfer function**,

**$R_t(t)$**  [ $R_t(t) = v_{dt} \cdot R(t)$ , where  $v_{dt} = \frac{v_d}{v_t}$ ]:

$$C_t(t) = \int_0^t AIF(t - \tau) \cdot R_t(\tau) d\tau = AIF(t) * R_t(t) \quad [21]$$

where the subtraction (t- $\tau$ ) corresponds to the time interval between the time point where the CA is in the artery up to the time point into tissue.

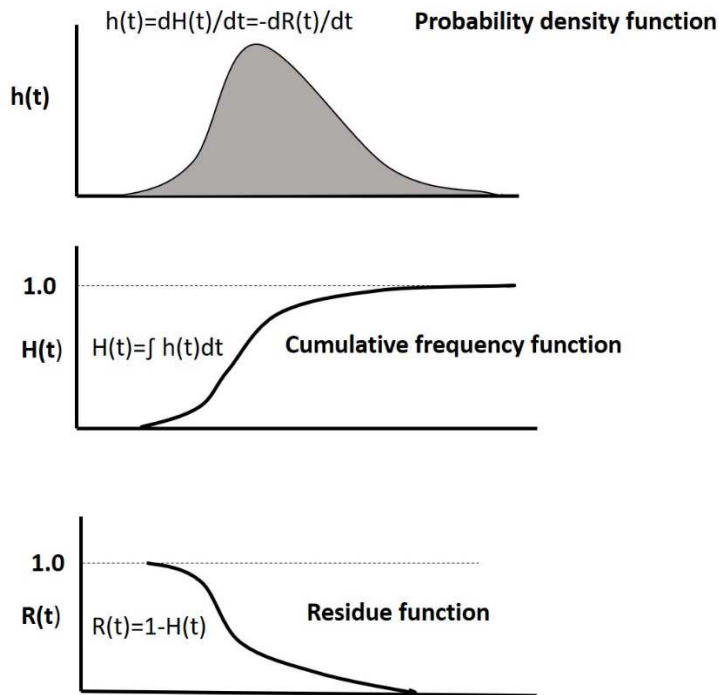


**Figure 33** : Relations between the residue function  $R(t)$ , the cumulative frequency function  $H(t)$ , and the probability density function  $h(t)$ . Both the initial value of  $R(0)$  and the final value of  $H(\infty)$  are normalized to one (1), and their combination corresponds to the area under the curve  $h(t)$ .

### Deconvolution

Deconvolution allows the determination of the theoretical impulse response  $R_t(t)$  of the tissue that can be computed from both the CA concentration-time input curve of contrast agent, AIF(t) and the concentration-time curve of contrast in the tissue,  $C_t(t)$ , based on the Eq.[21]. Hence, after contrast agent injection, a deconvolution process can compute the  $R_t(t)$  knowing the contrast variation of the tissue  $C_t(t)$  and the AIF(t).

### Extraction of the perfusion parameters using the impulse response

#### Mean Transit Time (MTT)

The MTT is the ratio of the blood volume of the tissue to the blood flow through the tissue. So, it can be calculated, through the vascular space, as the maximal value (geometric mean) of the calculated  $C_o(t)$ :

$$MTT = \frac{\int_0^{\infty} t C_o(t) dt}{\int_0^{\infty} C_o(t) dt} \quad [22]$$

It can also be calculated from the impulse response by dividing the area beneath the curve of contrast concentration as a function of time by its initial (maximum) value:

$$MTT = \frac{\int_0^{\infty} th(t)dt}{\int_0^{\infty} h(t)dt} \quad [23a]$$

However, knowing that  $\int_0^{\infty} h(t)dt = 1$  then  $MTT = \int_0^{\infty} th(t)dt$  [23b]

### Fractional volume of distribution (vd)

It can be calculated by the equation  $R_t(t) = v_{dt} \cdot R(t)$  applying the initial (maximal) value of  $R_t(t)$ ,  $R_t(0)$ . Knowing that  $R(0)=1$  then initial equation is converted to:

$$v_{dt} = R_t(0) \quad [24]$$

### Tissue blood flow ( $F_t$ )

It can be calculated by the central volume theorem:

$$F_t = \frac{v_{dt}}{MTT} \quad [25]$$

It is expressed as ml/min/ volume of tissue, usually ml/min/100ml.

### Deconvolution with two Inputs

Liver, as it is known, is composed of two supplies (hepatic artery and portal vein). For the deconvolution to be feasible in cases with multiple inflows, all inflows must meet and mix at the input to the system. This condition is fulfilled in the liver, as arterial and portal blood are mixed in the sinusoidal capillaries. Thus, the tissue concentration-time curve in the liver can be expressed as:

$$C_t(t) = [\alpha C_A(t) + (1 - \alpha) C_P(t)] * R_t(t) \quad [26]$$

where,  $\alpha = \text{HPI}$

$C_A(t)$  is the hepatic arterial CA concentration over time

$C_P(t)$  is the portal venous CA concentration over time

So, if the  $C_A(t)$  and  $C_P(t)$  are measurable, the deconvolution process allows the calculation of impulse response  $R_t(t)$ .

# III. OPTIMIZING THE BOLUS SCHEME FOR LIVER DCE-MRI: THE FOUR BOLUSES STRATEGY

---

## III.1 OPTIMIZATION OF THE ACQUISITION PROTOCOL

### III.1.1 RABBIT HANDLING

#### *Rational to perform our study in rabbits*

Rabbits are one of the most commonly used animals in research. They are widely used for experimentation and testing mainly due to practical, rather than scientific considerations. They are small and usually docile, easily restrained, cheap to maintain and breed in big amounts. Rabbits are also used in biomedical research, as models for diseases and disorders of the eyes, skin, heart and immune system <sup>67</sup>.

The MRI experiments of my project were based on rabbits to image the liver and tumor microcirculation. For the liver microcirculation imaging the positioning of a region of interest (ROI) into the portal vein is necessary to measure de portal input function (PIF). Because the size of the portal vein is very small in rats and mice, the accurate measurement of the PIF is not accessible, therefore the use of bigger animals is required. The rabbit represents a good alternative, when remaining small enough to fit into our MRI scanner, which is dedicated to small animal, employing a dedicated “rabbit gradient coil”.

## ***Rabbit handling before and during the MRI protocols***

### *Anesthesia protocol*

The procedure of the anesthesia protocol in rabbits in an MRI experiment breaks up into two parts; the premedication anesthesia (sedation) and the anesthesia for maintenance (during the MRI protocols).

During the sedation part (15 minutes before the MRI experiment), the rabbits were being anesthetized with a solution of Ketamine (Imalgene; 50mg/kg) dose at 0.6ml/kg and Xylazine (Rompun; 5mg/kg) dose at 0.4ml/kg delivered intramuscularly.

During the MRI experiment, the rabbit anesthesia was being maintained by mechanical ventilation via an alternative endotracheal mask (v-gel, Docsinnovent) (Figure 34) with a mixture of air, O<sub>2</sub> and, isoflurane at 45%, 55%, and 0.5%-2.0%, respectively.



**Figure 34** : (a) Anesthesia maintenance in rabbits during the MRI experiment with Isoflurane through the v-gel endotracheal mask. (b) Endotracheal v-gel mask.

### *Difficulties about the rabbit handling and Anesthesia Side effects*

However, throughout my MRI experiments, I encountered several difficulties in relation to the rabbit manipulation based on the anesthesia. Although rabbits are often used in research, they are fragile animals. They get scared when they are picked up. Their bones are delicate, and they can get hurt and even break their own backs when kicking to get away. Consequently, at the beginning many rabbits died before or at the very start of the experiments (Table 3). Therefore, the first year of my experiment, due to my limited experience on rabbit care, I employed a vet examination bag (BUSTER) (Figure 34) to handle the rabbit during the pre-medication anesthesia. This bag restrained the rabbit in a gentle way during the anesthesia injection. It resulted in less stress on my end and consequently less stress to the rabbit.



**Figure 35** : Vet examination bag used to handle the rabbits during the pre-medication anesthesia injection to keep the rabbit restrained in a gentle way.

Furthermore, rabbits are often considered as difficult animals in relation to anesthesia. This is related to the fact that the doses needed to induce and maintain anesthesia and those producing toxic effects are close. A large variety of secondary effects are related to stress and result to fatal cardiac or respiratory reactions <sup>68</sup>.

**Table 3:** List of rabbit deaths before and during the MRI experiments.

CAUSE OF DEATH	NUMBER OF RABBITS
Stress because of pre-medication anesthesia	6
High dose of isofluran gas or wrong position of the supraglottic mask for the anesthesia	6
Unclear cause	2
<b>TOTAL DEATHS</b>	<b>14</b>

### *Rabbit Respiration rate fluctuation*

The physiological range of the respiratory rate values in rabbits is between 32 and 60 Breath/min.

Within the MRI scanner, the respiration rate was continuously recorded using an air-pad placed under the rabbit abdomen in order to monitor the depth of the anesthesia.

During the MRI acquisitions, the respiratory rate was usually increasing beyond the upper extent of the physiological range, especially after the first injection of contrast agent.

Therefore, during the MRI experiment, I had to be aware in order to adjust the isoflurane rate according to the rabbit respiration rate so that it keeps within the physiological range but avoiding the rabbit to wake up and move.

### ***Rabbit handling Post-MRI***

At the end of the experiment, the rabbits had to be kept warm and quiet. So, I was placing a bottle with a warm water underneath their belly and blanketing them with a laboratory absorbing paper.

## **III.1.2 MRI PROTOCOLS**

The current imaging laboratory at the PARCC (U970), where I performed all the MRI experiments, had a large experience on the rats and mice imaging, but limited experience on the rabbit. So, I had to develop liver protocols from scratch with the help of the MRI responsible Gwennh el Autret dedicated to rabbits.

Because the rabbits are bigger than the rodents (rats and mice) usually imaged in the MRI scanner, we had to switch the gradient coil to a dedicated rabbit gradient coil. This procedure was difficult and long because the gradient coil was very heavy (40 kg) and needed to fit perfectly into the MRI bore. A dedicated fulcrum was necessary for the procedure. Therefore, the MRI sessions were programmed at special timing and required to perform the costly change of gradients before and after each session.

### ***Anatomical-Morphological Sequences***

MRI protocol of our study was consisted of two types of sequences; anatomical-morphological and dynamic sequences. The anatomical (T1-weighted) and morphological (T2-weighted) sequences detected the aorta, portal vein, liver, and tumor. The right detection of these tissues was a crucial point of the MRI experiment. Slices of the dynamic sequence (DCE) were placed over these tissues to acquire the respective regions of interest (ROIs) that determined their enhancement curves such as Arterial Input Function (AIF), Portal Input Function (PIF), liver, and tumor enhancement curves. Analyzing, then, those enhancement curves by using the deconvolution technique we could extract the perfusion parameters of the liver.

The final experimental MRI protocol is presented in Table 4.

**Table 4:** The sequences of my MRI protocol for the liver study.

	<b>T<sub>1</sub> -weighted</b>	<b>T<sub>2</sub> -weighted</b>	<b>DCE</b>
<b>Sequence Type / Slice Orientation</b>	<b>RARE (2D) / Coronal</b>	<b>TurboRARE (2D) / axial</b>	<b>FLASH (2D) / coronal</b>
<b>Flip Angle (°)</b>	90	90	70
<b>TR / TE (ms/ms)</b>	975.9 / 12.6	3420 / 50.1	23.9 / 2.9
<b>Thickness (mm)</b>	3	2	3
<b>Slices Number</b>	15	21	3
<b>Temporal Resolution</b>	-	-	2sec 37ms
<b>Repetitions</b>	1	1	253
<b>Total Time</b>	4min 49sec	5min 28sec	10min

### ***Dynamic sequence***

Dynamic contrast-enhanced (DCE) technique performs high temporal resolution sequences to monitor the traversal of the contrast-agent into the body. In DCE-MRI, the most common sequence called Fast Low-Angle Shot, FLASH (T<sub>1</sub>-weighted images) and the usually applied dynamic injection protocol is the single-bolus injection protocol.

In our study, we also employed the FLASH sequence. However, in terms of the injection protocol, we applied a new injection strategy (four-bolus injections) that allowed us to study efficiently the liver perfusion avoiding the signal saturation and improving the transient pattern separation between the AIF and PIF.

### ***Justification the bolus injection protocol (optimization of the number of injection)***

Using an iterative process, we set up our final “four bolus injection protocol” by optimizing the number of boluses their dilution, their volume, total acquisition time as well as the process of injection.

First, we performed a single-bolus injection protocol with contrast-agent dose of 5ml with concentration dilution at 1/5. Image analysis however, appeared signal saturation at AIF peak as the late part of the curve took place before the complete shape of the AIF transient pattern. In addition, the difference between the AIF’s and PIF’s signals was slight that does not fit the theory. Moreover, the wash-out part of both AIF and PIF curves was noisy and insufficient (Figure 36).

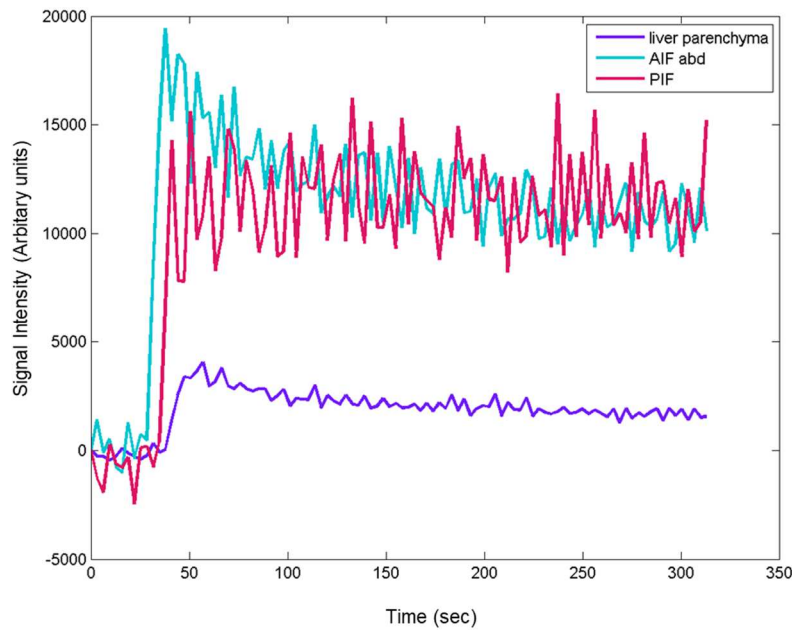


**Figure 36 :** Single-bolus protocol with 5ml of Gd-DOTA and a concentration dilution at 1/5. Signal saturation at the AIF curve.

Therefore, we moved on to a dual-bolus injection protocol with the same bolus volume but higher dilution (1/10). We tried out two different dual-bolus injection protocols (see Table 5). The first protocol occurred saturation effects at 2<sup>nd</sup> bolus because of the administration of pure contrast-agent. Regarding the second protocol, the interval time (1min) between two bolus injections, was deficient to be obtained an adequate first-bolus wash-out part. Furthermore, the concentration dilution at 1/10 was not enough to avoid the saturation effects. Thus, we passed to a third double-bolus protocol increasing the dilution at 1/15 and the interval time at 2min.

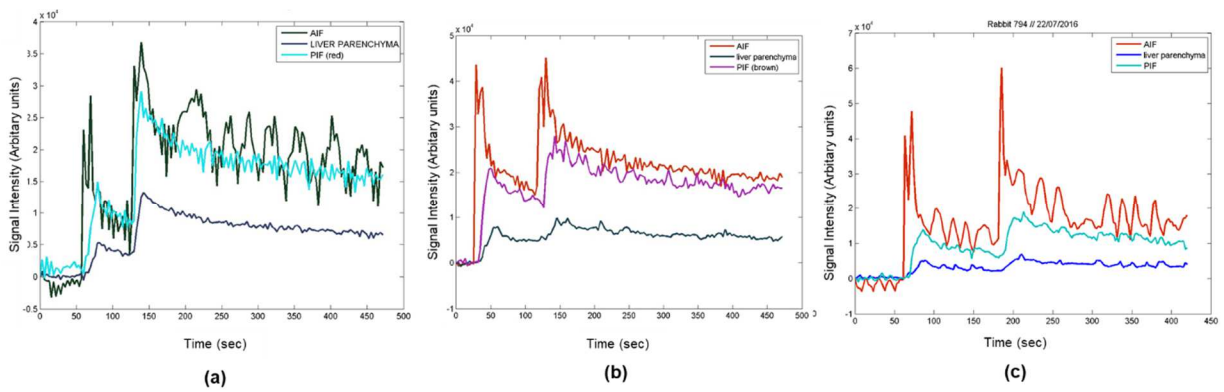


**Figure 37 :** Three different dual-bolus injection protocols. (a) 1st bolus: 3ml Gd-DOTA (1/10 dilution), 2nd bolus: 1ml Gd-DOTA (pure), and time interval between boluses: 1min. (b) 1st bolus: 5ml Gd-DOTA (1/10 dilution), 2nd bolus: 5ml Gd-DOTA (1/10 dilution), and time interval between boluses: 1min 30 sec. (c) 1st bolus: 5ml Gd-DOTA (1/15 dilution), 2nd bolus: 5ml Gd-DOTA (1/15 dilution), and time interval between boluses: 2min. The (c) protocol is better than the other two because it has less saturation effects and efficient wash-out part of first bolus.

The results of the last double-bolus protocol were better than the other two protocols because the saturation effects had been decreased and the wash-out part of the first bolus was efficient.

However, the goal of our study was to yield the best ratio between the supplies of AIF and PIF that is provided by Hepatic Perfusion Index [ $HPI=AIF/(AIF+PIF)$ ]. HPI is a crucial parameter in the liver study as it furnishes information about the amount of the arterial blood enters the liver. Thus, the increase of the differences in the transient pattern of the AIF and PIF to the greatest extent may give us the sufficient information about it. To accomplish this goal, we increased the number of the bolus injections so that the signal of AIF and PIF to break up into more transient patterns that allowed the optimization of the statistical noise of the measurement within the transient pattern and consequently the emergence of the differences between AIF and PIF. Moreover, the increase of the total acquisition time from 7min to 10min helped us to study better the later effects of the microcirculation (interstitial diffusion of the contrast agent).

We firstly performed a 3-bolus injection and then a 4-bolus injection protocol so that the expected results to be superior. However, when we changed the bolus injection protocol from 3 boluses to 4boluses, we decreased the volume of each bolus (Table 5; 4 boluses) so that the signal intensity to keep within an acceptable intensity range in relation to avoiding the signal saturation. We also increased the dilution at 1/25 in order not to exceed the clinical dose (Figure 38b).

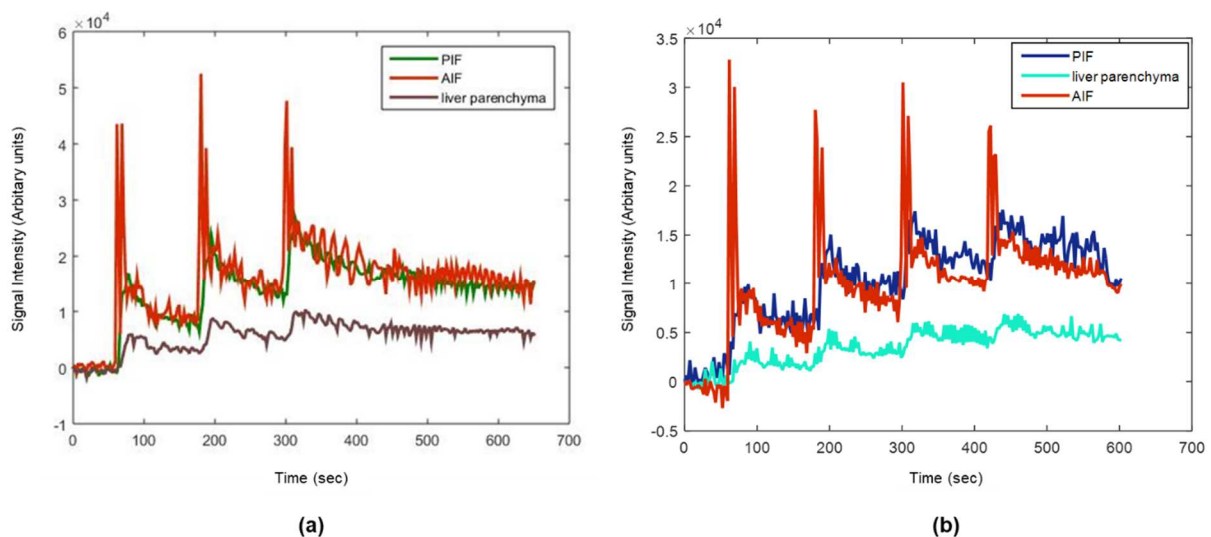


**Figure 38** : Two different bolus injection protocols. (a) 3-bolus injections' protocol; 5ml Gd-DOTA with a concentration dilution at 1/15. (b) 4-bolus injections' protocol; 4ml Gd-DOTA with a concentration dilution at 1/25.

Up to this point of my experiments, the bolus injections were manually administrated. It was often yielding double AIF peaks that degraded the sensitivity and the reliability of the measurement (Figure 38). Furthermore, the manual bolus injection did not let us know and control the injection rate to manage a sharp and standardized bolus. Thus, we decided to use a MR-compatible power injector (Optistar, Elite; Guerbet, France) in order to assure the right administration of the boluses for reliable and robust measurements. We set up the injection rate of the bolus injection to 3ml/sec. The use of an injector improved considerably the quality and reproducibility of the injection (Figure 39). In addition, it allowed me to stay out of the MRI room

during the injection, avoiding possible ear lesions and giving me the opportunity to monitor the total acquisition and the rabbit respiration rate from the console room.

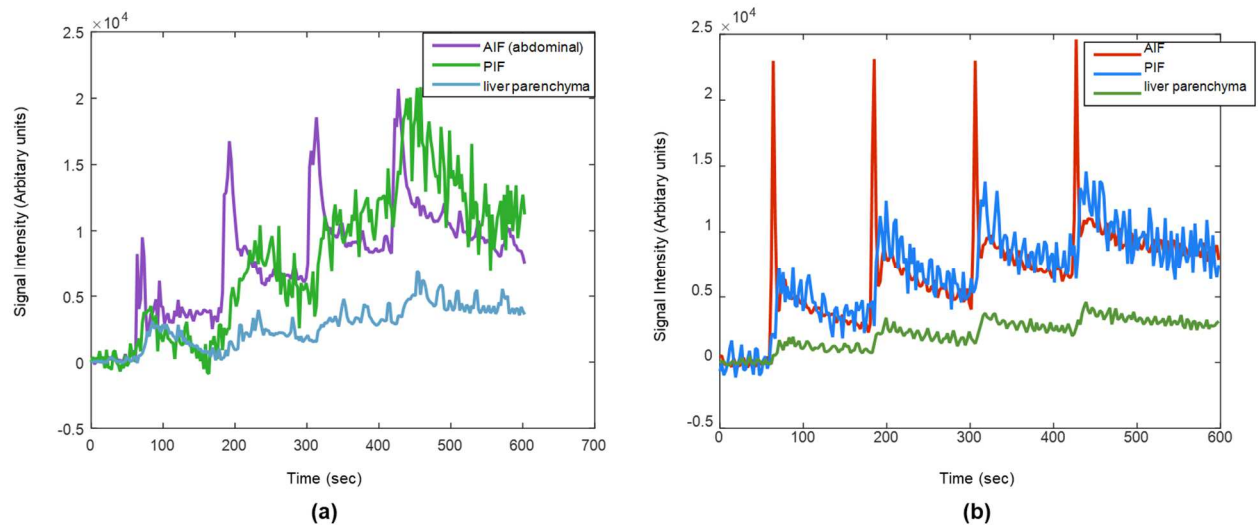


**Figure 39** : four-boluses injection protocols applied to the same rabbit (a) without the MR compatible injector (b) with the MR-compatible injector. When using the MR-compatible injector, the AIF transit pattern is sharp and identical in each bolus.

### *Justification the sequence parameters*

DCE MRI requires T1 weighted images (in order to estimate the signal enhancement induced by the increase of gadolinium chelate) with a high temporal resolution (temporal resolution of less than 5s, in order to accurately depict the transient changes in signal due to the bolus injection, especially in the small animal). Gradient echo sequences are commonly used for this purpose. They may be 2D or 3D sequences and the Fourier space may be filled in the classical in line way or more recently with dedicated filling strategies such as the spiral, radial or keyholes. In our study, FLASH sequence was used for the DCE-MRI experiments. FLASH is a fast gradient echo sequence with low flip angles (FA). Using this sequence, short repetition time (TR) (20-30ms) can be set for obtaining high T1 contrast while keeping the signal intensity in reasonable levels thanks to quasi-low FA. Additionally, the time echo (TE) should be as short as possible to suppress T2/T2\* effects. Consequently, T1 contrast depends on the short TR and low FA in combination with short TE.

Based on the Table 5, in my study, I tested three different combinations among TR, TE, and flip angle (a): a) TR= 24.73ms, TE=2.9ms,  $\alpha=90^\circ$ , b) TR= 16.47ms, TE=2.9ms,  $\alpha=90^\circ$ , and **c) TR= 24.73ms, TE=2.9ms,  $\alpha=70^\circ$**

Finally, the third combination provided the best quality imaging results. The selection of these values was based on the rationale to obtain a high T1 contrast (signal intensity) in relation to

decreasing the  $T_2/T_2^*$  effects and increasing the temporal resolution to avoid the mis-sampling of AIF and PIF data within the transient pattern.

A previous study, performed in our laboratory by Daniel Balvay, proved that the suitable flip angle to remain in the quasi-linear part of the contrast-agent concentration-signal intensity relationship and obtain a high SNR is  $FA \geq 70^\circ$  with  $TR=27\text{ms}$  and  $TE=2.24\text{ms}$ . Consequently, the final decision of the parameters' values was based on those results.

**Table 5:** Different bolus injection protocols performed within the entire interval of my thesis

	TR (ms)	TE (ms)	Flip angle (α)	Slice Number	Temporal resolution	Total Time	Dynamic Protocol
<b>1 BOLUS</b>	24.7	2.9	70°	2	3sec 16ms	5min	(30sec baseline) 5ml Gd (1/5 dilution) + 3ml saline
<b>2 BOLUSES</b>	24.7	2.9	90°	2	3sec 16ms	7min	(30 sec baseline) 1st: 5ml (1/10) Gd + 2ml saline (1.5 min interval) 2nd: 5ml Gd (1/10) + 2ml saline (1 min baseline) 1st: 3ml Gd(1/10) + 3ml saline (1 min interval) 2nd: 1ml Gd (pure) + 2ml saline
	16.47	2.9	90°	2	2sec 108ms	7min	(1 min baseline) 1st: 5ml Gd (1/15) Gd + 2ml saline (2 min interval) 2nd: 5ml Gd (1/15) + 2ml saline
<b>3 BOLUSES</b>	16.47	2.9	90°	2	2sec 108ms	10min	(1min baseline) 1st: 5ml Gd (1/15) Gd + 2ml saline (2 min interval) 2nd: 5ml Gd (1/15) + 2ml saline (2 min interval) 3rd: 5ml Gd(1/15) + 2ml saline
	24.7	2.9	70°	3	2sec 37ms	10min	(1min baseline) 1st: 5ml Gd (1/15) Gd + 2ml saline (2 min interval) 2nd: 5ml Gd (1/15) + 2ml saline (2 min interval) 3rd: 5ml Gd(1/15) + 2ml saline
<b>4 BOLUSES</b>	24.7	2.9	70°	3	2sec 37ms	10min	(1min baseline) 1st: 4ml (1/25) Gd + 1.5ml saline (2 min interval) 2nd: 4ml Gd (1/25) + 1.5ml saline (2 min interval) 3rd: 4ml Gd(1/25) + 1.5ml saline (2 min interval) 4th: 4ml Gd (1/25) + 1.5ml saline
							(1min baseline) 1st: 4ml (1/25) Gd (2 min interval) 2nd: 4ml Gd (1/25) (2 min interval) 3rd: 4ml Gd(1/25) (2 min interval) 4th: 4ml Gd (1/25)

## **III.2 COMPUTER SIMULATION TESTING OF THE FOUR BOLUSES STRATEGY (*PAPER I*)**

To test the feasibility of “four boluses strategy” regarding the robustness of the measurement of perfusion parameters, we performed a computer simulation. We present below general information and comments regarding this study. The study itself is formally presented in the paper N°1 at the end of the manuscript.

### **III.2.1 INTRODUCTION**

The aim of this study was to improve the measurement robustness of the perfusion parameters in liver DCE-MRI by enhancing the Signal to Noise Ratio (SNR) while preventing systematic error and decreasing the signal saturation

Dynamic Contrast enhanced (DCE) imaging is the most developed functional imaging technique for the evaluation of tissue microcirculation, beyond the brain. Although, DCE-imaging may be performed with different modalities such as magnetic resonance imaging (DCE-MRI), computed tomography (DCE-CT), ultrasound (DCE-US), MRI is the most capable modality for liver imaging due to its superior contrast resolution and its multi-parametric capabilities.

The quantitative estimation of the perfusion parameters of normal and diseased tissues in DCE-imaging is performed by using pharmacokinetic models where the tissue enhancement curve is analyzed in response to the arterial input function (AIF)-inflow of contrast agent (CA).

However, several challenges should be addressed when applying quantitative liver DCE-MRI in clinical practice. One of these challenges is the dual hepatic perfusion in the liver. The usual models, with a single Arterial Input Function (AIF), are not compatible for the liver, because the portal venous inflow needs to be considered. Therefore, dual-input models should be applied, including the Portal Input Function (PIF) in addition to the AIF. These models require a clear difference between the AIF- and PIF- curve shapes to separate their contributions that is induced by fast injection rates and high temporal resolution. The latter is especially challenging when performing DCE-MRI, due to the relatively low temporal resolution of most DCE-MRI sequences. A second challenge is the acquisition of high to noise ratio (SNR) which requires high CA doses. However, high CA doses cause MR signal saturation effects and T2\* effects that underestimate CA concentration and consequently yield considerable quantification errors.

To address the above challenges, we proposed a four-bolus injection scheme with a diluted CA.

## III.2.2 MATERIAL & METHODS

In order to examine if the multi-bolus scheme provides more robust perfusion results than a common single-bolus scheme, a computer simulation was developed by employing real AIF and PIF obtained in rabbits at 4.7T MRI scanner applying both single- and multi (four)-bolus injection schemes. The animal study was fully compliant with the European Community guidelines for the care and use of laboratory animals and was approved by our ethical committee (Project MESR N°2398). Experimental procedures were conducted at the PARCC (INSERM U970, Foundation Carpentier Paris, France). Rabbits were pre-anesthetized by Xylazine (2.5mg/kg), Ketamine (2mg/kg). General anesthesia was maintained by Isoflurane and Oxygen (O<sub>2</sub>) delivered via a supraglottic airway device by a gas anesthesia station.

### *In Vivo Experiments*

#### *MRI Acquisition*

Anatomical multi-slice sequences (T1-weighted and T2-weighted) were performed for the localization of the aorta, the portal vein, and the liver. Liver perfusion was assessed with dynamic T1-weighted echo with three coronal slices over the aorta, portal vein, and liver. The imaging parameters of the sequences are referred in the Paper I.

#### *Bolus-injection schemes*

DCE acquisition of our study was acquired with two different bolus-injection schemes: (a) a single-bolus injection, and (b) multi (four)-bolus injection (Figure 40).

Both injection schemes have had the same acquisition duration at 10min. The volume of each single bolus for both schemes was 4ml of CA with a dilution 1:25. The dilution corresponded to ¼ of the total clinical per bolus. Furthermore, such a low concentration (1:25 dilution) permitted the MR signal saturation and T2\* effects to be decreased in an acceptable point.

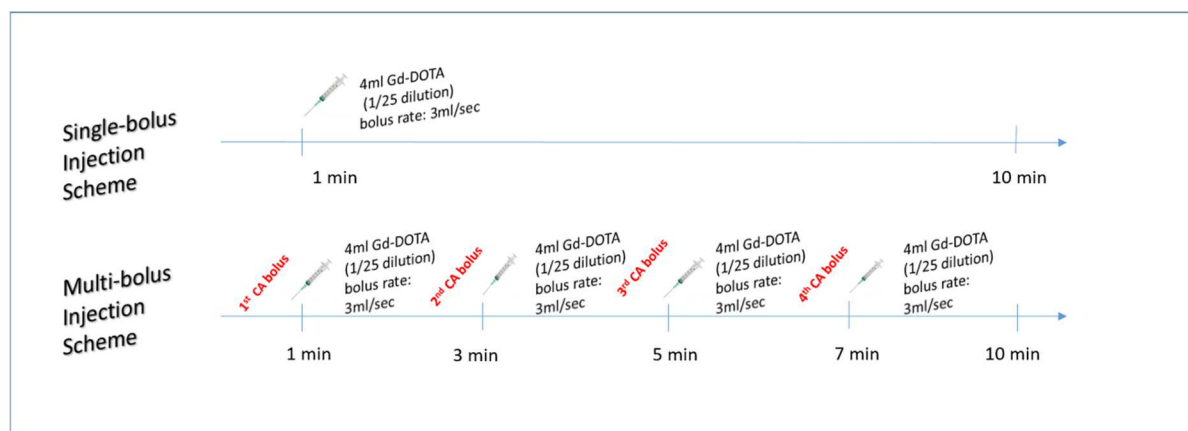


**Figure 40** : Single-bolus injection and multi (four)-bolus injection schemes. The acquisition duration is 10min for both schemes. The bolus volume is 4ml of contrast agent (Gd-DOTA) with a 1:25 dilution and injection rate at 3ml/sec for both schemes.

### Extraction of the vascular enhancement curves

The extraction of the AIF and PIF enhancement curves from the DCE-MRI images was achieved by using in-house software called PhysioD3D developed in Matlab (R2013b; MathWorks, Natick, MA) where region of interest (ROI) were manually drawn over the abdominal aorta (surrogate of aorta) and the portal vein on the frame of the arrival of contrast-agent. Then those ROIs were propagated to the remaining frames of the DCE sequence. The signal intensity of the enhancement curves was measured as arbitrary units, and the enhancement curves were calculated by subtracting the MR signal before the injections (baseline) from the signal after the injections (S-S<sub>0</sub>) (Figure 41).

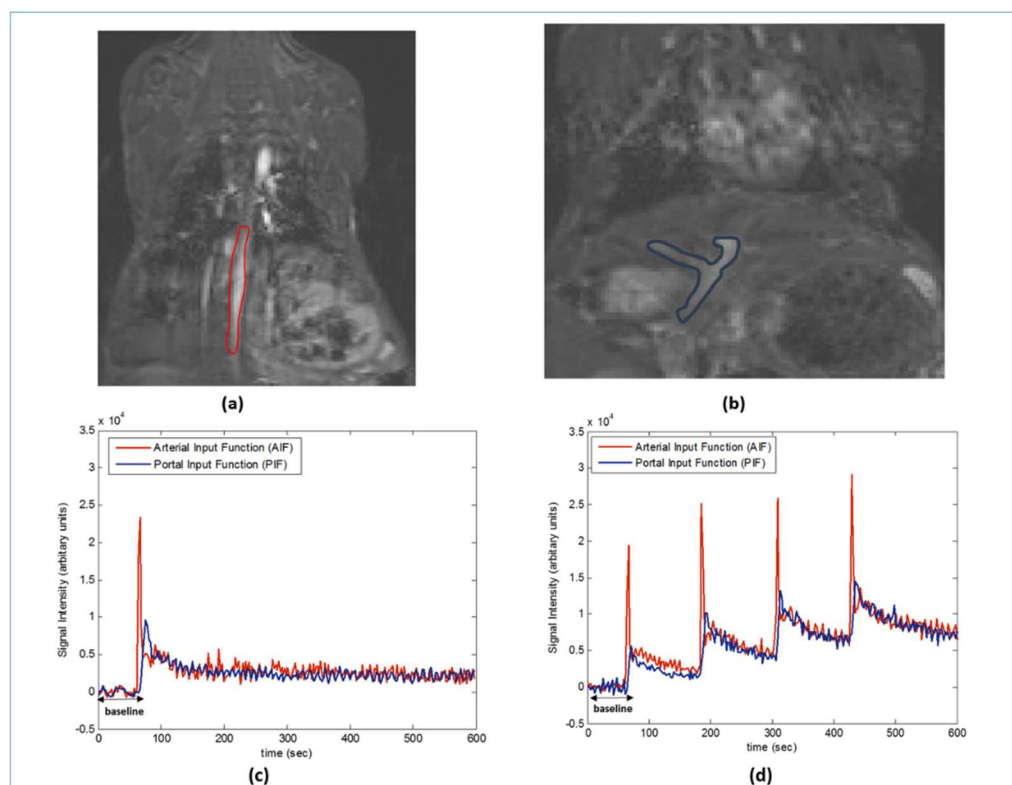


**Figure 41** : Vascular enhancement curves of Arterial Input Function (AIF) and Portal Input Function (PIF) for both injection schemes (c,d) acquired by the respective abdominal aorta ROI (a) and the portal vein ROI (b).

## Simulation experiments

### Simulation rational

The procedure of the simulation divided into three steps (Figure 42): **First**, several liver enhancement curves were generated with different sets of perfusion parameters (Hepatic Perfusion Index; HPI, total tissue blood flow;  $F_t$ , distribution volume;  $v_d$ ) within a given range

(Table 6) applying the AIF and PIF acquired in-vivo with both single-bolus and multi-bolus injection schemes.

**Table 6:** Initial perfusion parameters' range

	Values	HPI (%)	$v_d$ (%)	$F_t$ (ml/min/100ml)	T (sec)
Liver	Min	15	22.5	150	0
	Max	45	37.5	200	0.001

**Second**, the estimated perfusion parameters were extracted back by using the fitting technique. **Third**, the errors between initial and estimated parameters were evaluated for both injection schemes through the Coefficient of Variation (CV).

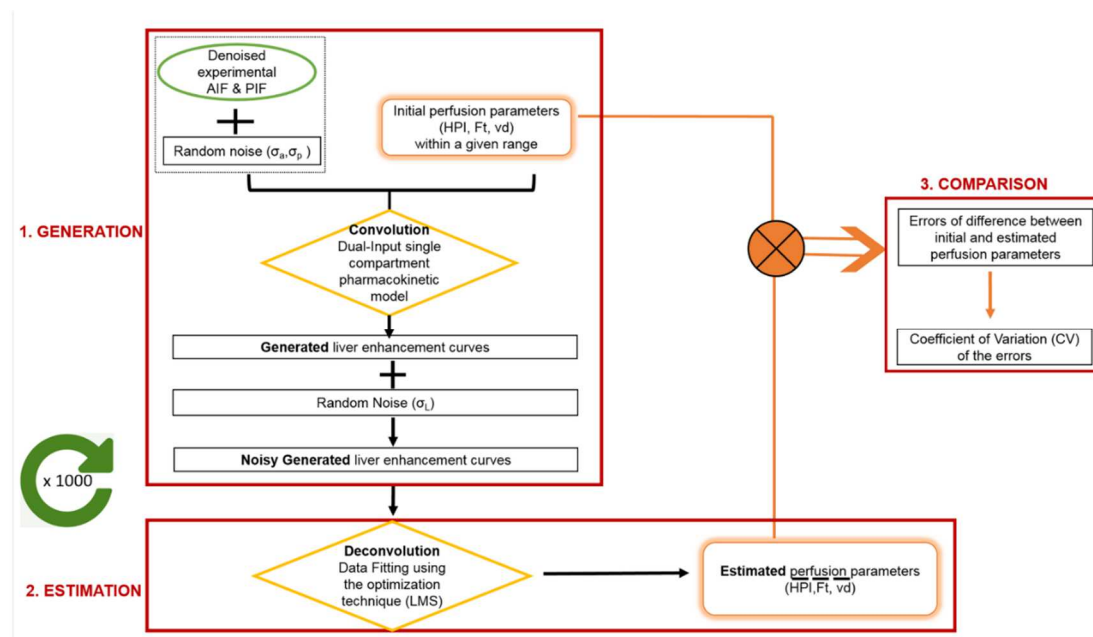


**Figure 42 :** Simulation workflow.

### Statistical Analysis

F-test was used to evaluate the variability of CV of the perfusion parameters in both schemes.  $p < 0.002$  was statistically considered significant by including Bonferroni multi-test correction.

### III.2.3 RESULTS

The input enhancement curves of the simulation originated from the same rabbit for both injection schemes.

### Multi-bolus injection scheme evaluation

The variability of the measurement of the perfusion parameters significantly decreased when increasing the number of bolus injections. The most remarkable improvement was noticed for HPI parameter (Figure 43).

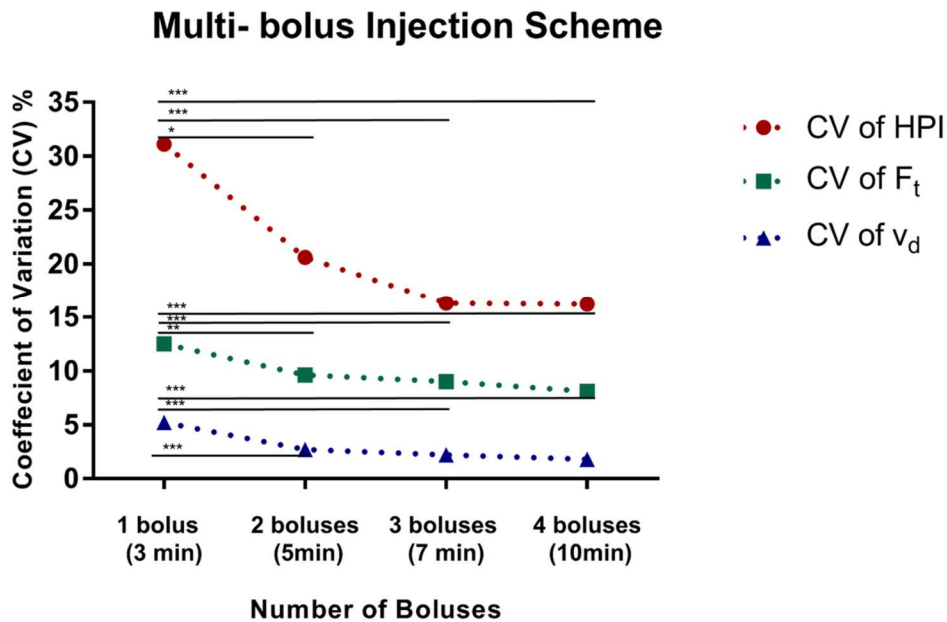


**Figure 43 :** Variability of the perfusion measurement applying the multi-bolus injection scheme. HPI: Hepatic perfusion index, Ft: total tissue blood flow, vd: distribution volume, CV: coefficient of variation. p-values extracted by performing the F-test.  $p \leq 2 \cdot 10^{-3}$ : \*,  $p \leq 2 \cdot 10^{-4}$ : \*\*,  $p \leq 2 \cdot 10^{-5}$ : \*\*\*

### Single-bolus injection scheme evaluation

There was no significant improvement of the variability for the measurement of all perfusion parameters as increasing the duration of the acquisition time. Specifically, HPI variability degraded with longer acquisition durations (Figure 44).

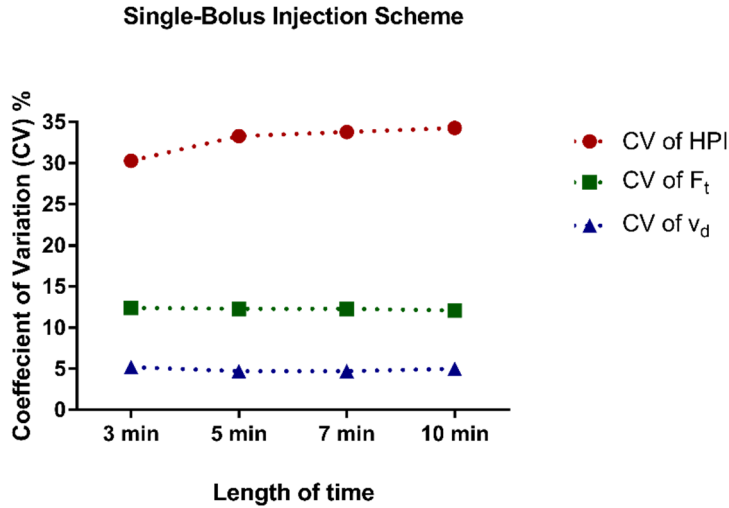


**Figure 44** : Variability of the perfusion measurement increasing the acquisition duration with the single-bolus injection scheme. HPI: Hepatic perfusion index,  $F_t$ : total tissue blood flow,  $v_d$ : distribution volume, CV: coefficient of variation.

## III.2.4 DISCUSSION

Our aim was to improve the DCE-MRI technique to increase the robustness of the measurement of the hepatic perfusion parameters.

Especially, we achieved less signal saturation and susceptibility ( $T2^*/T2$ ) effects as well as remaining in the quasi-linear part of the signal to CA concentration relationship decreasing the concentration of CA (1/25 dilution) while keeping a reasonable amount of CA for sufficient signal to noise ratio (SNR) increasing the bolus volume (4ml). Those achievements were accomplished by applying the multi-bolus injections strategy.

The evaluation of the multiple strategy proved that performing our multi-bolus injection scheme, the robustness of the perfusion measurement significantly increased compared to the single-bolus scheme. The outstanding improvement was for HPI which is a crucial parameter for the perfusion analysis of both the liver and the hepatic tumors.

Furthermore, another limitation of DCE-MRI technique is the mis-sampling of data because of its low temporal resolution. Applying the multi-bolus strategy, we managed to increase the number of measures during the crucial bolus peak that provides important information regarding the concentration of CA in the vascular space employing a moderate temporal resolution (2.4msec). So, we increased the statistical power of parametric assessment and increased the robustness of the measurement.

### **III.2.5 CONCLUSION**

This study developed the technique of multi-bolus injection with low concentration of CA. This technique could overcome major limitations of DCE-MRI such as MR signal saturation and T2\* effects and the mis-sampling of data increasing the robustness of the perfusion parameters' measurement. Furthermore, the improvement of the HPI robustness could be applied in the upcoming future for the tumor diagnosis and treatment monitoring.

## III.3 VX2 TUMOR HANDLING AND TREATMENT

### III.3.1 VX2 TUMOR HANDLING

The rabbit VX2 tumor model is used in experimental oncology since several years. It was developed in 1930-1940 by Rous et al <sup>69,70</sup>. It is a virus-induced anaplastic squamous cell carcinoma that is characterized by hyper-vascularity, high growth rate, and easy propagation in the skeletal muscle. It has also been used to model cancers of the head and neck, kidney, brain, lung, urinary bladder, uterus, liver, bone and pancreas. This model has also a wide use in interventional radiology. Additionally, the recent years, it has been employed in numerous studies correlated with the imaging and the treatment of hepatocellular carcinoma.

#### ***VX2 Tumor Implantation***

Thirty-six New Zealand female rabbits (2.5 -3kg) and twelve New Zealand male rabbits (3.5-4kg) were undergone to VX2 tumor implantation throughout my thesis.

Two different techniques have been applied during my work. Each involved **carrier rabbits** used to grow up tumors before their implantation in **receiver rabbits**, which were used for the MRI study. The first technique involved the implantation of tumor fragments in the liver for both carrier rabbits and receiver rabbits, while the second technique involved the injection of a suspension of tumor cells in the limb of the carrier rabbits to develop tumor tissue which is then implanted in the receiver rabbits.

#### *First tumor implantation technique*

Regarding the first technique, I attended a training at the Guerbet company (Aulnay-sous-Bois, Paris, France), where I was supplied with the first tiny VX2 fragments for the tumor implantation. Thirty-six New Zealand female rabbits were used for this technique. The procedure is described below.

#### *Anesthesia protocol*

Mixture of Ketamine (2mg/kg) and Xylazine (2.5 mg/kg) was intramuscularly medicated to the donor rabbits 15 minutes before the intervention. During the operation, general anesthesia was maintained by Isoflurane 2-3% and Oxygen (O<sub>2</sub>) 100% delivered through a supraglottic airway device (V-gel, Dicsinnovent, ([www.docsinnovent.com](http://www.docsinnovent.com))) by a gas anesthesia station and a medical respiration armlet was applied to monitor respiration rate (60-100pulse/min). The

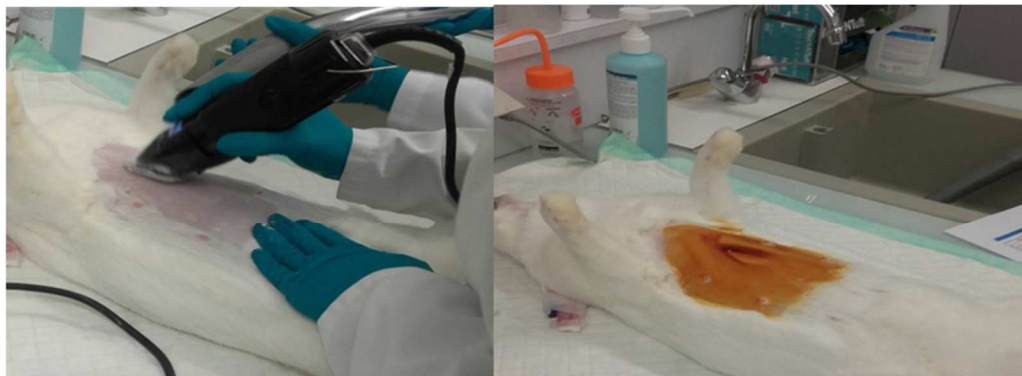
intravenous access for the saline was secured via a marginal ear vein with the use of catheter (Figure 45).



**Figure 45** : Cardiac monitoring armlet around the anterior paw of the rabbit (black straight arrow), v-gel mask connected with the isoflurane gas application (dashed arrow), and ear catheter (red straight arrow).

#### *Implantation protocol*

After shaving and applying two types of Betadine (betadine soap, betadine solution) on the rabbit abdomen by circular movements from in to out (Figure 46), the abdomen was draped in standard surgical fashion (Figure 47).



(a)

(b)

**Figure 46** : (a) rabbit abdomen shaving, (b) betadine application on the rabbit abdomen

A vertical oriented subxyphoid mini-laparotomy was performed with a 15-blade, and a blunt dissection was employed to expose the peritoneum (Figure 47a). Careful division of the peritoneum permitted visualization of the liver. The exposed section of the liver was kept moist with wet gauze (Figure 47b). The left lateral lobe was pulled out for the implantation, as based

on investigations(the left lateral hepatic lobe is preferable for the VX2 tumor implantation due to a more favorable angle of the feeding artery for later angiographic catheterization <sup>71</sup>).

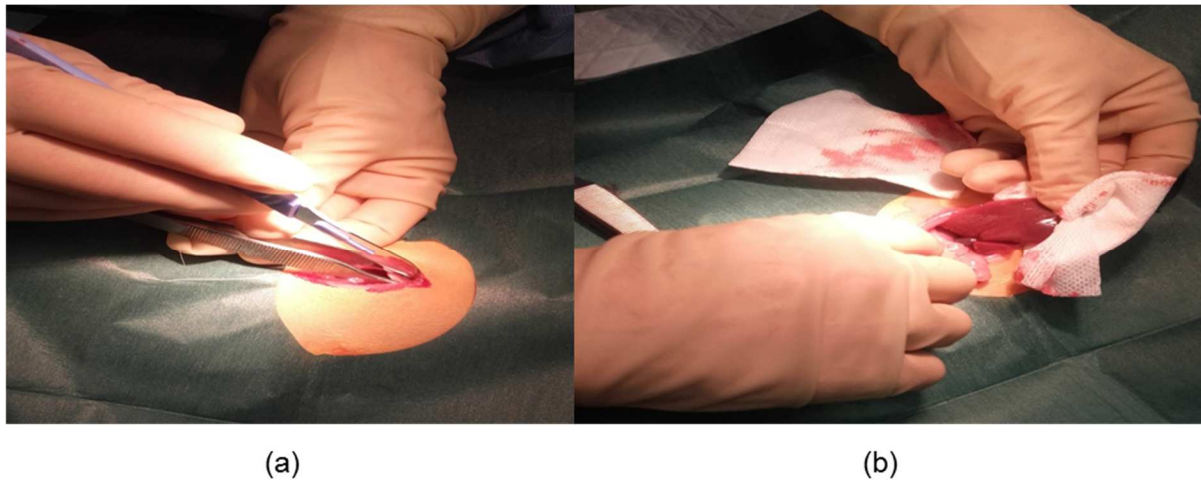


**Figure 47 :** (a) Vertical oriented mini-laparotomy abdominal incision with a 15-blade and a blunt dissection. (b) Liver is kept moist with the help of a wet gauze.

Vertical incision was performed with the tip of a fine forceps at the hepatic sites of the tumor implantation. Hemostasis, at the incision sites, was accomplished with gauzes' application. Single solid VX2 tumor fragment was placed atop each of two incisions at the left lateral lobe and gently pushed into the parenchyma with the tip of fine forceps (Figure 48b).

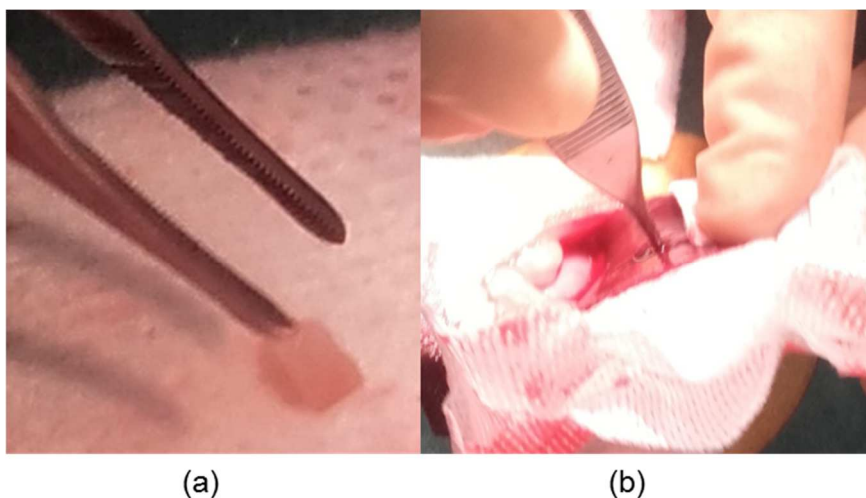


**Figure 48 :** (a) Solid VX2 tumor fragment. (b) Gentle push of the VX2 fragment into the liver parenchyma with the tip of a fine forceps.

The abdominal incision was closed in two layers using 3-0 silk suture (3-0, VICRYL\*PLUS, V-34, 90cm) for fascial repair performing one by one stitch (Figure 49a) and cutaneous ligation with a constant steam (Figure 49b), respectively. At the end of the operation Betadine was applied on the first layer of the incision and on the cutaneous sutures for preventing infections.

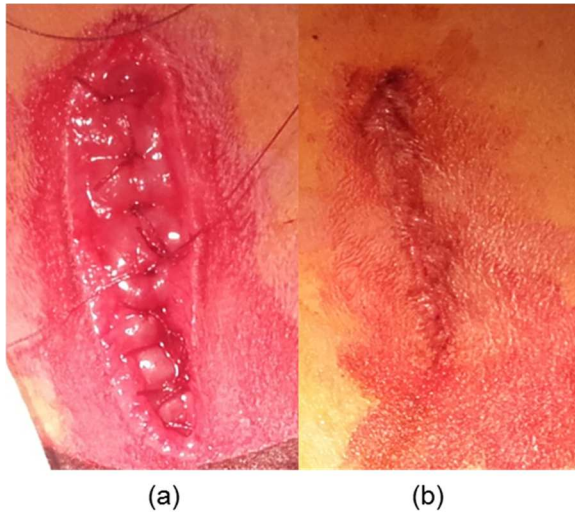
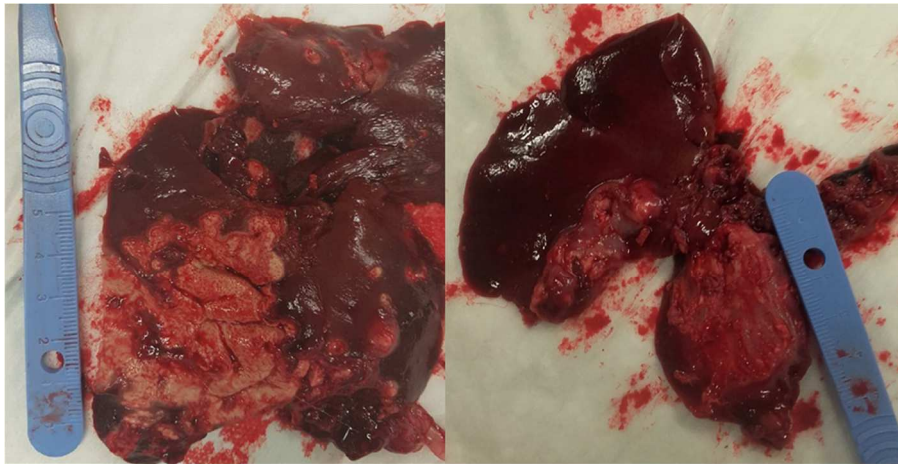


**Figure 49** : (a) Fascial repair sutures. (b) Cutaneous ligation sutures

Post-operatively, analgesic patch (Durogesic; 12 $\mu$ g/h) was applied at the rabbit nape. The tumor fragment yielded a palpable VX2 tumor within 24-25 days. The tumor growth was confirmed by magnetic resonance imaging (MRI).

#### *Results of the first implantation protocol*

Although the implantation protocol was followed as shown by the Guerbet team, the fragments of the VX2 that were implanted to the carrier rabbits yielded inconsistent results, with surprisingly long growth periods of 25 days as opposed to the usually reported period of 15 days after the implantation. Thus, we were not sure if the harvested VX2 fragments corresponded to good VX2 strain for the receiver rabbit implantation and then for the tumor treatment. Finally, it was suspected that those VX2 strains were contaminated because the palpable tumors that were yielded from the receiver rabbits were huge and aggressive, based on the autopsy images (Figure 50), and did not look like typical VX2 tumors. Consequently, we could not use the animals prepared with this VX2 strain and implantation technique to test the effect of the treatment.



(a)

(b)

**Figure 50** : (a,b) Aggressive and probably virus stem VX2 tumor

### *Second tumor implantation technique*

Twelve male rabbits were used in this second series. Because the first implantation technique failed, we looked for the help of a team which was mastering the VX2 handling. The team of Archimmed company has a long and successful story in that field. They use a procedure of tumor implantation with two different steps: in the first step a suspension of tumor cells is injected in the limb of the carrier rabbits to develop tumor tissue, then in the second step fragments of tumor (harvested from the limb tumor) are implanted in the receiver rabbits through laparotomy.

**Step 1 VX2 Carrier induction:** Two carrier rabbits were used for the VX2 implantation in order to yield palpable nodules for further implantation into the liver. VX2 tumors were first grown in the hind limbs of the anesthetized carrier rabbits by injection of a frozen cellular suspension obtained as described by Rao et al<sup>72</sup>. Two weeks later the carrier rabbit was euthanized by intravenous injection of pentobarbital (5ml [200mg/ml] Doléthal-Vetoquinol, France) and the tumors were aseptically harvested in RPMI 1640 medium supplemented with 1% fetal calf serum. The tumors were dissected and viable fragments of 2-3mm were selected for further implantation into the liver.

**Step2 Liver VX2 tumor Implantation in receiver liver:** The procedure was identical with the 1<sup>st</sup> implantation technique. The tumor grew up within a 14-15 days after the implantation. Growth of implanted tumors was confirmed by ultrasonography (US) (MyLab™Gamma Esaote, Genoa, Italy, 3-13 MHz probe (SL 1543).

This protocol yielded a very good success rate 10 out of 10 rabbits with typical VX2 tumors around 2 cm in diameter (Figure 51)

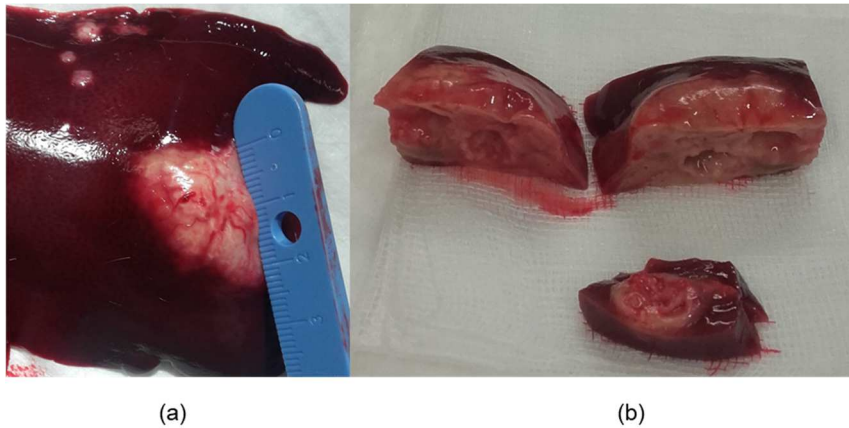


**Figure 51** : (a) VX2 tumor nodule. (b) the respective slices of VX2 tumor

### ***Tumor harvesting for implantation in the receiver rabbits***

In the carrier rabbits a viable tumor yielded a palpable nodule within 2-3 weeks of implantation.

Signs of tumor growth in rabbit include:

1. Decreased appetite
2. Loss of caecotrophy (the ingestion of nocturnal feces is common to lagomorphs)
3. Lethargy increased
4. Fever with highly necrotic tumors

Ultrasonography and MRI confirm tumor growth.

The fragments of tumor were implanted in the receiver livers:

1. After the bisection of the tumor in small fragments at the moment of the autopsy (applied to the second implantation technique) or
2. After the thawing, just before implantation (applied to the first implantation technique).

The harvesting of the tumor from the carrier rabbit enables the intrahepatic implantation to 6-10 receiver rabbits.

The tumor manipulations were being performed under highly sterile conditions.

#### ***Harvesting Procedure***

The carrier rabbits were intramuscularly medicated with a mixture of Ketamine (2mg/kg; Imalgène 1000), and Xylazine (2.5mg/kg; Rompun) and sacrificed performing an intravenous dose of Doléthol (1ml/kg).

Regarding the VX2 tumor extraction, the cutaneous and subcutaneous tissues overlying the tumor nodule were divided and the liver tumor exposed. The size of tumor growth of each specimen was about 2x2x1cm<sup>3</sup>.

The explanted specimen was being dissected, permitting visualization of the necrotic core and peripheral viable tumor. Gentle scraping with a 22-blade easily removed the necrotic core for careful separation of viable tumor from adherent muscle tissue (Figure 52).

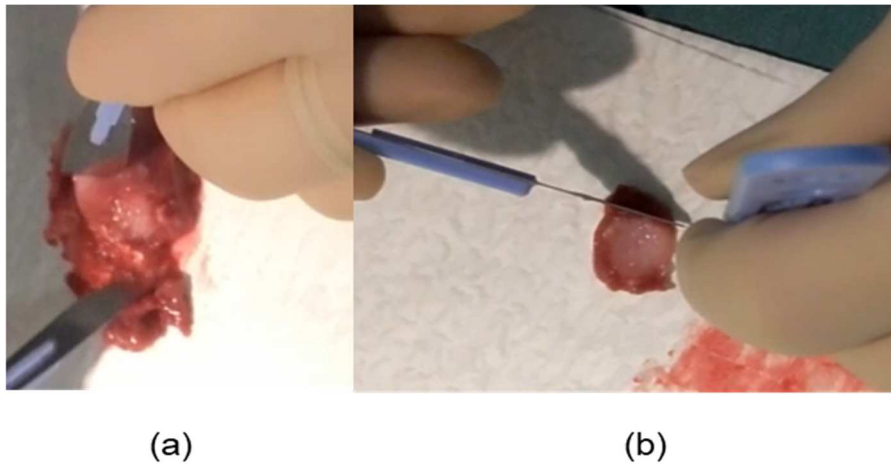


**Figure 52** : (a) Gentle scraping for the removal of necrotic core. (b) Separation of viable tumor from adherent muscle tissue

The viable tumors were being bisected to small pieces of  $25\text{mg} \pm 1\text{mg}$  size and stored in sterile saline for immediate subsequent intrahepatic implantation.

The remaining tumor was bathed in nutrient-rich medium (Figure 53) consisted by:

- 1.5ml rabbit serum
- 1.5ml glycerol
- 12ml of medium RPMI 1640

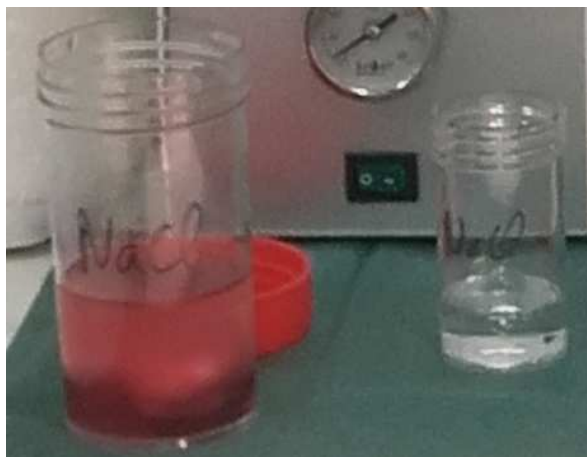


**Figure 53** : Bathing of tumor in the nutrient-rich solution (left). Small fragments of tumor, for immediate intrahepatic implantation, stored in the physiologic serum (right).

Storage of the tumor fragments in sterile saline enables the tumor fragments keep cold up to 2-3 hours later. During any waiting time among the rabbits which were going to undergo intrahepatic implantation, the tube had to be placed in the freezing machine in temperature of  $4^{\circ}\text{C}$ .

### ***VX2 Tumor conservation and transport***

In case of no immediate intrahepatic implantation, we were preparing the tumor fragments, under sterile conditions, in cryotubes of 1ml nutrient-rich medium. Up to 4 tumor fragments were being deposited per tube. The cryotubes were being placed in the freezing machine at the temperature of  $-80^{\circ}\text{C}$  in order to freeze. The next day of freezing, the cryotubes were being placed in liquid nitrogen.

The thawing of the frozen cryotubes, the time of the intrahepatic implantation, was being performed with rapid rub using the hands. Then, the content of the cryotubes was being removed in a big sterile tube which contained an amount of serum of 200ml. During any waiting time, the cryotubes were being placed in the freezing machine in temperature of  $4^{\circ}\text{C}$ .

The transportation of the frozen cryotubes to operation room for the intrahepatic implantation was done in containers with liquid nitrogen not totally sealed to avoid explosion. The liquid nitrogen was manipulated in a well-ventilated room to avoid suffocation.

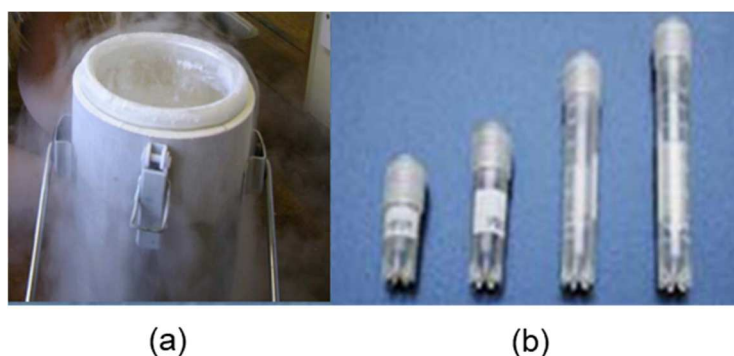


**Figure 54** : (a) Liquid nitrogen container. (b) cryotubes in different sizes

### **III.3.2 VX2 TUMOR TREATMENT: TRANSCATHETER ARTERIAL EMBOLIZATION (TAE)**

Hepatocellular carcinoma is associated with liver cirrhosis in 80% of cases. When the tumor is diagnosed, the surgical resection is often contraindicated in most cases. In those cases, treatment of HCC can be accomplished with different procedures. One of them is the transarterial embolization (TAE) that was applied in our study. This procedure blocks the blood supply to a tumor. Thoroughly, a small incision is made in the inner thigh and a catheter is inserted and guided into an artery close to tumor. Once the catheter is at the correct position, small particles made of tiny gelatin sponges or beads are administrated. Thus, the artery is blocked and the flow of blood to tumor stops.

In our study, the TAE treatment was performed by an interventional radiologist (Olivier Pellerin) of our team according to conventional protocols used in human. Specifically, trans-catheter hepatic artery catheterization and embolization were guided by fluoroscopy. The left hepatic artery was selectively catheterized through a 4-French sheath femoral access with a microcatheter (Terumo Europe Leuven Belgium). From this position, 1mL of Embosphere 100-300 $\mu$ m (Merit Medical; South Jourdan UT, US) were slowly injected in the left hepatic artery over a 1-min period as close as possible to the tumor. The end point of the technical procedure was the completed occlusion of the tumor arterial network. Specific attention to avoid any reflux into no-targeted arteries. Upon completion of the intra-arterial injection, the catheter was removed.

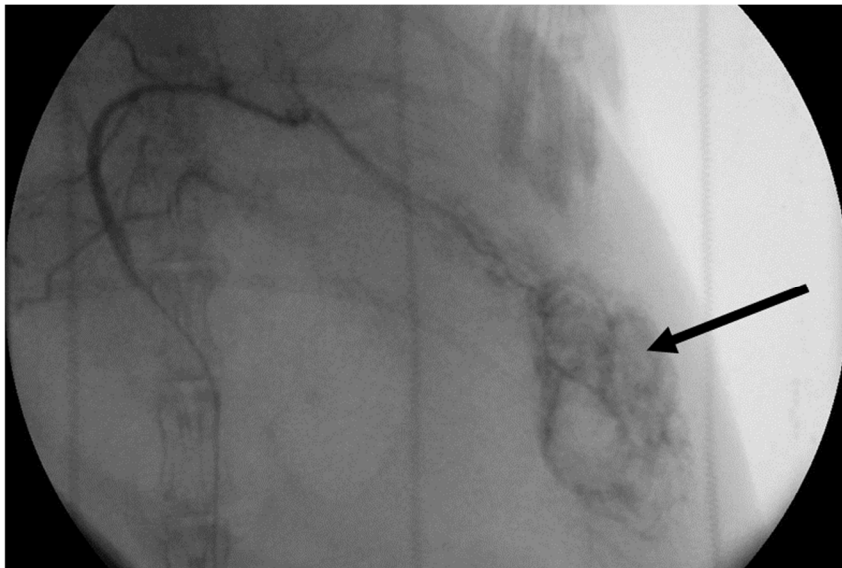


**Figure 55** : Angiography of a liver bearing a VX2 tumor The vascularization of VX2 tumor is clear (black arrow).

## **III.4 IN VIVO TESTING OF THE FOUR BOLUSES STRATEGY (*PAPER II; IN PREPARATION*)**

To test our “four boluses strategy” we performed a study on rabbit livers bearing VX2 tumors before and after transcatheter arterial embolization. We present below the results of this study, which correspond to the paper N°2 (in preparation).

### **III.4.1 INTRODUCTION**

The aim of this study was to validate *in vivo* the efficiency of the multi-bolus injection scheme, which we proposed and tested on simulations in the 1<sup>st</sup> paper. We wanted to test if DCE-MRI, with this new injection scheme, allows a clear discrimination of tissues, such as liver and tumor, as well as tumor pre- and post-embolization, based on the measured perfusion parameters.

### **III.4.2 MATERIAL AND METHODS**

#### ***Animal and Tumor model***

Twelve adult New Zealand White male rabbits (age=6-7months; body weight=3.5-4.2 kg) were used in this study.

Animals were housed under the supervision of a trained veterinary team. The overall health and well-being of each animal was monitored daily. All animals were killed at D23 by general anesthesia (4% Isoflurane with 100% oxygen), and an overdose of sodium pentobarbital (5ml ;200mg/kg).

VX2 tumor cells were provided and implanted by Dr. Florentina Pascale, veterinarian from Archimmed (Jouy en Jossas). VX2 carcinoma cells were used to induce tumor growth in the liver, thus modeling hepatic arterial supply patterns similar to hepatocellular carcinoma at 13–15 days following transplantation. The procedure of the VX2 implantation that was followed, it is described above in the section of second implantation technique.

After the growth of the VX2 tumor, transcatheter arterial embolization (TAE) was applied to the tumor. The treatment procedure is described above in the section of VX2 tumor treatment.

#### ***Animal Study Design***

Our study was designed to observe statistically significant differences on VX2 tumor before and after treatment by applying the four-bolus DCE-MRI protocol.

### Dynamic Imaging and Treatment timeline

DCE-MRI was performed to rabbits fourteen days after VX2 tumor implantation for the pre-embolization baseline. TAE treatment was performed sixteen days after the tumor implantation, and immediately after the TAE procedure a DCE-MRI was performed for post-embolization recording. Seven days later the rabbits were sacrificed, and sections of the tumor and liver tissues were harvested for histology analysis. The timeline of DCE-MRI and TAE treatment is illustrated in Figure 56.

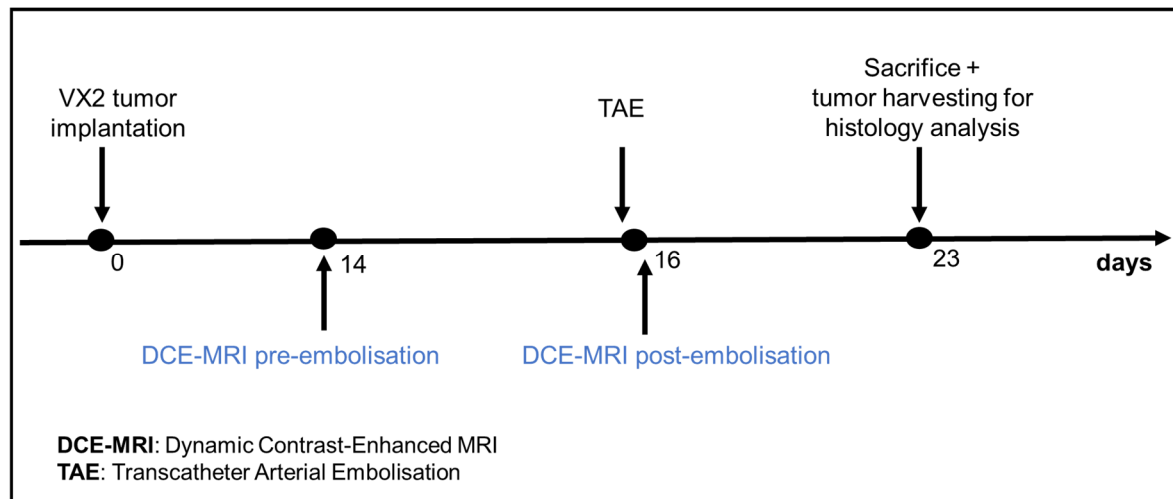


Figure 56 : DCE-MRI and TAE treatment timeline.

### MRI Acquisition

Images were acquired with a Bruker Biospec 4.7T MRI scanner employing dedicated rabbit gradient coil. Rabbits were pre-anesthetized by Xylazine (2.5mg/kg), Ketamine (2mg/kg). Intravenous access was secured via a marginal ear vein for saline infusion and MR contrast-agent injection. General anesthesia was maintained by Isoflurane (2-3%) and oxygen (100%) delivered through a supraglottic airway device (V-gel, Dicsinnovent, ([www.docsinnovent.com](http://www.docsinnovent.com))) by a gas anesthesia station (Minerve; Tec 7). The breathing rate was adjusted between 25-30 breaths/min and used to synchronized MR pulse sequences.

Anatomical multi-slice sequences (T1-weighted and T2-weighted) were performed for the localization of the aorta, portal vein, liver, and tumor. Liver and tumor perfusion were assessed with a 2D dynamic T1-weighted gradient echo sequence (FLASH) with three coronal slices over the aorta, portal vein, and tumor/liver. The imaging parameters of the sequences are depicted in Table 7.

**Table 7** : MRI sequences

	T <sub>1</sub>	T <sub>2</sub>	DCE
<b>Sequence Type / Slice Orientation</b>	<b>RARE (2D) / Coronal</b>	<b>TurboRARE (2D) / axial</b>	<b>FLASH (2D) / coronal</b>
<b>Flip Angle</b>	90°	90°	70°
<b>TR / TE (ms)</b>	975.9 / 12.6	3420 / 50.1	23.9/ 2.9
<b>Thickness (mm)</b>	3	2	3
<b>Slices Number</b>	15	21	3
<b>Temporal Resolution</b>	-	-	2sec 37ms
<b>Repetitions</b>	1	1	253
<b>Total Time</b>	4min 49sec	5min28sec	10min

### *Multi-bolus injection Scheme*

The multi-bolus scheme that was performed in this study described in the Paper I, and depicted in Figure 57.

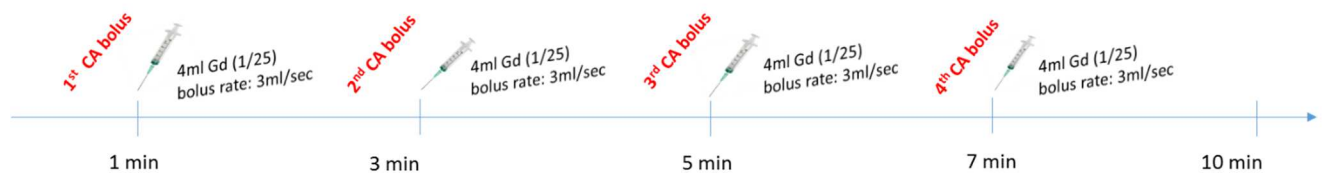


**Figure 57** : Multi (four)-bolus injection scheme

### *Histopathology Evaluation*

One-week post-embolization, all rabbits were sacrificed. Sections from both the embolized VX2 tumor and the liver lobes around tumor were harvested post-embolization. Tissue specimen were fixed in 4% formalin solution (20 hours) and then processed to paraffin tissue blocks. Blocks were cut in 4µm sections and then stained with hematoxylin and eosin (H&E) for histology analysis. The hematoxylin and eosin slides were blindly evaluated by a more-than-ten-year experienced pathologist (Tchao.Méatchi) evaluating the **tumor regression grade (TRG)** based on the classification of Mandard's study <sup>73</sup>. Specifically, the tumor regression is classified into five histological TRGs based on vital tumor tissue at the ratio of fibrosis: TRG-1 (complete regression; 100% fibrosis), TRG-2 (fibrosis with scattered tumor cells), TRG-3 (fibrosis and tumor cells with preponderance of fibrosis), TRG-4 (fibrosis and tumor cells with preponderance of tumor cells), TRG-5 (no tumor regression).

## DCE-MRI image analysis

### Region of Interest (ROI)

The acquired DCE-MRI images were sent to in-house software, PhysioD3D, developed in Matlab (R2013; Mathworks, Natick, MA). The signal enhancement curves were obtained from Regions of Interest (ROI) drawn manually over the aorta, the portal vein, the liver parenchyma, and the tumor based on the description of the Paper I. Figure 58 shows the ROIs drawn on the above regions from one single rabbit and the corresponding signal enhancement curves over time obtained for two different temporal times (pre-embolization & post-embolization).

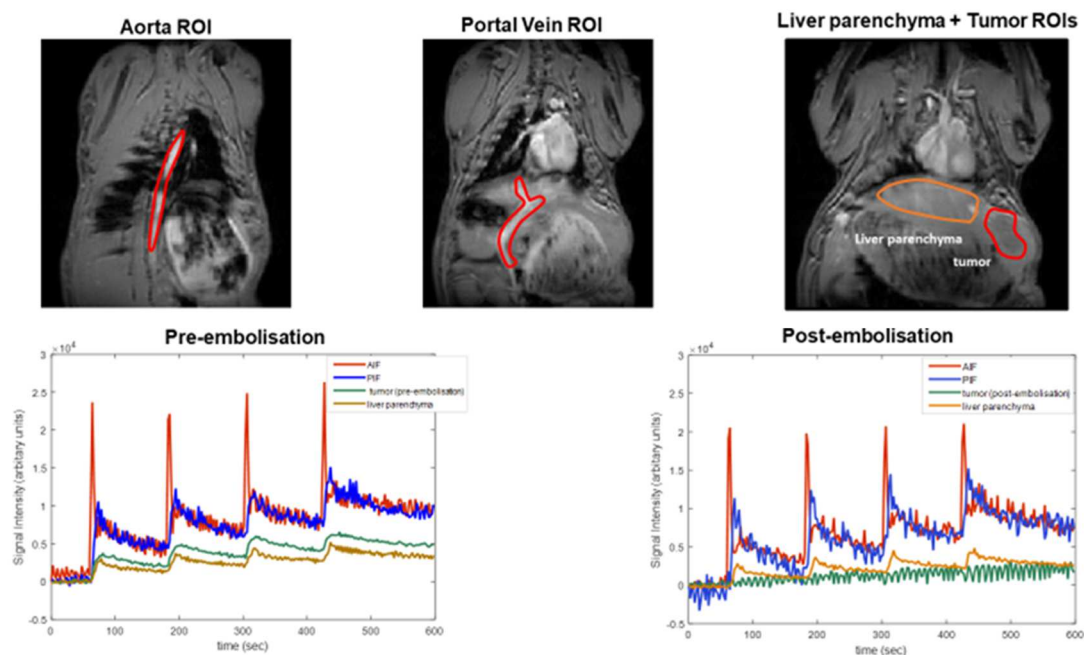


**Figure 58** : ROIs and respective enhancement curves from the same rabbit pre-embolisation and post-embolisation. Pre-embolisation, the signal of the tumor is higher than the liver while post-embolisation, because of the embolisation, the signal of the tumor is lower than the liver.

### Signal analysis

The entire signals of the AIF, PIF, liver, and tumor enhancement curves were divided into four sub-signals that corresponded to time interval of a single bolus of the multi-bolus injections scheme. Then, the baseline obtained before the first injection of the entire signal was subtracted from each sub-signal for each single tissue. In continue, the median value from the four sub-signals was calculated. Finally, the resulting signals were used for the extraction of the perfusion parameters, applying a dual-input single-compartment pharmacokinetic model (see Chapter II.4.2; equation 14) with a non-linear optimization fitting technique provided by the Matlab toolbox (Least Mean Square [LMS]). The values of parameters that yielded the best fit of the curves were recorded as the best values for the perfusion parameters. The perfusion parameters that were considered in this study are described below:

**Hepatic perfusion Index (HPI):** Percentage of the hepatic arterial perfusion in the tissue. Expressed in percentage (%).

**Liver distribution volume (vd):** Percentage of tissue volume in which the contrast agent distributes into the liver tissue. Expressed in percentage (%).

**K<sup>trans</sup>:** It determines the transport rate of the contrast agent from plasma into the tissue. Expressed in ml/min/100ml of tissue.

#### *Tissue Comparison*

The tissues (liver, tumor) in different temporal times (pre- and post-embolisation) were compared, for each perfusion parameter (HPI, K<sup>trans</sup>, vd).

#### *Statistical analysis*

In regard to the small amount of the samples, we used the median rather than the mean, and evaluated the statistical variation as the Median Absolute Deviation (MAD) which is a robust measure of the variability of a univariate sample of quantitative data.  $MAD = median(|X_i - \bar{X}|)$

where  $\bar{X} = median(X)$

The non-parametric Wilcoxon signed rank test was employed to evaluate the paired differences between liver and tumor perfusion parameters for each temporal time (pre- and post-embolization), as well as the paired differences between pre- and post- embolization perfusion parameters for each tissue.  $p < 0.05$  was considered statistically significant.

### **III.4.3 RESULTS**

#### ***Perfusion Results***

Among ten rabbits, one rabbit passed away immediately after the embolization procedure. Two rabbits were excluded from the pre-embolization analysis and one rabbit from the post-embolization analysis due to bad quality results. Consequently, the results of the measurement of the perfusion parameters pre- and post- embolization were based on eight rabbits.

#### *Fitting*

The fitting was performed on the median tissue signal from the four sub-signals which was applied to the image analysis (Figure 59).

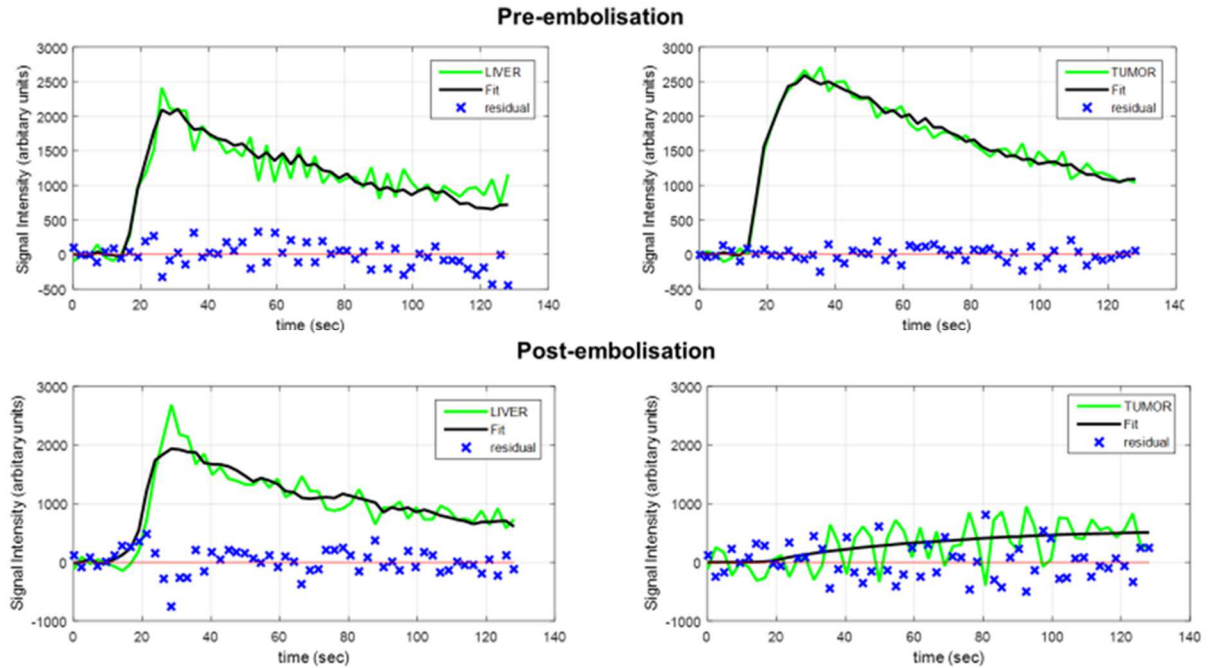


**Figure 59** : Typical fitting (in black) of the tissue enhancement curves (in green) of the liver (left) and the tumor(right) with the single-compartment model, pre-embolisation (upper curves), and post-embolisation (bottom curves). The residual of the fitting process is displayed as blue crosses, and remains well centered around the zero level, attesting the quality of the adjustment.

### Perfusion Analysis

The median values of the parameters are displayed on Figure 60 and summarized in Table 8. Each paired variations of the parameters are displayed on Figure 61, their mean differences and their significances are summarized in Table 9.

For pre-embolization, median HPI is 14 ( $\pm 13.2$ ) % in the liver, and 50.5 ( $\pm 29.1$ ) % in the tumor respectively ( $p= 0.078$ ), while for post-embolization, it is 1.0 ( $\pm 1.1$ ) % in the liver, and 1.0% ( $\pm 14.7$ ) in the tumor.

For pre-embolization, median  $K^{\text{trans}}$  has a significant difference between liver and tumor (liver 246.0 ( $\pm 76.7$ ) ml/min/100ml, tumor 264.0 ( $\pm 260.9$ ) ml/min/100ml) ( $p=0.94$ ). However, their difference appear clearly post-embolization; (liver 190.2 ( $\pm 26.6$ ) ml/min/100ml, tumor 7.2 ( $\pm 39.3$ ) ml/min/100ml) ( $p=0.016$ ).

For pre-embolization, median  $vd$  is 28.5 ( $\pm 5.3$ ) % in the liver, and 39.2 ( $\pm 6.5$ ) % in the tumor ( $p=0.078$ ). For post-embolization, median  $vd$  is highly decreased 5.8 ( $\pm 15.1$ ) % in the tumor but not in the liver 23.0 ( $\pm 3.5$ ) % ( $p=0.078$ ).

Figure 60 depicts the above results.

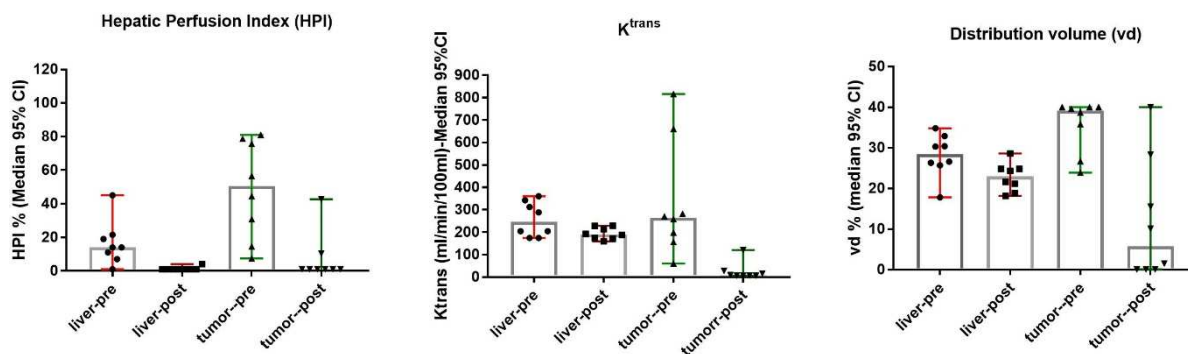


**Figure 60** : pre- and post-embolisation perfusion parameters of the tissues (liver, tumor) for the Hepatic Perfusion Index (HPI),  $K^{trans}$ , and distribution volume (vd) parameters. The measurements are expressed as median with 95% Confidence Interval (CI).

**Table 8** : Median values of perfusion parameters values of the liver and the tumor pre- and post-embolisation. *MAD: Median Absolute Deviation. SD: Standard Deviation*

TISSUE		HPI (%)	$K^{trans}$ (ml/min/100ml)	vd (%)
LIVER pre-embolisation	Median ( $\pm$ MAD/ $\pm$ SD)	14.0 ( $\pm$ 5.95/ $\pm$ 13.2)	246.0 ( $\pm$ 69/ $\pm$ 76.7)	28.5 ( $\pm$ 2.45/ $\pm$ 5.3)
LIVER post-embolisation	Median ( $\pm$ MAD/ $\pm$ SD)	1.0 ( $\pm$ 0.0/ $\pm$ 1.1)	190.2 ( $\pm$ 21.0/ $\pm$ 26.6)	23.0 ( $\pm$ 1.85/ $\pm$ 3.5)
TUMOR pre-embolisation	Median ( $\pm$ MAD/ $\pm$ SD)	50.5 ( $\pm$ 26.7/ $\pm$ 29.1)	264.0 ( $\pm$ 87/ $\pm$ 260.9)	39.2 ( $\pm$ 0.85/ $\pm$ 6.5)
TUMOR post-embolisation	Median ( $\pm$ MAD/ $\pm$ SD)	1 ( $\pm$ 0.0/ $\pm$ 14.7)	7.2 ( $\pm$ 1.2/ $\pm$ 39.3)	5.8 ( $\pm$ 5.7/ $\pm$ 15.1)

The non-parametric Wilcoxon signed rank test has been performed on seven rabbits. Two rabbits out of ten rabbits have had bad quality results and excluded from the analysis, and one rabbit passed away immediately after the embolization technique.

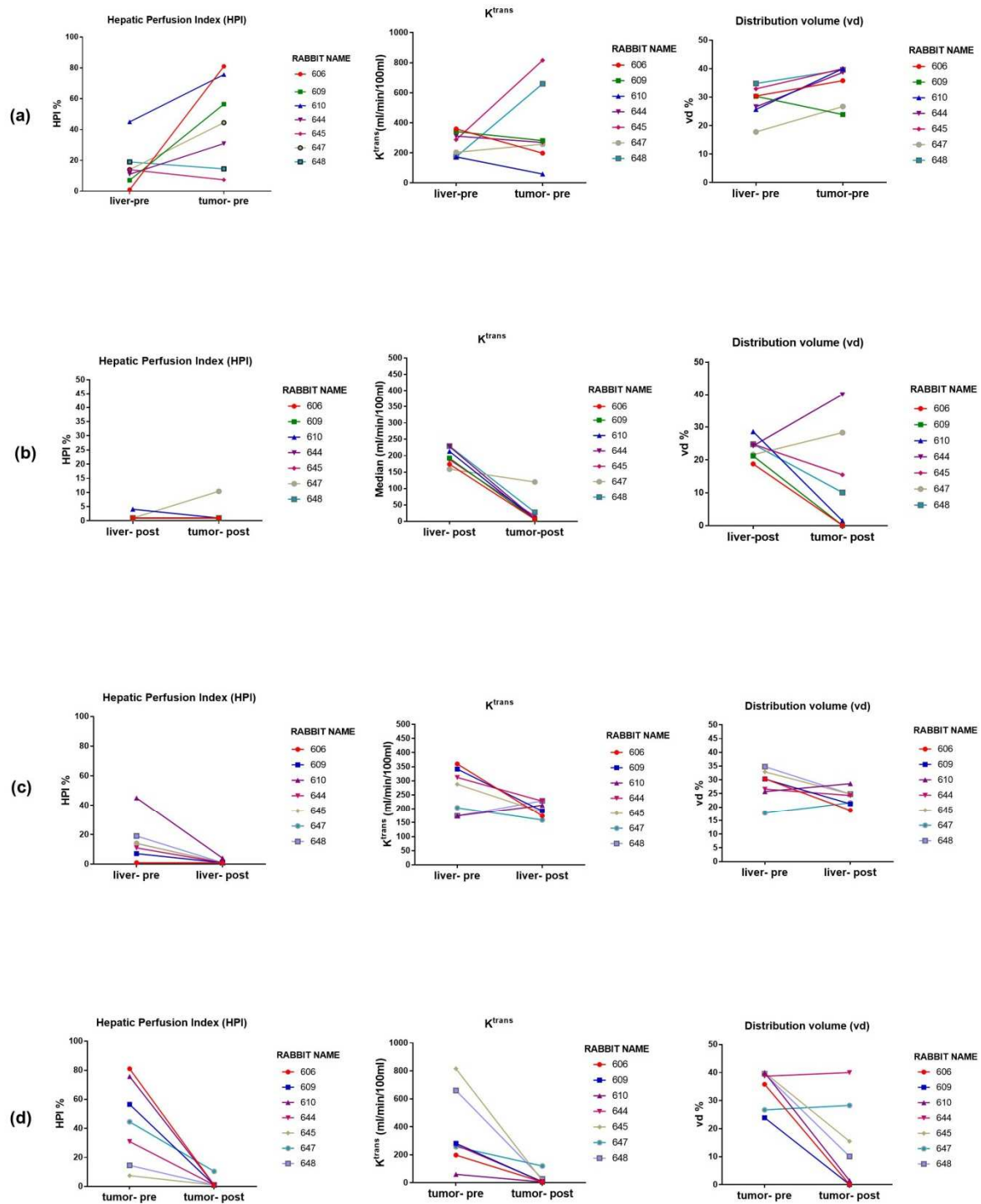


**Figure 61** : Graph of the paired parameter values. a) normal liver and tumor pre-embolization, b) normal liver and tumor post-embolization, c) normal liver pre- and post-embolization, d) tumor pre- and post-embolization.

**Table 9:** Mean paired differences of the parameters and their p-values (comparison in the different combinations displayed in Figure 61) (Wilcoxon matched pairs test).. The asterisk (\*) indicates the statistically significant results ( $p < 0.05$ ), and the cross (+) the quasi-significant results ( $p < 0.1$ ).

		$\Delta$ HPI %	p-value	$\Delta K^{trans}$ ml/min/100ml	p-value	$\Delta$ vd %	p-value
<b>Liver vs Tumor</b> (pre- embolisation)	<b>Mean</b> ( $\pm$ SD)	- 28.5 ( $\pm$ 30.3)	0.078 <sup>+</sup>	-98.6 ( $\pm$ 287.1)	0.94	-6.6 ( $\pm$ 6.7)	0.078 <sup>+</sup>
<b>Liver vs Tumor</b> (post- embolisation)	<b>Mean</b> ( $\pm$ SD)	- 0.9 ( $\pm$ 3.9)	1	170.6 ( $\pm$ 60.9)	0.016 *	9.8 ( $\pm$ 15.6)	0.16
<b>Liver</b> pre-embolisation vs post-embolisation	<b>Mean</b> ( $\pm$ SD)	14.4 ( $\pm$ 13.0)	0.03 *	67.2 ( $\pm$ 90.4)	0.11	4.9 ( $\pm$ 6.4)	0.16
<b>Tumor</b> pre-embolisation vs post-embolisation	<b>Mean</b> ( $\pm$ SD)	42.0 ( $\pm$ 28.8)	0.016 *	336.3 ( $\pm$ 274.5)	0.016 *	21.3 ( $\pm$ 16.4)	0.078 <sup>+</sup>

## Histology

Out of ten embolized VX2 tumors, one rabbit passed away immediately after embolization technique and two rabbits died one-day post-embolization. Seven rabbits, thus, stayed alive one-week post-embolization and therefore underwent histology analysis.

Based on the H&E staining of embolized VX2 tumor one-week post-embolization, the tumor **regression grade was TRG-3** on all specimen, with fibrosis superior to vital tumor cells (Figure 62).

Some sites in the non-tumoral liver were also affected by fibrosis and necrosis (Figure 63), as a consequence of embolic material backflow despite the superselective embolization, and embolization beads were found in these normal liver areas.

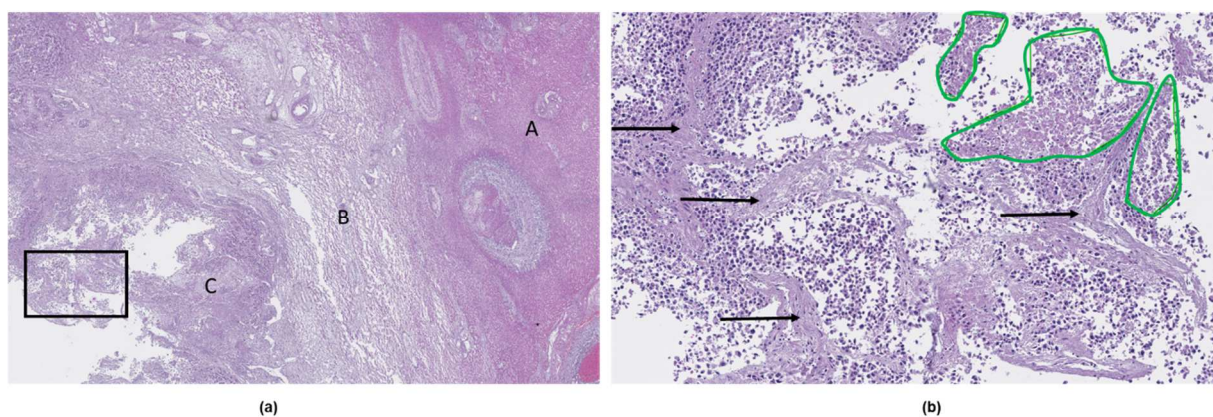


**Figure 62 : One-week post-embolization pathology (H&E staining).** (a) Magnification 2.7x. Three different regions of the post-embolisation sample: normal liver (A), fibrotic band between liver and embolized VX2 tumor (B), embolized VX2 tumor (C). (b) Magnification (11.1x.) of the left black rectangle within the embolized tumor. The embolized tumor contains fibrosis (straight arrows), necrotic cells (green outlines) and vital tumor cells (the small black dots are the nuclei of the vital VX2 cells).

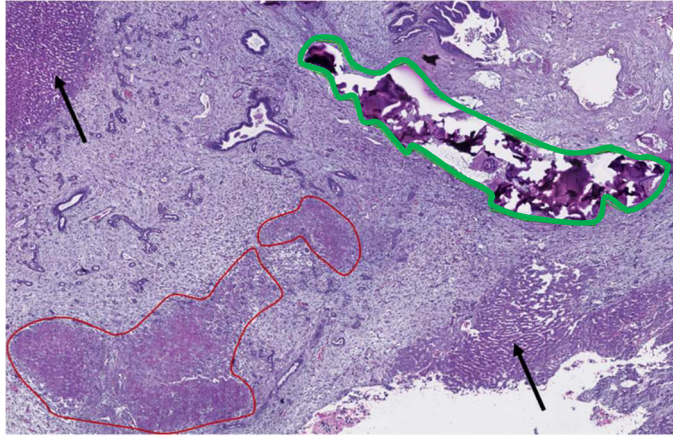


**Figure 63 : One-week post-embolization liver tissue affected by the transcatheter arterial embolisation (TAE) (H&E staining)** Magnification 3.7x. Embolisation product is found into the vessels of the liver (green outline). There are necrotic sites (red outlines) adhered to fibrosis sites (light blue areas). Black arrows indicate the remaining normal liver.

### III.4.4 DISCUSSION

Our aim was to evaluate the in vivo capability of the “DCE-MRI multi-bolus injection scheme” to accurately detect perfusion differences in tissues. Hence, we tested in rabbits bearing VX2 tumor 1) the detection capability of tumors into the liver parenchyma, and 2) the detection capability of the effect of an embolization procedure.

For this purpose, we focused our study on the perfusion difference among the tissues (liver, tumor) pre-embolization and post-embolization based on the values of the perfusion parameters (HPI,  $K^{trans}$ ,  $vd$ ).

Pre-embolization, HPI and  $vd$  indicated both a quasi-significant difference ( $p=0.078$ ) between the normal liver and the tumor, when no difference was for  $K^{trans}$ . Adversely, post-embolisation  $K^{trans}$  presented significant difference ( $p=0.016$ ) between the liver and the tumor in contrast with HPI and  $vd$  parameters (Table 9).

Post-embolization, HPI was extremely low (1.0%) in both tissues with a significant decrease for the tumor ( $p=0.016$ ), and the liver ( $p=0.03$ ).  $K^{trans}$  also significantly decreased ( $p=0.016$ ) for the tumor, when  $vd$  was statistically quasi-significant ( $p=0.078$ ). Contrarily, for the liver, post embolization there was no significant decrease for both  $K^{trans}$  ( $p=0.11$ ) and  $vd$  ( $p=0.16$ ).

The comparison of the parameters before embolization showed that in our series it was possible to detect the tumor in 5 out of 7 cases for HPI and in 6 out of 7 for  $vd$  (Figure 61a).

Tumor is largely supplied by the arterial blood (HPI=50.5 %, as compared to the 14% found in the normal liver in Table 8). Consequently, the embolization procedure that blocked the feeding arterial blood into tumor, affected largely the tumor perfusion. Therefore, for the post-embolization comparisons, the embolization effect in the tumor was detectable using  $K^{trans}$  in all

of the cases of our series (Figure 61b,d). HPI parameter also showed to be a suitable parameter for the evaluation of the embolization effect in the tumor (Figure 61d). Actually, it showed also to be suitable to detect an unexpected effect of the embolization in the liver (Figure 61c) which was confirmed by histology showing that a small amount of the embolic material was found in the normal liver (Figure 63) as a consequence of the backflow of embolic material and leading to a decreased arterial perfusion of the normal liver. In summary,  $K^{\text{trans}}$  and HPI proved to be very sensitive parameters for the tumor embolization evaluation.

On the other hand, although there is a tendency for  $K^{\text{trans}}$  and  $vd$  to decrease, these two parameters were not able to detect efficiently the embolization effect in the liver (Figure 61c). This may be due to the fact that the liver is essentially supplied by the portal vein which was not blocked by the embolization procedure.

### **III.4.5 CONCLUSION**

In this study, we validated the efficiency of our four-bolus injection scheme in vivo to detect tumor tissue within the liver and to evaluate the effect of the embolization procedure. The perfusion parameters obtained with this new injection scheme may be potentially used for the detection of tumor with HPI and  $vd$ , and for the treatment evaluation with HPI and  $K^{\text{trans}}$ .

## IV.GENERAL CONCLUSION & PERSPECTIVES

---

### IV.1 CONCLUSION

The study of the liver perfusion has great interest to detect and characterize hepatic tumors as well as to follow them during treatments. It is, however, very challenging as compared to those of other organs and tissues due to the specific macroscopic and microscopic organization of the liver. This organ not only has a particularly large blood volume with a quasi-absence of interstitial space and very leaky sinusoid capillaries but more importantly, has a double vascular supply (arterial and portal) which induces unusual additional complexities. The study of this double supply, depicted by the ratio of the arterial hepatic perfusion to total hepatic perfusion (HPI-hepatic perfusion index) plays a pivotal role in the assessment of the pathologies of the liver such as cirrhosis (fibrosis) or focal tumor lesions.

Hepatocellular carcinoma (HCC) is known to be preferentially perfused by arterial pedicles, which justifies the therapeutic strategy of arterial embolization. Modifications of HPI, thus, enable to detect HCC at early stages or even at pre-tumoral stages.<sup>74</sup>

The study of HPI with DCE-MRI is challenged by the short delay between the arrival of the contrast agent brought into the liver by arterial blood and the arrival of the contrast agent brought by the portal blood. This induces a very short delay between the rise of the Arterial Input Function (AIF) and the rise of the Portal Input Function (PIF) which has to be recorded by a high temporal resolution imaging system and need to be distinguishable in order to be separated by the deconvolution method. Therefore, signal/noise improvement techniques are needed to be able to extract the perfusion parameters. This can be achieved either by improving dynamic acquisition sequences and the sensitivity of the acquisition equipment such as the antenna, and the quality of the electronic channels or by employing large doses of contrast-agent at high concentration. However, the first strategy is dependent on the available imaging equipment, and the second strategy is limited in DCE-MRI by non-linearity of the relationship between the concentration of contrast-agent and the signal enhancement induced by T1-weighted signal saturation effects, and magnetic susceptibility effects (T2\* effects) due to high concentrations of contrast-agent.

Therefore, we propose an alternative new strategy, which involves an injection of normal dose of contrast-agent but splitting it into multiple boluses (four boluses) and diluting the concentration of contrast-agent for each bolus. The theoretical advantages of this new strategy are to be able to inject a high total dose of contrast-agent in order to obtain a sufficient cumulative signal

increase for the analysis (statistical power) while avoiding the deleterious effects of the high concentrations remaining in the quasi-linear part of the signal enhancement curve. In addition, this strategy seems to be more robust than the conventional injection with a single bolus, because if an unforeseen event (movement) takes place at the time of one of the bolus injections, information enables it to be obtained by the other boluses assuring more reliable results.

In the first part of my thesis, we were able to show that our new strategy provided promising results by significantly increasing the robustness of the results by performing numerical simulations based on experimental input functions (AIF and PIF) where we compared our new multi-bolus technique to a single-bolus injection strategy with the same concentration dilution, which was proposed to limit the effects of signal non-linearity.

In the second part of my thesis, we could verify that the quantitative results obtained with our multi-bolus strategy were sensible enough to differentiate the normal liver from the VX2 tumor in a rabbit. The sensitivity of this strategy permitted also the accurate evaluation of the effect of arterial embolization not only on the embolized tumor but also on the liver that had not been embolized but been affected by the backflow embolization.

## IV.2 PERSPECTIVES

This new injection scheme opens a lot of hope to overcome many of the limitations of DCE-MRI, especially in the liver. Many more studies need to be performed before envisioning its use in everyday clinical practice. These studies will allow the tuning and validation of our strategy. These studies belong to three different areas, which are 1) the technique of injection, 2) the image acquisition, and 3) the image analysis.

- ❖ Among the possible works to optimize the technique of injection, we would like to mention:
    - the test of the strategy in humans in pilot clinical projects,
    - the comparison of our strategy to a single-bolus with the same total dose of that of four boluses.
- More basic scientific works could also be performed including:
- the test of different injection rates, and temporal intervals to improve the robustness of the parameter estimation based on the elimination of mis-sampling of data.
  - the test of different contrast-agent concentrations to achieve the most efficient dose and volume of the bolus, which will provide as little signal saturation and susceptibility effects as possible.

- ❖ The improvement of the image acquisition techniques includes the test of the new rapid-imaging techniques such as partial-random Fourier filling space and spiral MRI filling by using our multi-bolus strategy
- ❖ Finally, the new injection paradigm opens an entirely new field for the data analysis based on statistical data (multiple acquisitions) and quasi-linear signal to concentration relationship.

## V. REFERENCES

---

1. Sibulesky L. Normal liver anatomy. *Clin Liver Dis.* 2013;2(S1):S1-S3. doi:10.1002/cld.124
2. The Radiology Assistant : Anatomy of the liver segments. <http://www.radiologyassistant.nl/en/p4375bb8dc241d/anatomy-of-the-liver-segments.html>. Accessed July 2, 2018.
3. Abdel-Misih SRZ, Bloomston M. Liver Anatomy. *Surg Clin North Am.* 2010;90(4):643-653. doi:10.1016/j.suc.2010.04.017
4. Microscopic Anatomy Of Liver. Anatomy And Physiology Biology Images. <http://stockmarketresources.info/>. Accessed August 23, 2018.
5. SIU SOM Histology GI. <http://www.siumed.edu/~dking2/erg/liver.htm#acini>. Accessed July 2, 2018.
6. Sendensky A., Dufour J.F. Liver Physiology. Springer. <https://www.printfriendly.com/p/g/iZHaBZ>. Published 2011. Accessed July 16, 2018.
7. The Liver | Boundless Anatomy and Physiology. <https://courses.lumenlearning.com/boundless-ap/chapter/the-liver/>. Accessed July 16, 2018.
8. Charlton MR. Protein metabolism and liver disease. *Baillieres Clin Endocrinol Metab.* 1996;10(4):617-635.
9. Transamination and Deamination of amino acids. *Med Biochem.* February 2018. <http://www.medbiochemistry.com/metabolism-of-amino-acids/>. Accessed July 19, 2018.
10. Metabolic Functions of the Liver. <http://www.vivo.colostate.edu/hbooks/pathphys/digestion/liver/metabolic.html>. Accessed July 17, 2018.
11. How the Liver Detoxifies | Life Extension. LifeExtension.com. <http://www.lifeextension.com/Protocols/Gastrointestinal/Liver-Degenerative-Disease/Page-04>. Accessed July 19, 2018.
12. Rothbarth J, van de Velde CJH. Treatment of liver metastases of colorectal cancer. *Ann Oncol Off J Eur Soc Med Oncol.* 2005;16 Suppl 2:ii144-149. doi:10.1093/annonc/mdi702
13. Hepatocellular Carcinoma | NEJM. New England Journal of Medicine. <https://www.nejm.org/doi/10.1056/NEJMra1001683>. Accessed March 25, 2019.
14. Forner A, Llovet JM, Bruix J. Hepatocellular carcinoma. *The Lancet.* 2012;379(9822):1245-1255. doi:10.1016/S0140-6736(11)61347-0
15. Izzo F, Piccirillo M, Albino V, et al. Prospective screening increases the detection of potentially curable hepatocellular carcinoma: results in 8,900 high-risk patients. *HPB.* 2013;15(12):985-990. doi:10.1111/hpb.12080
16. Ando E, Kuromatsu R, Tanaka M, et al. Surveillance program for early detection of hepatocellular carcinoma in Japan: results of specialized department of liver disease. *J Clin Gastroenterol.* 2006;40(10):942-948. doi:10.1097/O1.mcg.0000225675.14594.d6

17. Lu S-N, Wang J-H, Chen P-F, et al. Community-based mass ultrasonographic screening of hepatocellular carcinoma among thrombocytopenic adults. *Cancer Epidemiol Biomark Prev Publ Am Assoc Cancer Res Cosponsored Am Soc Prev Oncol*. 2008;17(7):1813-1821. doi:10.1158/1055-9965.EPI-07-2746
18. Singal A, Volk ML, Waljee A, et al. Meta-analysis: surveillance with ultrasound for early-stage hepatocellular carcinoma in patients with cirrhosis. *Aliment Pharmacol Ther*. 2009;30(1):37-47. doi:10.1111/j.1365-2036.2009.04014.x
19. Kansagara D, Papak J, Pasha AS, et al. Screening for hepatocellular carcinoma in chronic liver disease: a systematic review. *Ann Intern Med*. 2014;161(4):261-269. doi:10.7326/M14-0558
20. Bruix J, Reig M, Sherman M. Evidence-Based Diagnosis, Staging, and Treatment of Patients With Hepatocellular Carcinoma. *Gastroenterology*. 2016;150(4):835-853. doi:10.1053/j.gastro.2015.12.041
21. Oka H, Saito A, Ito K, et al. Multicenter prospective analysis of newly diagnosed hepatocellular carcinoma with respect to the percentage of Lens culinaris agglutinin-reactive alpha-fetoprotein. *J Gastroenterol Hepatol*. 2001;16(12):1378-1383.
22. Sterling RK, Jeffers L, Gordon F, et al. Utility of Lens culinaris agglutinin-reactive fraction of alpha-fetoprotein and des-gamma-carboxy prothrombin, alone or in combination, as biomarkers for hepatocellular carcinoma. *Clin Gastroenterol Hepatol Off Clin Pract J Am Gastroenterol Assoc*. 2009;7(1):104-113. doi:10.1016/j.cgh.2008.08.041
23. Singal AG, Conjeevaram HS, Volk ML, et al. Effectiveness of hepatocellular carcinoma surveillance in patients with cirrhosis. *Cancer Epidemiol Biomark Prev Publ Am Assoc Cancer Res Cosponsored Am Soc Prev Oncol*. 2012;21(5):793-799. doi:10.1158/1055-9965.EPI-11-1005
24. Pocha C, Dieperink E, McMaken KA, Knott A, Thurs P, Ho SB. Surveillance for hepatocellular cancer with ultrasonography vs. computed tomography -- a randomised study. *Aliment Pharmacol Ther*. 2013;38(3):303-312. doi:10.1111/apt.12370
25. Trinchet J-C, Chaffaut C, Bourcier V, et al. Ultrasonographic surveillance of hepatocellular carcinoma in cirrhosis: A randomized trial comparing 3- and 6-month periodicities. *Hepatology*. 2011;54(6):1987-1997. doi:10.1002/hep.24545
26. Santi V, Trevisani F, Gramenzi A, et al. Semiannual surveillance is superior to annual surveillance for the detection of early hepatocellular carcinoma and patient survival. *J Hepatol*. 2010;53(2):291-297. doi:10.1016/j.jhep.2010.03.010
27. Han K-H, Kim DY, Park JY, et al. Survival of hepatocellular carcinoma patients may be improved in surveillance interval not more than 6 months compared with more than 6 months: a 15-year prospective study. *J Clin Gastroenterol*. 2013;47(6):538-544. doi:10.1097/MCG.0b013e3182755c13
28. European Association for the Study of the Liver. Electronic address: easloffice@easloffice.eu, European Association for the Study of the Liver. EASL Clinical Practice Guidelines: Management of hepatocellular carcinoma. *J Hepatol*. 2018;69(1):182-236. doi:10.1016/j.jhep.2018.03.019

29. Marrero JA, Kulik LM, Sirlin CB, et al. Diagnosis, Staging, and Management of Hepatocellular Carcinoma: 2018 Practice Guidance by the American Association for the Study of Liver Diseases. *Hepatol Baltim Md.* 2018;68(2):723-750. doi:10.1002/hep.29913
30. Chernyak V, Fowler KJ, Kamaya A, et al. Liver Imaging Reporting and Data System (LI-RADS) Version 2018: Imaging of Hepatocellular Carcinoma in At-Risk Patients. *Radiology.* 2018;289(3):816-830. doi:10.1148/radiol.2018181494
31. Forner A, Reig ME, de Lope CR, Bruix J. Current strategy for staging and treatment: the BCLC update and future prospects. *Semin Liver Dis.* 2010;30(1):61-74. doi:10.1055/s-0030-1247133
32. Llovet JM, Brú C, Bruix J. Prognosis of hepatocellular carcinoma: the BCLC staging classification. *Semin Liver Dis.* 1999;19(3):329-338. doi:10.1055/s-2007-1007122
33. Llovet JM, Bustamante J, Castells A, et al. Natural history of untreated nonsurgical hepatocellular carcinoma: rationale for the design and evaluation of therapeutic trials. *Hepatol Baltim Md.* 1999;29(1):62-67. doi:10.1002/hep.510290145
34. Romagnoli R, Mazzaferro V, Bruix J. Surgical resection for hepatocellular carcinoma: Moving from what can be done to what is worth doing. *Hepatol Baltim Md.* 2015;62(2):340-342. doi:10.1002/hep.27831
35. Reig M, Darnell A, Forner A, Rimola J, Ayuso C, Bruix J. Systemic therapy for hepatocellular carcinoma: the issue of treatment stage migration and registration of progression using the BCLC-refined RECIST. *Semin Liver Dis.* 2014;34(4):444-455. doi:10.1055/s-0034-1394143
36. Esnaola NF, Lauwers GY, Mirza NQ, et al. Predictors of microvascular invasion in patients with hepatocellular carcinoma who are candidates for orthotopic liver transplantation. *J Gastrointest Surg Off J Soc Surg Aliment Tract.* 2002;6(2):224-232; discussion 232.
37. Wald C, Russo MW, Heimbach JK, Hussain HK, Pomfret EA, Bruix J. New OPTN/UNOS policy for liver transplant allocation: standardization of liver imaging, diagnosis, classification, and reporting of hepatocellular carcinoma. *Radiology.* 2013;266(2):376-382. doi:10.1148/radiol.12121698
38. Livraghi T, Meloni F, Di Stasi M, et al. Sustained complete response and complications rates after radiofrequency ablation of very early hepatocellular carcinoma in cirrhosis: Is resection still the treatment of choice? *Hepatol Baltim Md.* 2008;47(1):82-89. doi:10.1002/hep.21933
39. Roayaie S, Obeidat K, Sposito C, et al. Resection of hepatocellular cancer  $\leq 2$  cm: results from two Western centers. *Hepatol Baltim Md.* 2013;57(4):1426-1435. doi:10.1002/hep.25832
40. Mazzaferro V, Bhoori S, Sposito C, et al. Milan criteria in liver transplantation for hepatocellular carcinoma: an evidence-based analysis of 15 years of experience. *Liver Transplant Off Publ Am Assoc Study Liver Dis Int Liver Transplant Soc.* 2011;17 Suppl 2:S44-57. doi:10.1002/lt.22365
41. Bruix J, Sala M, Llovet JM. Chemoembolization for hepatocellular carcinoma. *Gastroenterology.* 2004;127(5 Suppl 1):S179-188.

42. Llovet JM, Real MI, Montaña X, et al. Arterial embolisation or chemoembolisation versus symptomatic treatment in patients with unresectable hepatocellular carcinoma: a randomised controlled trial. *The Lancet*. 2002;359(9319):1734-1739. doi:10.1016/S0140-6736(02)08649-X
43. Lo C-M, Ngan H, Tso W-K, et al. Randomized controlled trial of transarterial lipiodol chemoembolization for unresectable hepatocellular carcinoma. *Hepatology*. 2002;35(5):1164-1171. doi:10.1053/jhep.2002.33156
44. Llovet JM, Bruix J. Systematic review of randomized trials for unresectable hepatocellular carcinoma: Chemoembolization improves survival. *Hepatology*. 2003;37(2):429-442. doi:10.1053/jhep.2003.50047
45. Bruix J, Sherman M. Management of hepatocellular carcinoma: An update. *Hepatology*. 2011;53(3):1020-1022. doi:10.1002/hep.24199
46. European Association For The Study Of The Liver, European Organisation For Research And Treatment Of Cancer. EASL-EORTC clinical practice guidelines: management of hepatocellular carcinoma. *J Hepatol*. 2012;56(4):908-943. doi:10.1016/j.jhep.2011.12.001
47. Verslype C, Rosmorduc O, Rougier P, ESMO Guidelines Working Group. Hepatocellular carcinoma: ESMO-ESDO Clinical Practice Guidelines for diagnosis, treatment and follow-up. *Ann Oncol Off J Eur Soc Med Oncol*. 2012;23 Suppl 7:vii41-48. doi:10.1093/annonc/mds225
48. Varela M, Real MI, Burrel M, et al. Chemoembolization of hepatocellular carcinoma with drug eluting beads: efficacy and doxorubicin pharmacokinetics. *J Hepatol*. 2007;46(3):474-481. doi:10.1016/j.jhep.2006.10.020
49. Wilhelm S, Carter C, Lynch M, et al. Discovery and development of sorafenib: a multikinase inhibitor for treating cancer. *Nat Rev Drug Discov*. 2006;5(10):835-844. doi:10.1038/nrd2130
50. Reig M, Rimola J, Torres F, et al. Postprogression survival of patients with advanced hepatocellular carcinoma: rationale for second-line trial design. *Hepatology*. 2013;58(6):2023-2031. doi:10.1002/hep.26586
51. Forner A, Gilibert M, Bruix J, Raoul J-L. Treatment of intermediate-stage hepatocellular carcinoma. *Nat Rev Clin Oncol*. 2014;11(9):525-535. doi:10.1038/nrclinonc.2014.122
52. Reig M, Torres F, Rodriguez-Lopez C, et al. Early dermatologic adverse events predict better outcome in HCC patients treated with sorafenib. *J Hepatol*. 2014;61(2):318-324. doi:10.1016/j.jhep.2014.03.030
53. Cabibbo G, Enea M, Attanasio M, Bruix J, Craxì A, Cammà C. A meta-analysis of survival rates of untreated patients in randomized clinical trials of hepatocellular carcinoma. *Hepatology*. 2010;51(4):1274-1283. doi:10.1002/hep.23485
54. Allen.D. Elster. Perfusion: defined. Questions and Answers in MRI. <http://mriquestions.com/measuring-perfusion.html>. Accessed August 23, 2018.
55. Cuenod CA, Balvay D. Perfusion and vascular permeability: Basic concepts and measurement in DCE-CT and DCE-MRI. *Diagn Interv Imaging*. 2013;94(12):1187-1204. doi:10.1016/j.diii.2013.10.010

56. Steven SOURBRON. Classic models for dynamic contrast-enhanced MRI. - PubMed - NCBI. [https://www.ncbi.nlm.nih.gov-s.frodon-biusante.parisdescartes.fr/pubmed?term=\(classic%20models%20for%20dynamic%20contrast%20enhanced%20MRI\)%20AND%20Sourbron%2C%20Steven%5BAuthor%5D](https://www.ncbi.nlm.nih.gov-s.frodon-biusante.parisdescartes.fr/pubmed?term=(classic%20models%20for%20dynamic%20contrast%20enhanced%20MRI)%20AND%20Sourbron%2C%20Steven%5BAuthor%5D). Published 2012. Accessed July 4, 2017.
57. Le Bihan D. Theoretical principles of perfusion imaging. Application to magnetic resonance imaging. *Invest Radiol.* 1992;27 Suppl 2:S6-11.
58. Jahng G-H, Li K-L, Ostergaard L, Calamante F. Perfusion Magnetic Resonance Imaging: A Comprehensive Update on Principles and Techniques. *Korean J Radiol.* 2014;15(5):554. doi:10.3348/kjr.2014.15.5.554
59. Tofts PS. T1-weighted DCE imaging concepts: modelling, acquisition and analysis. *signal.* 2010;500(450):400.
60. Tofts PS, Brix G, Buckley DL, et al. Estimating kinetic parameters from dynamic contrast-enhanced T(1)-weighted MRI of a diffusable tracer: standardized quantities and symbols. *J Magn Reson Imaging JMRI.* 1999;10(3):223-232.
61. de Bazelaire C, Calmon R, Thomassin I, et al. Accuracy of perfusion MRI with high spatial but low temporal resolution to assess invasive breast cancer response to neoadjuvant chemotherapy: a retrospective study. *BMC Cancer.* 2011;11:361. doi:10.1186/1471-2407-11-361
62. Choon Hua Thng. Perfusion magnetic resonance imaging of the liver. - PubMed - NCBI. <https://www.ncbi.nlm.nih.gov-s.frodon-biusante.parisdescartes.fr/pubmed/20355238>. Published 2010. Accessed July 4, 2017.
63. Pandharipande PV, Krinsky GA, Rusinek H, Lee VS. Perfusion imaging of the liver: current challenges and future goals. *Radiology.* 2005;234(3):661-673. doi:10.1148/radiol.2343031362
64. Miles KA, Hayball MP, Dixon AK. Functional images of hepatic perfusion obtained with dynamic CT. *Radiology.* 1993;188(2):405-411. doi:10.1148/radiology.188.2.8327686
65. Blomley MJ, Coulden R, Dawson P, et al. Liver perfusion studied with ultrafast CT. *J Comput Assist Tomogr.* 1995;19(3):424-433.
66. Materne R, Smith A m., Peeters F, et al. Assessment of hepatic perfusion parameters with dynamic MRI. *Magn Reson Med.* 2002;47(1):135-142. doi:10.1002/mrm.10045
67. Rabbits. American Anti-Vivisection Society. <https://aavs.org/animals-science/animals-used/rabbits/>. Accessed June 18, 2019.
68. Anesthesia Protocols for Rabbits | House Rabbit Society. <https://rabbit.org/anesthesia-protocols-for-rabbits/>. Accessed June 18, 2019.
69. KIDD, ROUS. A TRANSPLANTABLE RABBIT CARCINOMA ORIGINATING IN A VIRUS-INDUCED PAPILOMA AND CONTAINING THE VIRUS IN MASKED OR ALTERED FORM. - PubMed - NCBI. <https://www.ncbi.nlm.nih.gov/pubmed/19871000>. Published 1940. Accessed July 13, 2017.

70. Rous P, Beard JW. THE PROGRESSION TO CARCINOMA OF VIRUS-INDUCED RABBIT PAPILLOMAS (SHOPE). *J Exp Med*. 1935;62(4):523-548. doi:10.1084/jem.62.4.523
71. Lee K-H, Liapi E, Buijs M, et al. Considerations for implantation site of VX2 carcinoma into rabbit liver. *J Vasc Interv Radiol JVIR*. 2009;20(1):113-117. doi:10.1016/j.jvir.2008.09.033
72. Rao PP, Pascale F, Seck A, et al. Irinotecan loaded in eluting beads: preclinical assessment in a rabbit VX2 liver tumor model. *Cardiovasc Intervent Radiol*. 2012;35(6):1448-1459. doi:10.1007/s00270-012-0343-y
73. Mandard AM, Dalibard F, Mandard JC, et al. Pathologic assessment of tumor regression after preoperative chemoradiotherapy of esophageal carcinoma. Clinicopathologic correlations. *Cancer*. 1994;73(11):2680-2686. doi:10.1002/1097-0142(19940601)73:11<2680::aid-cnrcr2820731105>3.0.co;2-c
74. Fournier L, Cuenod C, de Bazelaire C, et al. *Early Modifications of Hepatic Perfusion Measured by Functional CT in a Rat Model of Hepatocellular Carcinoma Using a Blood Pool Contrast Agent*. Vol 14.; 2004. doi:10.1007/s00330-004-2339-8

---

## **PAPER I: Multi-Bolus Injection to Improve the Robustness of Liver DCE-MRI: A Simulation Study in Rabbits**

---

# Multi-bolus injection to improve the robustness of Liver DCE-MRI: *a simulation study in rabbits*

Sofia Veneti, MD<sup>1,2</sup>, Daniel Balvay, PhD<sup>1,2,3</sup>, Gwennh ael Autret, PhD<sup>1,2,3</sup>, Charles A. Cuenod, PhD<sup>1,2,4</sup>

<sup>1</sup>Paris Cardiovascular Research Center (PARCC), INSERM U970 Paris, France,

<sup>2</sup>Universit  de Paris, Paris, France,

<sup>3</sup>Plateforme d'Imagerie du Vivant de Paris Descartes, Paris, France,

<sup>4</sup>Radiologie, H pital Europ en G. Pompidou (HEGP) APHP, Paris, France

## ABSTRACT

**Purpose:** Quantitative liver Dynamic Contrast Enhanced (DCE)-MRI is challenging, due to the dual vascular hepatic supply. We propose a multi-bolus injection scheme to overcome most of the limitations induced by a single bolus injection. We tested the improvement carried out by this strategy on realistic simulations in rabbit liver.

**Methods:** A computer simulation was developed using real arterial input function (AIF) and portal input function (PIF) obtained on rabbit on a 4.7T MRI scanner with single- and multi bolus injection schemes. One thousand liver enhancement curves were simulated with a dual-input model by varying the perfusion parameter values (Hepatic Perfusion Indexes -HPI, total hepatic blood flow -Ft, and distribution volume fractions -vd). Noise has been added to these simulated curves. Then, a deconvolution was applied to these simulated curves to estimate the perfusion parameters. Finally, the estimated and the initial parameters were compared and evaluated by the Coefficient of Variation (CV) of their differences to test the robustness of the measurements.

**Results:** For the multi-bolus scheme, CVs were 31.1%, 12.5%, and 5.2% in the single-bolus injection for HPI, Ft, and vd, respectively. The improvement factors in the 4-bolus injection were 47.9% ( $P < 2 \times 10^{-5}$ ), 35.7% ( $P < 2 \times 10^{-5}$ ), and 65.9% ( $P < 2 \times 10^{-5}$ ). Results obtained by the single-bolus scheme up to 10min degraded the HPI robustness and slightly improved the Ft, and vd.

## Conclusion:

Performing a low concentration multi-bolus scheme, liver DCE-MRI robustness is substantially improved minimizing the non-linearity effect. The improvement is especially sensitive for HPI, which is a critical perfusion parameter in the liver.

## 1. INTRODUCTION

Nowadays, the most developed functional imaging technique for the evaluation of tissue microcirculation, beyond the brain, is Dynamic Contrast Enhanced imaging (DCE-imaging). This implies a sequential image acquisition during the venous injection of a contrast agent (CA) and may be performed with magnetic resonance imaging (DCE-MRI), computed tomography (DCE-CT) or ultrasound (DCE-US). Under strict conditions, DCE-imaging allows the quantitative estimation of the perfusion parameters of normal and diseased tissues, by analyzing the tissue enhancement curves in response to the inflow of CA -called arterial input function (AIF)- by using pharmacokinetic models.

MRI is the modality of choice for liver imaging due to its superior contrast resolution and its multiparametric capabilities. DCE-MRI of the liver has great potential for the evaluation of focal tumors and diffuse liver disease in addition to diffusion-, T2\* sequences and "in phase out of phase acquisition." However, several challenges remain when applying quantitative DCE-MRI in clinical routine <sup>1,2</sup>.

One of these challenges for quantitative DCE-MRI of the liver is the dual hepatic perfusion. The usual models, with a single Arterial Input Function (AIF), are not relevant for the liver, because the portal venous inflow needs to be considered. Therefore, dual-input models should be applied, including the Portal Input Function (PIF) in addition to the AIF<sup>3-6</sup>. Dual-input models, however, induce more complexity. These models require a clear difference between the AIF- and PIF- curve shapes to separate their contributions. This point is demanding, as the circulation of blood between the aorta and the portal vein leads quickly to the CA enhancement curves of AIF and PIF to the same equilibrium level. Hence, CA has to be injected fast to generate sharp transient patterns, which could differentiate PIF and AIF. To bring out these patterns, high temporal resolution is required for the dynamic image acquisition. This is especially challenging when performing DCE-MRI, due to the relatively low temporal resolution of most DCE-MRI sequences.

A second challenge, which can be generalized to all DCE-MRI acquisition, is to generate high signal to noise ratio (SNR). Currently, high SNR is obtained by injecting high CA doses. However, in MRI, this way of improving SNR has a major drawback, due to MR signal saturation effects and T2\* effects caused by high CA concentrations.

These effects result in underestimation of CA concentration, especially in the vessels during the first pass peak, when CA reaches maximal concentration and therefore yields major quantification errors.

The combination of the previously described requirements: signal sharpness and high SNR, is a challenge in liver DCE-MRI. To address these requirements, we propose a multi-bolus injection approach, with the repetition of four short boluses of diluted CA. This approach enables 1) fast-rate injections, for the fulfillment of the signal sharpness requirement, with high SNR, 2) substantially reduced systematic error, as a result of the low CA concentration of each bolus. Moreover, this strategy should be less sensitive to random and unexpected periods of motion that could happen during a single bolus injection.

The aim of this study was to test if the multi-bolus injection strategy could improve the measurement of hepatic perfusion parameters by enhancing the SNR when preventing systematic error. The robustness of the estimation of the perfusion parameters was evaluated for a single- and a multi-bolus injection strategy on simulated data generated from real AIF and PIF obtained in rabbits with a dual-input single compartment pharmacokinetic model.

## 2. THEORY

### Pharmacokinetic liver model

Compartment models are used to describe the kinetic behavior of the contrast agent (CA) in the tissues. In our study, we estimate the liver perfusion parameter with a dual-input single-compartment model<sup>3-9</sup>, as illustrated in Figure 1. The model's equation, Figure 1, is based on the following assumptions:

1. Contrast agent concentration in the hepatic artery ( $C_A$ ) flows into the liver via the hepatic artery at a perfusion rate  $F_A/v_d$ , where  $F_A$  is the amount of contrast agent in the hepatic artery that enters into a unit of volume of liver per second (ml/sec), and  $v_d$  is the fraction of the liver where the contrast agent is distributed.
2. Contrast agent concentration in the portal vein ( $C_p$ ) flows via the portal vein at a perfusion rate of  $F_p/v_d$ , where  $F_p$  is the amount of contrast agent in the portal vein that enters into a unit of volume of liver per second (ml/sec), and  $v_d$  is the fraction of the liver where the contrast agent is distributed.
3. The vascular space and the interstitial space were considered a single functional compartment in the normal liver. As a result, the contrast agent of two blood supplies (portal vein, hepatic artery) is assumed to be instantaneously distributed from the vasculature into the small interstitial space of Disse through the fenestrated sinusoid wall.
4. The apparent concentration in the liver region of interest (ROI) is the amount of CA in the liver divided by the total tissue region.

The mathematical equation<sup>10</sup> which describes the kinetic behavior of the CA in the liver region of interest is given by:

$$\frac{dC_L}{dt} = \frac{F_A}{v_d} C_A(t) + \frac{F_p}{v_d} C_p(t) - \frac{F_t}{v_d} C_L(t) \quad (1)$$

where,  $F_t = F_A + F_p$  is the outflow through the liver region.

The inflow equals the outflow and is expressed as ml/min/100ml.

The arterial fraction of hepatic blood flow (HPI) (%) is calculated as  $(F_A/F_t)*100$  and represents the relative contribution of the arterial blood supply to the total blood supply to the liver parenchyma. HPI is a major liver perfusion parameter since it is very sensitive to the liver pathologies <sup>4,5,11-15</sup>.

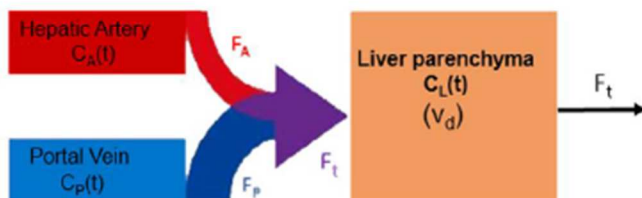


**Figure 1:** Dual Input single-compartment model.  $C_L(t)$ ,  $C_A(t)$  and  $C_P(t)$  are the concentrations of the CA at time  $t$  in the liver region of interest (ROI),  $F_A$  and  $F_P$ , are the blood flows from the hepatic artery, and the portal vein, respectively yielding the total hepatic blood to the liver ( $F_t$ ).  $v_d$  is the fraction of the liver volume where the contrast agent is distributed between the vascular and the interstitial spaces. The same amount of total hepatic blood flow enters and goes out of the liver ( $F_t$ ).

### 3. MATERIALS AND METHODS

In order to investigate if the multi-bolus scheme provides more robust perfusion parameters than the usual single-bolus scheme we employed a simulation technique. First, we generated various liver enhancement curves with different sets of perfusion parameters and applied real AIF and PIF obtained in vivo with a single bolus or a multi-bolus injection. Next, we extracted back estimated parameters that we compared to the input parameters in order to evaluate the improvement of robustness provided by the multi-bolus versus the single-bolus strategy.

## A. In-Vivo Acquisition Procedure

To generate reasonable liver enhancement curves, we employed real arterial and portal input functions extracted from in-vivo liver DCE-MRI experiments in rabbits.

### 1. Rabbits

DCE-MRI sequences were performed on healthy rabbits according to the guidelines of the French rural and maritime code (R. 214-87 to R. 214-126) and the study was approved by the ethics committee of our institution.

Three female New Zealand white rabbits (N=, 3.0-3.5kg) with normal liver function were used for the experiments and anaesthetized with Zoletil/Xylazine cocktail (Vibrac, Zoletil 100: 8mg/kg; Rompun, 5mg/kg) delivered intramuscularly after a 17-hr fast. Throughout the MRI experiment, the rabbit anesthesia was being maintained by mechanical ventilation via an alternative endotracheal mask (v-gel, Docsinnovent) with a mixture of air, O<sub>2</sub> and, isoflurane at 45%, 55%, and 0.6%-1.5%, respectively.

### 2. MRI Examination

MRI performed on a 4.7T scanner dedicated to small animals (Bruker Biospec) using the dedicated rabbit gradient coil. The rabbits were positioned prone, with the lower limbs fully extended and the image center positioned between the heart and the liver. Anatomic and dynamic images were acquired in coronal and axial planes.

#### Anatomical images

T1-weighted spin echo RARE (2D) with coronal slice orientation was acquired over the heart and the liver with the following imaging parameters: TR/TE= 975.9/12.6ms, slice thickness= 3mm, Field of View (FOV)= 15 x 15 cm<sup>2</sup>, Matrix= 256 x 256 pixels<sup>2</sup>, number of slices= 15, spatial resolution= 58.6 mm/pixel, as well as T2-weighted turbo spin echo turboRARE (2D) with axial slice orientation acquired over the liver with imaging parameters: TR/TE= 2437/50 ms, slice thickness= 2mm, Field of View= 15 x 15 cm<sup>2</sup>, Matrix= 256 x 256 pixels<sup>2</sup>, number of slices= 21, spatial resolution= 58.6 mm/pixel. Both T1-weighted and T2-weighted sequences were performed for the

localization of the abdominal aorta, the portal vein and the liver. Both acquired with respiratory gating.

### **DCE images**

Liver perfusion was assessed with a dynamic T1-weighted gradient echo sequence (FLASH 2D) (DCE sequences) with coronal slice orientation over the abdominal aorta, the portal vein and the liver parenchyma. Imaging parameters were the following: TR/TE= 24/3 ms, temporal resolution= 2s 37ms/image, flip angle= 70°, number of slices= 3, slice thickness=3mm, acquisition time= 10min for a total of 253 time frames. Gd-DOTA (gadoterate dimeglumine, Dotarem®, Guerbet, Roissy, France) injected as a dose of 0.1mmol/kg body (0.2ml/kg). It also is a blood-pool agent with renal clearance and moderate relaxivity (3.3 sec<sup>-1</sup> mM<sup>-1</sup> in plasma at 4.7T and 37°C)<sup>16</sup>. Calibrated boluses of Gd-DOTA were intravenously injected into the ear vein at a rate of 3mL/s via an MR-compatible power injector (Optistar, Elite; Guerbet, France).

### **Bolus Schemes**

DCE acquisition was acquired with two different bolus-injection schemes: 1) a single-bolus injection scheme, and 2) a multi-bolus injection scheme with four boluses. For both injection-schemes, the total DCE-MRI acquisition duration was 10min. The first bolus-injection for both injection-schemes was administered 1 min after the beginning of the MR acquisition (t1=1min) to generate a baseline prior to injection. The multi-bolus scheme consisted of four boluses in total, the three additional boluses administered at 2-minute intervals (t2=3min, t3=5min, t4=7min). The volume of each single injection bolus for both protocols was 4ml of Gd-DOTA with a dilution 1:25 (corresponding to 1/4 of the total clinical dose for each bolus). This low concentration (diluted Gd-DOTA) was selected to reduce the saturation and T2\* effects in order to minimize the underestimation of the concentration of the contrast agent<sup>3</sup>. Both imaging protocols were performed with the same MR parameters. Each rabbit was successively imaged with both injection schemes, with a one-week interval between

the two imaging sessions, to allow contrast agent clearance and anesthesia recovery. The bolus-injection schemes are shown in Figure 2.

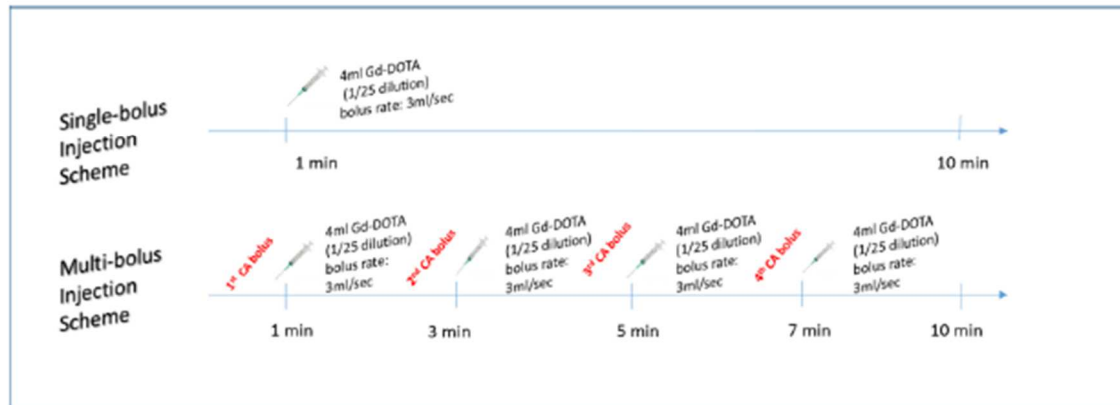
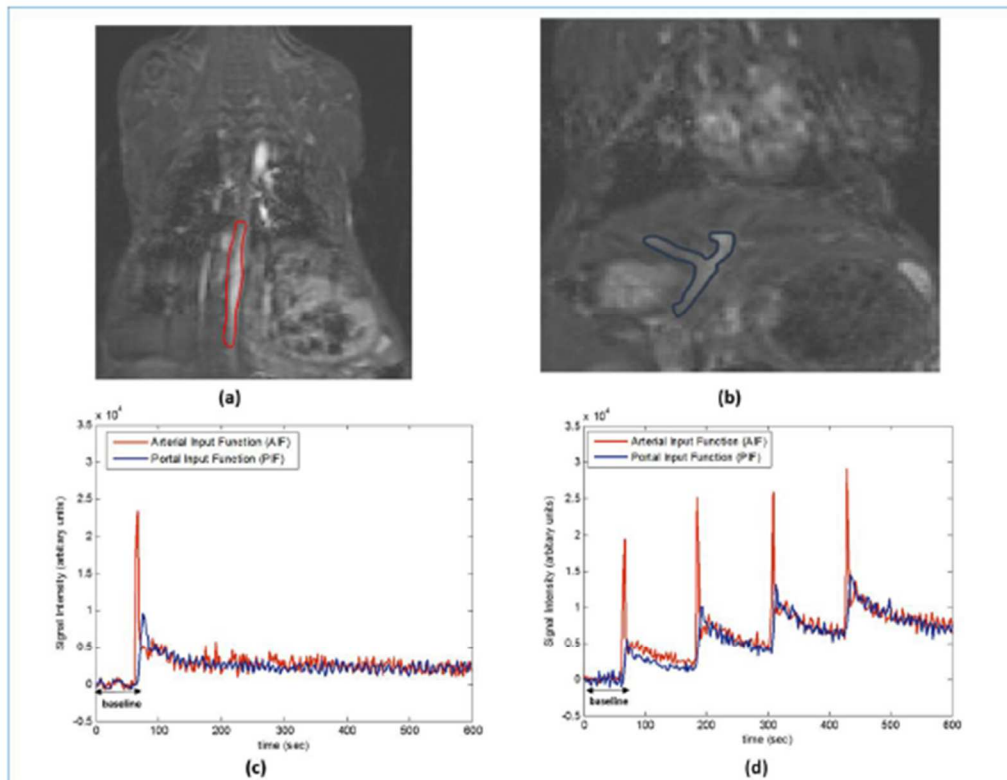


Figure 2: Two different experimental bolus-injection schemes.

### 3. Extraction of the aorta and portal vein enhancement curves

To extract the dynamic enhancement curves of the abdominal aorta and portal vein, the sets of DCE-MR Images were transferred to in-house software, *PhysioD3D*, developed in Matlab (R2013b; MathWorks, Natick, MA)<sup>17-19</sup>. Regions of interest (ROI) were manually drawn over the abdominal aorta (as a surrogate of the hepatic artery) and the portal vein, on one frame, showing the arrival of the contrast agent. Those ROIs were propagated on every time frame. The signal intensity of the ROIs over time measured as arbitrary units. The enhancement curves were calculated by subtracting the mean MR signal before the injections (baseline) from the MR signal after the injections (S-S<sub>0</sub>). Figure 3 shows the ROIs drawn on the aorta and the portal vein of one rabbit and the signal enhancement curves over time obtained with the two different injection schemes.



**Figure 3:** (a-b) Coronal abdominal slices of a rabbit selected from the DCE series after intravenous bolus administration of 0.1 mmol/kg Gd-DOTA (1:25 dilution). (a) Slice containing the abdominal aorta (red ROI). (b) Slice containing the portal vein (dark blue ROI). (c-d) Signal enhancement curves over time for the ROIs on the abdominal aorta, and the portal vein (c) Single-bolus injection scheme. (d) Multi-bolus injection scheme.

#### 4. Input functions (AIF, PIF) selection

In order to compare single and multi-bolus, input functions were selected taking into account the following criteria: (1) comparable signals in portal and arterial bloods during the late equilibrium phase, as expected by the theory (2) comparable signal enhancement curves between single and multi-bolus schemes before the second bolus injection of the multi-bolus scheme, (3) single and multi-bolus enhancement curves selected from the same rabbit, and (4) motion artifacts limited as much as possible, specifically in the PIF enhancement curve.

## B. Computer simulation of liver enhancing curves and parameter retrieval.

The general process that we use to test the bolus injection strategies was to 1) generate synthetic liver enhancement curves by imposing liver perfusion parameters [initial parameters], 2) estimate back the perfusion parameters [estimated parameters], 3) and finally compare the estimated with the initial parameters. The workflow of this process is illustrated in Figure 4.

### 1. Synthetic generation of liver enhancement curves – Convolution

A computer simulation generated synthetic liver enhancement curves applying the perfusion model described in the theory section, to (1) a set of experimental enhancement curves measured in the abdominal aorta and the portal vein for both bolus-injection schemes coming from the same rabbit as input functions (AIF and PIF) selected as mentioned above (fig 3 c and d); and (2) a large variety of values of liver perfusion parameters, randomly chosen, for Hepatic Perfusion Index (HPI), total liver perfusion ( $F_t$ ), and distribution volume fraction ( $v_d$ ). The ranges of values for these "initial parameters" were selected to be in line with physiology (Table 1). The simulation was run one thousand times for each bolus-injection scheme.

**Table 1:** Range of values of the perfusion parameters selected in the study for generating simulated liver enhancement curves

	Values	HPI (%)	$v_d$ (%)	$F_t$ (ml/min/100ml)	T (sec)
Liver	Min	15	22.5	150	0
	Max	45	37.5	200	0.001

In order to vary the level of noise for each generated liver enhancement curve, noise was first removed from the experimental AIF, PIF by spline interpolation<sup>20</sup>, and then random noise was added back prior to the generation of the liver enhancement curve.

Finally, a random noise was also added to the generated liver enhancement curve. The amplitudes of these added noises were fixed on the standard deviations (SD) of the baseline of the signal obtained before the first injection. They were measured, in arbitrary units, as follows:  $\sigma_a=600$ ,  $\sigma_p=700$ , and  $\sigma_L=150$  for the AIF, PIF, and liver enhancement curves respectively.

## 2. Estimation of the liver perfusion parameters – deconvolution

The generated liver enhancement curves were then adjusted, employing the same perfusion model used for their generation, with a non-linear optimization fitting technique provided by the Matlab toolbox (Least Mean Square [LMS]). The values of the parameters, that yielded the best fit of the curves, were recorded as the "estimated values" for the perfusion parameters ( $\overline{HPI}$ ,  $\overline{Ft}$ ,  $\overline{vd}$ ).

## 3. Comparison of the initial and estimated parameters

For each perfusion parameter and each condition, the error of the estimation was calculated as the difference between the estimated and the initial values. The robustness of the estimated parameters was assessed by the calculation of the Coefficient of Variation ( $CV\%=(SD/mean)*100$ ), which corresponds to the ratio of the standard deviation (SD) of error of the estimated parameters by the mean value of the original parameters. The CV was evaluated for both injection schemes. For each perfusion parameter, the improvement Factor (IF)<sub>j</sub> between the variability of the first bolus versus the other boluses was calculated as:  $(IF)_j = (CV_1 - CV_j)/CV_1$ , where j=number of boluses.

To test if the amelioration of the parameters' variation didn't arise mechanically from the prolongation of the acquisition duration, rather than from the application of a multi-bolus scheme, we compared the improvement of the multi-bolus scheme on the perfusion parameters with those which were obtained by the single-bolus scheme expanding only the acquisition time. The improvement Factor (IF)<sub>i</sub> between the variability of the length of the acquisition time at 3min versus the other lengths of the acquisition time was calculated as:  $(IF)_i = (CV_{3min} - CV_i)/CV_{3min}$ , where i=length of the acquisition time.

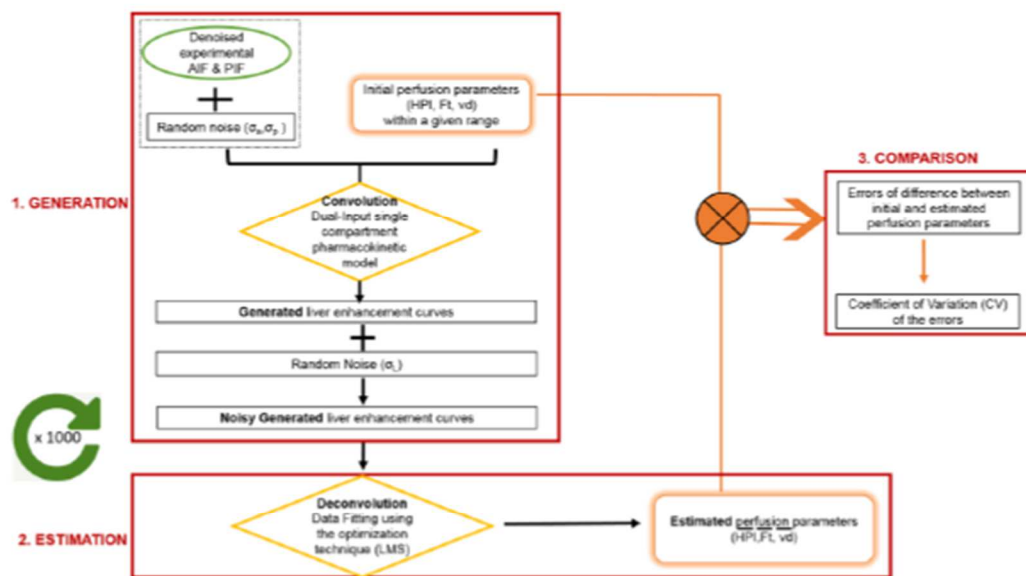


**Figure 4:** Workflow chart of the enhancement curves generation followed by the parameters' extraction: 1. Generation of simulated liver enhancement curves with different perfusion parameters (Generator), 2. Extraction of the estimated perfusion parameters with curve fitting (Estimator), and 3. Comparison between the input and the estimated perfusion values (from the generated liver curves). The simulation ran 1000 times.

### C. Statistical Analysis

F-test was used to evaluate the variability of the CVs of the perfusion parameters in both schemes.  $p < 0.002$  was statistically considered significant by including Bonferroni multi-test correction.

When analyzing the multi-bolus scheme, the variability of the first bolus was evaluated versus the other boluses (two boluses, three boluses, four boluses) to all perfusion parameters. While for the single-bolus scheme, the variability of the 3min-length of the

acquisition time was evaluated versus the other lengths of the acquisition time (5min, 7min, 10min).  $p < 0.002$  was statistically considered significant by including Bonferroni multi-test correction.

## 4. RESULTS

### a. Selection of input functions

Input functions were selected from the same rabbit according to the criteria indicated in the method section. Input enhancement curves (AIF, PIF) for the single- and multi-bolus schemes were consistent (see Fig. 3). The area under the curves of the signals clearly increased for the multi-bolus injection, indicating an expected improvement of SNR. The maximal MR signal in AIF (AIF peak) did not substantially increase after four injections keeping it below the zone of saturation and T2\* effects.

### b. Perfusion Parameters' Variation

When analyzing the multi-bolus injections scheme from two to four boluses, CV decreased compared to the single- bolus injection for all perfusion parameters (Figure 5). The decrease was more pronounced when increasing the number of bolus injections. CV of HPI, Ft, and vd were 31.1%, 12.5%, 5.2% respectively for the single-bolus injection, and 16.2%, 8.1%, 1.8% for the 4-bolus injection (Table 2). The percentage of the CV reduction from 1 to 4-bolus injections were respectively 47.9%, 35.7%, and 65.9% for HPI, Ft, and vd. The improvement was visually more striking for HPI than for Ft and vd, due to its high initial CV, and allowed the CV of HPI to pass below the 20% level.

**Table 2:** Coefficient of Variation (CV) % of the estimated hepatic perfusion parameters obtained following the four-bolus injection protocol. The asterisks (\*) indicate the order of the statistically significant results.  $p \leq 2 \times 10^{-3}$ : \*,  $p \leq 2 \times 10^{-4}$ : \*\*,  $p \leq 2 \times 10^{-5}$ : \*\*\*

Perfusion Parameters	1 bolus (3min)	2 boluses (5min)	3 boluses (7min)	4 boluses (10min)
<b>HPI</b>				
Coefficient of Variation (CV) %	31.12	20.63*	16.32***	16.21***
Improvement Factor %		33.71	47.56	47.91
<b>F<sub>t</sub></b>				
Coefficient of Variation (CV) %	12.52	9.57**	8.95***	8.05***
Improvement Factor %		23.56	28.51	35.7
<b>v<sub>d</sub></b>				
Coefficient of Variation (CV) %	5.22	2.68***	2.21***	1.78***
Improvement Factor %		48.66	57.66	65.9

### Multi- bolus Injection Scheme

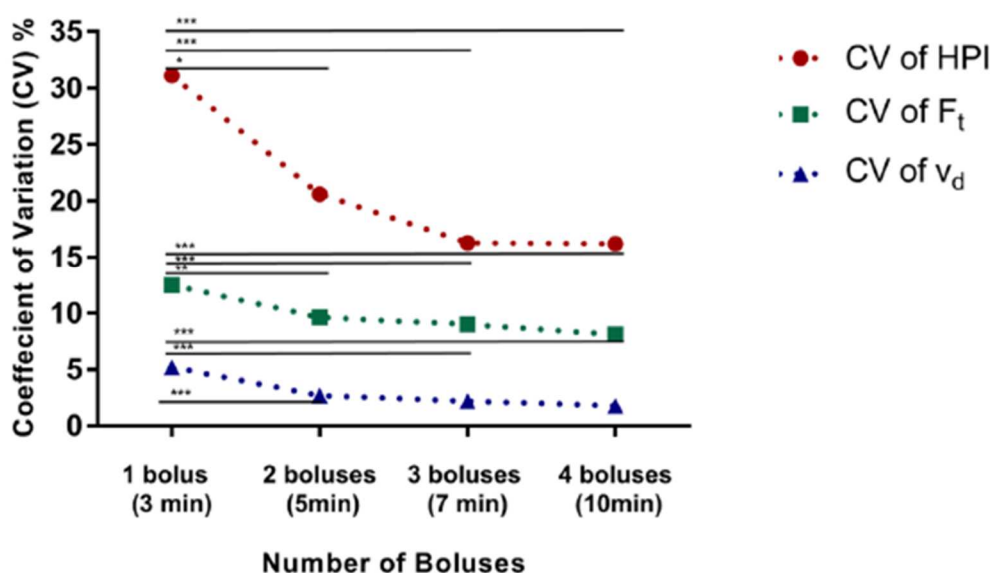


**Figure 5:** Coefficient of variations (CV) obtained with the different number of injection for the extracted hepatic perfusion parameters.  $CV = (SD/mean) \times 100$ . HPI: Hepatic Perfusion Index, F<sub>t</sub>: hepatic blood perfusion v<sub>d</sub>: liver distribution volume fraction. CV improves over all the parameters when using more-boluses. p-values extracted by performing the F-test for 100 repetitions.  $p \leq 2 \times 10^{-3}$ : \*,  $p \leq 2 \times 10^{-4}$ : \*\*,  $p \leq 2 \times 10^{-5}$ : \*\*\*

### c. Acquisition time effect

No significant CV reduction of parameters observed when increasing only the acquisition time from 3 min to 10min for the single-bolus injection scheme (Figure 6, Table 3). Moreover, the CV of HPI tends to increase when applying a longer length of time from the total acquisition, but this increase was not significant.

**Table 3:** Coefficient of Variation (CV) of the estimated hepatic perfusion parameters obtained following the single-bolus injection scheme, when considering different length of time from the total acquisition

Perfusion Parameters	Length of time			
	3min	5min	7min	10min
<b>HPI</b>				
Coefficient of Variation (CV) %	30.29	33.28	33.8	34.33
Improvement Factor %		-9.87	-11.59	-13.34
<b>F<sub>t</sub></b>				
Coefficient of Variation (CV) %	12.37	12.34	12.31	12.13
Improvement Factor %		0.24	0.49	1.94
<b>V<sub>d</sub></b>				
Coefficient of Variation (CV) %	5.15	4.66	4.69	4.95
Improvement Factor %		9.51	8.93	3.88

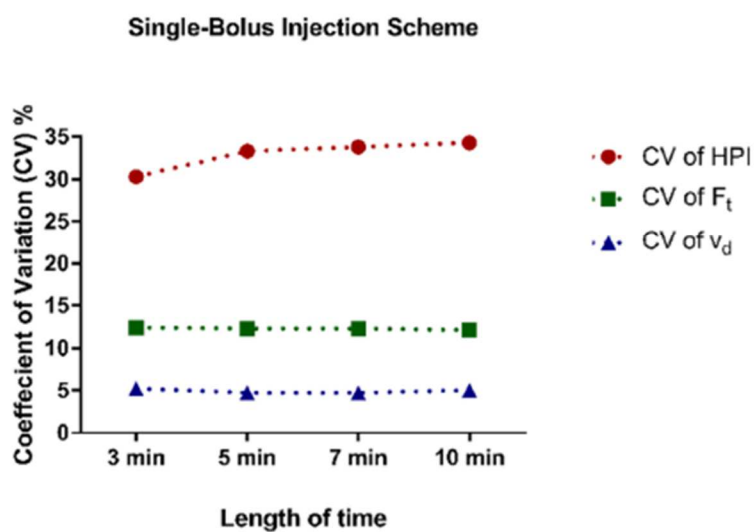


**Figure 6:** Coefficient of variations (CV) obtained with the single-bolus injection scheme when taking into account different length of time from the total acquisition for the extracted hepatic perfusion parameters.  $CV = (SD/mean) \times 100$ . HPI: Hepatic Perfusion Index,  $F_t$ : hepatic blood perfusion  $v_d$ : liver distribution volume fraction. The CV is degraded for the HPI parameter and slightly improved for the  $F_t$  and  $v_d$  parameters using the single-bolus injection with longer acquisition time.

## 5. DISCUSSION

Our aim was to improve the DCE-MRI technique in order to increase the robustness of the liver microcirculation analysis. More specifically, we focused on avoiding high contrast agent concentration to limit the saturation and T2\* effects, while keeping a reasonable total amount of contrast agent to maintain a sufficient sensitivity. To achieve this goal, we injected a limited amount of diluted contrast agent for a bolus but offsetting the resulting loss of signal-to-noise (SNR) by applying multiple boluses. We tested this strategy on the robustness of perfusion parameters of HPI, Ft, and vd, performing a computer simulation with real AIF and PIF. This study shows that the robustness is significantly improved for all liver perfusion parameters (HPI, Ft, vd) when performing the multi-bolus injection scheme in comparison to the single bolus injection scheme, while the signal remained in the area with negligible saturation and T2\* effects. There was a clear improvement for HPI, which is a major parameter for the liver study but has natural poor robustness when using a single-bolus scheme (Fig. 6).

In our study, each unit bolus corresponded to a quarter of the CA clinical dose with a 1/25 dilution. This setting was selected to reach up to 4 injections without exceeding the total clinical dose. In our simulation study for a single bolus, with a ¼ CA clinical dose, vd still evaluated with acceptable precision (CV~5%), Ft with a moderate precision (CV~12%), but HPI was evaluated with poor precision (CV~34%), (Table 3). However, when performing the multi-bolus scheme, the variability of HPI was significantly improved (even from the second bolus) dropping from 31.1% with a single-bolus injection to 16.2% with 4 bolus injections (Figure 5), corresponding approximately to a factor of 2 (Table 2).

HPI is a major perfusion parameter for the normal and the pathological liver <sup>11-15,21-23</sup>. However, in the literature, the mean HPI values measured in normal liver lies in a large range between 5% and 40% <sup>4-8,24,25</sup>. Such a range of values could be explained by poor robustness of HPI derived from 1) moderate SNR, 2) saturation and T2\* effects, and 3) mis-sampling of AIF or PIF, especially when an acquisition with relatively low-temporal resolution was used.

Several strategies have been proposed to overcome these obstacles however, they tend to induce additional drawbacks. Increasing CA dose or CA concentration can improve SNR. However, in the presence of signal saturation, this approach is not

feasible. Alternatively, half a clinical dose of contrast agent is sometimes applied to DCE-MRI protocols to limit the MR signal saturation and T2\* effects. The relevance of that reduced dose depends on acquisition settings, particularly on TR and flip angle. However, the deleterious effects remain very strong at half clinical dose, especially when pure CA is injected. Moreover, SNR is reduced yielding to less robust results. The infusion-technique, which consists of a slow CA injection, can induce high total CA dose without high CA concentration peak. However, it does not allow for signal sharpness and sufficient separation between AIF and PIF, due to the long injection time.

To improve the robustness of the perfusion parameters and to minimize saturation errors induced by large volumes of highly concentrated CA, the application of uneven dual-bolus injection has been suggested in cardiac and lung DCE-MRI <sup>26-31</sup>. This dual-bolus injection technique consists of an injection of a low-dose pre-bolus, followed by the injection of a high-dose main-bolus. The low-dose pre-bolus gives a signal with minimal saturation effects but low SNR, when the high-dose main-bolus gives a high SNR signal but biased by large saturation effects. Information of both injections is then combined to provide a derived dataset with high SNR and, theoretically, corrected for signal bias. However, as with other MRI signal correction techniques, based on reference tubes or pre-T1 mapping, this technique induces complexity and may provide errors either with an inaccurate correction of initial signal or with noise addition induced and multiplied by the correction process. Alternatively, with our approach with low concentration boluses, we remain in the quasi-linear part of the signal enhancement curve - like the low dose pre-bolus - and minimize errors by directly applying the pharmacokinetic model to the data.

To overcome the mis-sampling of AIF and PIF high temporal resolution should be applied to the DCE-MRI sequence. Indeed, low temporal resolution induces errors within the fast-changing region of bolus peak (first-pass peak) as the number of point measurements is not sufficient to describe the real shape of the curve. The first-pass portion of the input function is crucial because it provides important information regarding the arrival and the early fast concentration changes of CA within the vascular space. A precise assessment of the first pass is needed to accurately estimate the tissue blood flow, the tissue blood volume <sup>32</sup>, the temporal shifts between AIF and PIF, and consequently the HPI. Henderson et al <sup>33</sup> have referred in their study that the optimum sampling interval, in order to capture entirely the first-pass peak of AIF,

should be on the order of 1 sec. This temporal resolution cannot be reached, nowadays, with most of the current MRI sequences. The multi-bolus injection strategy increases the total number of measurements during the bolus peak period and consequently increases the statistical power of parametric assessment in a super-resolution type of way. Finally, the strategy of multiple short diluted bolus injections appears to overcome all these limitations.

*Roberts et al*<sup>34</sup>, however, suggested that the division of the dose into several boluses was of no benefit. They tested a double bolus injection protocol over different temporal resolutions simulating the AIF enhancement curves and evaluated the mis-sampling errors on them. The summary of this study was that using a global given CA dose, with a temporal resolution of 2.3 sec, results in equivalence between single- and double-bolus injections. Therefore, they deduced that since the robustness of the parametric estimations was not improved by the double injection approach, this strategy was not advantageous. However, they did not take into account the signal saturation constraint, therefore, the equivalence statement between the single-bolus and the double-bolus injections makes it, in fact, possible to propose that the double-bolus injection, with a diluted CA, could replace the single bolus, without major consequences, and with the advantage of limiting the saturation effects. In addition, it is worth noting that when performing a single-bolus injection exam, the occurrence of an unexpected movement during the first-pass is critical and may lead to the final exclusion of this exam. On the contrary, when performing a multi-bolus injection exam, the negative effect of an unexpected movement during one of the multiple boluses could be greatly minimized, since the "first pass" information is collected during the other boluses.

Some limitations of our study should be noted. The main limitation was that the experimental enhancement curves of the AIF and PIF integrated into the simulation originated from rabbits instead of humans that prevents the straight translation of our results in clinical practice. Additional studies could be performed on the human to confirm our results. It would, however, require two acquisition sets in the subjects to compare both injection strategies. Another limitation is that our results are based on simulations (although using real input functions). However, it is a first step, which provided conclusive results to be followed by in-vivo studies.

To simplify the study, we evaluated our multi-bolus strategy with a simple liver perfusion model (single compartment model without time delay). Even with this simple

model, the results indicated a high variability of HPI for a single-bolus injection. For more complex and more realistic models of liver perfusion, described in the literature, including time-delays for AIF and PIF <sup>7</sup> and a second compartment for the study of tumor <sup>13,22</sup>, substantial augmentation of variability is expected. With these more complex models, the multi-bolus injections strategy may, therefore, be even more useful. This, however, remains to be tested.

Finally, a practical limitation to the multi-bolus injection protocol should be acknowledged. It is more complex to be performed and does not provide the regular "arterial phase" "portal phase" and "late phase" images usually obtained and visually analyzed when using the classical single bolus injection in liver MRI. This limitation, however, may be overcome by the improvement of the quantitative analysis of the liver perfusion.

In conclusion, our study shows that the multi-bolus injection scheme improves the robustness of the liver perfusion parameters' measurement when the limitation of the MRI signal saturation does not allow the injection of CA dose in a single-bolus injection. A major improvement was noticed for the critical HPI parameter, which is particularly affected by poor SNR. Therefore, the improvement of liver DCE-MRI robustness by the multi-bolus injection suggests that it could be prospectively applied to improve tumor diagnosis and treatment monitoring.

## **ACKNOWLEDGMENT**

This work has been financed by BPI France under the HECAM project [Hepatocellular Carcinoma Multi-Technological]

We thank Julie Piquet and the team of the animal house facility at the Carpentier Foundation.

## REFERENCES

1. Pandharipande PV, Krinsky GA, Rusinek H, Lee VS. Perfusion imaging of the liver: current challenges and future goals. *Radiology*. 2005;234(3):661-673. doi:10.1148/radiol.2343031362
2. Ronot M, Lambert S, Daire J-L, et al. Can we justify not doing liver perfusion imaging in 2013? *Diagn Interv Imaging*. 2013;94(12):1323-1336. doi:10.1016/j.diii.2013.06.005
3. Materne R, Smith A m., Peeters F, et al. Assessment of hepatic perfusion parameters with dynamic MRI. *Magn Reson Med*. 2002;47(1):135-142. doi:10.1002/mrm.10045
4. Hagiwara M, Rusinek H, Lee VS, et al. Advanced liver fibrosis: diagnosis with 3D whole-liver perfusion MR imaging--initial experience. *Radiology*. 2008;246(3):926-934. doi:10.1148/radiol.2463070077
5. Van Beers BE, Leconte I, Materne R, Smith AM, Jamart J, Horsmans Y. Hepatic Perfusion Parameters in Chronic Liver Disease. *Am J Roentgenol*. 2001;176(3):667-673. doi:10.2214/ajr.176.3.1760667
6. Baxter S, Wang ZJ, Yeh BM. Timing bolus dynamic contrast-enhanced (DCE) MRI assessment of hepatic perfusion: Initial experience. *J Magn Reson Imaging*. 2009;29(6):1317-1322. doi:10.1002/jmri.21795
7. Chouhan M. Estimation of contrast agent bolus arrival delays for improved reproducibility of liver DCE MRI. - PubMed - NCBI. [https://www.ncbi.nlm.nih.gov/s.frodon-biusante.parisdescartes.fr/pubmed?term=\(estimation%20of%20contrast%20agent%20bolus%20arrival%20delays%20for%20improved%20reproducibility%20of%20liver%20DCE%20MRI%5BTitle%5D\)%20AND%20Chouhan%2C%20Manil%5BAuthor%5D](https://www.ncbi.nlm.nih.gov/s.frodon-biusante.parisdescartes.fr/pubmed?term=(estimation%20of%20contrast%20agent%20bolus%20arrival%20delays%20for%20improved%20reproducibility%20of%20liver%20DCE%20MRI%5BTitle%5D)%20AND%20Chouhan%2C%20Manil%5BAuthor%5D). Published 2016. Accessed July 10, 2017.
8. Materne R, Van Beers BE, Smith AM, et al. Non-invasive quantification of liver perfusion with dynamic computed tomography and a dual-input one-compartmental model. *Clin Sci Lond Engl 1979*. 2000;99(6):517-525.
9. Annet L, Materne R, Danse E, Jamart J, Horsmans Y, Van Beers BE. Hepatic Flow Parameters Measured with MR Imaging and Doppler US: Correlations with Degree of Cirrhosis and Portal Hypertension. *Radiology*. 2003;229(2):409-414. doi:10.1148/radiol.2292021128
10. Ziegler SI, Haberkorn U, Byrne H, et al. Measurement of liver blood flow using oxygen-15 labelled water and dynamic positron emission tomography: limitations of model description. *Eur J Nucl Med*. 1996;23(2):169-177.

11. Fournier L, Cuenod C, de Bazelaire C, et al. *Early Modifications of Hepatic Perfusion Measured by Functional CT in a Rat Model of Hepatocellular Carcinoma Using a Blood Pool Contrast Agent*. Vol 14.; 2004. doi:10.1007/s00330-004-2339-8
12. Abdullah SS, Pialat JB, Wiart M, et al. Characterization of hepatocellular carcinoma and colorectal liver metastasis by means of perfusion MRI. *J Magn Reson Imaging*. 28(2):390-395. doi:10.1002/jmri.21429
13. Jian-Feng Yang. Dual-input two-compartment pharmacokinetic model of dynamic contrast-enhanced magnetic resonance imaging in hepatocellular carcinoma. - PubMed - NCBI. [https://www.ncbi.nlm.nih.gov/s.frodon-biusante.parisdescartes.fr/pubmed/?term=\(dual+input+two+compartments+pharmacokinetic+model+of+dynamic+contrast+enhanced+magnetic+resonance+imaging+in+hepatocellular+carcinoma\)+AND+Yang%5BAuthor%5D](https://www.ncbi.nlm.nih.gov/s.frodon-biusante.parisdescartes.fr/pubmed/?term=(dual+input+two+compartments+pharmacokinetic+model+of+dynamic+contrast+enhanced+magnetic+resonance+imaging+in+hepatocellular+carcinoma)+AND+Yang%5BAuthor%5D). Published 2016. Accessed July 4, 2017.
14. Cuenod C, Leconte I, Siauve N, et al. Early changes in liver perfusion caused by occult metastases in rats: detection with quantitative CT. *Radiology*. 2001;218(2):556-561. doi:10.1148/radiology.218.2.r01fe10556
15. San Koh T, Thng CH, Hartono S, et al. Dynamic contrast-enhanced CT imaging of hepatocellular carcinoma in cirrhosis: feasibility of a prolonged dual-phase imaging protocol with tracer kinetics modeling. *Eur Radiol*. 2009;19(5):1184.
16. Rohrer M, Bauer H, Mintorovitch J, Requardt M, Weinmann H-J. Comparison of magnetic properties of MRI contrast media solutions at different magnetic field strengths. *Invest Radiol*. 2005;40(11):715-724.
17. Lecler A, Balvay D, Cuenod C-A, et al. Quality-based pharmacokinetic model selection on DCE-MRI for characterizing orbital lesions. *J Magn Reson Imaging JMRI*. April 2019. doi:10.1002/jmri.26747
18. Thomassin-Naggara I, Soualhi N, Balvay D, Darai E, Cuenod C-A. Quantifying tumor vascular heterogeneity with DCE-MRI in complex adnexal masses: A preliminary study. *J Magn Reson Imaging*. 2017;46(6):1776-1785. doi:10.1002/jmri.25707
19. Balvay D, Frouin F, Calmon G, et al. New criteria for assessing fit quality in dynamic contrast-enhanced T1-weighted MRI for perfusion and permeability imaging. *Magn Reson Med*. 2005;54(4):868-877. doi:10.1002/mrm.20650
20. Schmid VJ, Whitcher B, Padhani AR, Yang G. Quantitative Analysis of Dynamic Contrast-Enhanced MR Images Based on Bayesian P-Splines. *IEEE Trans Med Imaging*. 2009;28(6):789-798. doi:10.1109/TMI.2008.2007326
21. Ghodasara S, Pahwa S, Dastmalchian S, Gulani V, Chen Y. Free-Breathing 3D Liver Perfusion Quantification Using a Dual-Input Two-Compartment Model. *Sci Rep*. 2017;7(1):17502. doi:10.1038/s41598-017-17753-9

22. Koh TS, Thng CH, Lee PS, et al. Hepatic metastases: in vivo assessment of perfusion parameters at dynamic contrast-enhanced MR imaging with dual-input two-compartment tracer kinetics model. *Radiology*. 2008;249(1):307-320. doi:10.1148/radiol.2483071958
23. Jajamovich GH, Huang W, Besa C, et al. DCE-MRI of hepatocellular carcinoma: perfusion quantification with Tofts model versus shutter-speed model—initial experience. *Magn Reson Mater Phys Biol Med*. 2016;29(1):49-58. doi:10.1007/s10334-015-0513-4
24. Kanda T, Yoshikawa T, Ohno Y, et al. Hepatic computed tomography perfusion: comparison of maximum slope and dual-input single-compartment methods. *Jpn J Radiol*. 2010;28(10):714-719. doi:10.1007/s11604-010-0497-y
25. Miyazaki M, Tsushima Y, Miyazaki A, Paudyal B, Amanuma M, Endo K. Quantification of hepatic arterial and portal perfusion with dynamic computed tomography: comparison of maximum-slope and dual-input one-compartment model methods. *Jpn J Radiol*. 2009;27(3):143-150. doi:10.1007/s11604-008-0312-1
26. Christian TF, Rettmann DW, Aletras AH, et al. Absolute myocardial perfusion in canines measured by using dual-bolus first-pass MR imaging. *Radiology*. 2004;232(3):677-684. doi:10.1148/radiol.2323030573
27. Köstler H, Ritter C, Lipp M, Beer M, Hahn D, Sandstede J. Prebolus quantitative MR heart perfusion imaging. *Magn Reson Med*. 2004;52(2):296-299. doi:10.1002/mrm.20160
28. Groothuis JGJ, Kremers FPPJ, Beek AM, et al. Comparison of dual to single contrast bolus magnetic resonance myocardial perfusion imaging for detection of significant coronary artery disease. *J Magn Reson Imaging JMRI*. 2010;32(1):88-93. doi:10.1002/jmri.22231
29. Utz W, Greiser A, Niendorf T, Dietz R, Schulz-Menger J. Single- or dual-bolus approach for the assessment of myocardial perfusion reserve in quantitative MR perfusion imaging. *Magn Reson Med*. 2008;59(6):1373-1377. doi:10.1002/mrm.21611
30. Veldhoen S, Oechsner M, Fischer A, et al. Dynamic Contrast-Enhanced Magnetic Resonance Imaging for Quantitative Lung Perfusion Imaging Using the Dual-Bolus Approach: Comparison of 3 Contrast Agents and Recommendation of Feasible Doses. *Invest Radiol*. 2016;51(3):186-193. doi:10.1097/RLI.0000000000000224
31. Risse F, Semmler W, Kauczor H-U, Fink C. Dual-bolus approach to quantitative measurement of pulmonary perfusion by contrast-enhanced MRI. *J Magn Reson Imaging*. 2006;24(6):1284-1290. doi:10.1002/jmri.20747
32. Cuenod CA, Balvay D. Perfusion and vascular permeability: Basic concepts and measurement in DCE-CT and DCE-MRI. *Diagn Interv Imaging*. 2013;94(12):1187-1204. doi:10.1016/j.diii.2013.10.010

33. Henderson E, Rutt BK, Lee TY. Temporal sampling requirements for the tracer kinetics modeling of breast disease. *Magn Reson Imaging*. 1998;16(9):1057-1073.
34. Roberts C, Buckley DL, Parker GJM. Comparison of errors associated with single- and multi-bolus injection protocols in low-temporal-resolution dynamic contrast-enhanced tracer kinetic analysis. *Magn Reson Med*. 2006;56(3):611-619. doi:10.1002/mrm.20971

